Bistatic Scattering of Acoustic Waves from a Rough Ocean Bottom

by

Yevgeniy Yakov Dorfman

M.S., Electrical Engineering
Gorky University, 1989

Submitted to the Department of Ocean Engineering
in partial fulfillment of the requirements for the degree of

Doctor of Philosophy

at the

MASSACHUSETTS INSTITUTE OF TECHNOLOGY

September 1997

Author .....
Department of Ocean Engineering
June 5, 1997

Certified by....
Professor Ira Dyer
Weber-Shaughness Professor of Ocean Engineering
Thesis Supervisor

Accepted by..........
Professor J. Kim Vandiver
Chairman, Department Committee on Graduate Students

Bistatic Scattering of Acoustic Waves from a Rough Ocean Bottom

by

Yevgeniy Yakov Dorfman

Submitted to the Department of Ocean Engineering
on June 5, 1997, in partial fulfillment of the
requirements for the degree of
Doctor of Philosophy

Abstract

Proper understanding and modeling of the bistatic scattering of sound from the ocean bottom is vital for underwater acoustics. The problem of pulse scattering from rough surfaces, Rayleigh parameter $\gamma > 1$, in the midfrequency range 200-250 Hz ($\lambda = 6m$), is considered. An analytical model for scattering strength is developed and found to match with the ARSRP-93 experimental data. Mean value and higher order statistical properties of the signals received during the experiment are analyzed independently.

Analysis of the higher order statistical properties shows that they are controlled by the bistatic angle only. Further analysis suggests that the major contribution to the scattering strength is generated by the $O(\lambda)$ scales on the bottom, thus supporting a separation of scales hypothesis.

The mean value of the received signal (scattering strength) is controlled by the large scale geomorphology and the experimental geometry. It is found that Lambert's Law, which assumes infinitely small wavelength, does not explain experimental data. Small perturbation theory accounts for the wave effects involved in the problem and hence performs better. However, it underpredicts the levels of scattering in back directions by about 10 dB. The separation of scales hypothesis suggests that small features, not accounted for by the first order small perturbation solution, are responsible for enhanced scattering into back directions. A heuristic model based on combination of small perturbation and boss theory is developed, within the separation of scales framework to account for those features which, except in forward scattering, matches experimental data to within 3 dB.

Thesis Supervisor: Professor Ira Dyer
Title: Weber-Shaughness Professor of Ocean Engineering

Acknowledgments

First of all, I would like to thank my advisor, Prof. Ira Dyer. I admire your physical intuition and technical expertise. Your ability to identify limitations was a constant source of encouragement, thank you for it. Looking back, every meeting with you was fun, working for you was a privilege most greatfully acknowledged, an experience never to be forgotten.

I am also grateful to the entire acoustics group. Henrik Schmidt: I benefited much more than I dreamed to from our discussions, your help is greatly appreciated. Thanks to the rest of my thesis committee, Arthur Baggeroer and Rob Fricke, for working with me on my thesis. Thanks to Dr. Guo for working on special projects with me.

A special thank to Dr. Joseph Bondaryk. You are a great teacher, Joe. I will always remember your eagerness to help (which is NOT your job, hence even more appreciated).

Dear Dr. Tucholke: you help in geology is greatly appreciated. Your vision of the ocean bottom helped me to shape my understanding.

Support for this thesis was provided by the Office of Naval Research, it is greatfully acknowledged.

Thanks to the acoustics group administrative staff. Sabina Rataj, I can feel your absence even for one day. Thank you for caring.

Thanks to all my office mates. Yury, it feels great to speak Russian once in a while, and thanks for your support. Peter, my thesis still would have been sitting in the printer queue without your help. Pierre, your thoughtful comments are just great! Jo-Tiam (JT) Goh, and Ken Rolt, you were first at MIT to come to rescue my language (well, never mind what Joe thinks of it, I still call it "English"). Jaiyong Lee, Brian Sperry, Brian Tracey, Hua He, Dan Li and the rest of 5-007 and 5-435 crew, thank you for your company.

Last but not list I want to thank my wife. Lena, we haven't seen each other much lately, things will change, I promise!

Contents

List of Tables

List of Figures

Chapter 1

Introduction

1.1 Motivation

The problem of scattering of acoustic waves from rough surfaces is still extensively investigated. The reason for the continued attention it fairly simple. Conventionally all issues in underwater acoustics are categorized either as a direct or an inverse problem. Properties of sound scattering from rough ocean surfaces and bottoms are vital for both direct and inverse problems, i.e., in all underwater sound applications.

A direct problem usually arises in sonar engineering. The major question asked is to find the sound field incident on the receiver due to given sources in a certain environment. The practical implication of this question is clear.

Imagine for instance an arbitrary sonar system. Its performance is sought about in terms of its detection ability. Detection ability in turn is governed by the signal-to-noise ratio. It is customary to distinguish different sources of noise in the ocean. First, there is ambient noise. Second, there is system noise, i.e., noise created within the sonar system itself. At last, the ocean environment contains inhomogeneities within the water column and on its rough boundaries. The combined effect of sound scattering back from all these inhomogeneities is conventionally called reverberation. Consequently, the equivalent noise is called the reverberation noise.

As long as power radiated by the sonar is small enough, reverberation will be indistinguishable in the received signal due to the first two noise sources. This system is so-called noise-limited, i.e., noise contributing to the signal-to-noise ratio is a sum of the system noise and the ambient noise in the ocean. Neither one of those two noise sources is a function of the radiated signal itself, so sonar performance can be enhanced by increasing the power of its transmitter, thus increasing sound scattered from the target, i.e., the received signal, while leaving noise unchanged. On the contrary, power scattered from inhomogeneities will increase at the same rate as power scattered from the targets we are trying to detect, eventually outrgrowing ambient and system noise and becoming the most important of all three noise sources. Thus powerful and capable sonar systems can become reverberation-limited. Now, to achieve better performance it is necessary to somehow control reverberation. And to make an assessment of sonar performance, a good model of the reverberation must be developed.

This emphasizes the practical importance of studying the reverberation. Also, the intrinsic property of reverberation noise as a sonar dependent property is highlighted. In contrast ambient noise is independent of the sonar, i.e., independent of the way we observe it, while reverberation noise is a function of both environment and the sonar system. Unlike any other type of noise, reverberation can not be sought independently, without considering how we observe it. Reverberation does not manifest its existence without external intervention. We encounter it while operating a sonar, or otherwise interacting with inhomogeneities. As in quantum mechanics, the way we observe the phenomena may alter what we see.

The inverse problem is also frequently encountered in applications, especially in oceanography. In this scenario, properties of the environment are deduced from the amount of reverberation noise generated due to the operation of a certain sound source. Usually a sound source is controlled by the experimenter, however generally this does not have to be the case. Scattering of sound generated by sources already present in the ocean can also indicate the configuration of the environment.

In solving the direct problem, reverberation is usually considered as noise we would like to get rid of. Conversely, while solving the inverse problem reverberation is treated as a signal carrying information about environment. The same techniques and models are commonly used for the direct and inverse problem solution, hence the difference between these two problems is often confined to the attitude of the researcher. Qualitative and quantitative understanding of the process of acoustic reverberation in the ocean, inherently interconnected with the ability to properly model the phenomenon, is vital for the solution of both the direct and inverse problems.

1.2 Objectives

To improve knowledge about rough ocean bottom scattering, a large scale experiment was initiated by ONR. The first stage of the experiment was conducted in 1991 employing two ships. Three ships were used in the second stage in 1993. These stages are conventionally known as ARSRP-91 and ARSRP-93, respectively. The later one is described in detail in subsequent sections. A large volume of scattering data was acquired during the experiment and made available for researchers. Cited from [1], important scientific questions of the experiment were:

- What are the important mechanisms of rough, elastic, heterogeneous seafloor scattering? What seafloor features cause scattering that appears event-like when high resolution signals are used? Is this scattering associated with high slope surfaces such as faults on the seafloor or features beneath a thin sediment cover? What role does propagation have to play (caustics etc.) in the generation of highly-resolved signals?
- How important is elasticity of the seafloor for scattering? Are Neumann, Dirichlet or impedance boundary conditions useful concepts? Are compressional and shear speed profiles necessary for accurate prediction? Might scattering be affected by volumetric inhomogeneities in the basement?
- Is large scale seafloor geomorphology the dominant variable in controlling scattering? What description of seafloor geomorphology at near

wavelength scales is needed to predict scattering? Is a fractal self-similar model adequate for this small scale? What is the sensitivity of measured and model results to interface characteristics like fractal/non-fractal of, if applicable, Gaussian/non-Gaussian statistics and within divisions, what is the sensitivity to variation of parameters like the five in the Goff-Jordan model?

- What is a good characterization of seafloor scattering? Can the properties of the reverberation be described using stochastic concepts, or is a more deterministic approach necessary? If a stochastic approach can be used, is the concept of scattering strength as used in the sonar equation useful for quantifying scattering with a high resolution system? Do simple models like Lambert's Law have a useful role in describing the scattering?

In the following I will analyze and model the midfrequency data ($\lambda = 6m$), in order to address some of these questions.

1.3 Major results

Analyzing the data I found that the received scattering signal is a highly nonstationary function of time. I show that two goals are achieved by removing local short-time average from the received signal. First, this procedure allows one to separate the signal into its "slow" and "fast" components, where the slow component (local mean) carries information about the first order statistical properties of the signal, and higher order statistical properties are encapsulated in the fast component (signal with its local mean removed). Second, the resulting fast component is a stationary stochastic process, which simplifies its statistical analysis. Subsequently, I show that different physical parameters control first and higher order statistical properties of the received signal, hence slow and fast components can be analyzed and modeled independently.

Considering the higher order statistical properties of the received signal, I find that discreteness of the scattering process results in a slight deviation of the received signal probability density distribution away from the Gaussian at high levels of the received signal. However, a substantial difference between signal and Gaussian noise is found considering temporal distribution of individual features in the received signal (peaks). Therefore, I conclude that analysis of individual peaks in the received data is a better indicator of statistical properties of the received signal, and hence a better reflection of the physics of scattering. Additionally, I find that the major contribution to scattering is generated by the $O(\lambda)$ scales on the bottom, which supports a separation of scales hypothesis [2, 3], and emphasizes the importance of wave effects. Later I show that the first order statistical properties of the received signal (related to the scattering strength) are controlled by the experimental geometry and large scale geomorphology, with essential roughness scales on the order of the sonar footprint size $L_0 \approx 100 \div 1000\, m$.

Then it becomes clear that the scattering observed during the ARSRP-93 experiment is a multiscale process, and therefore a multiscale wave scattering theory is required for its proper understanding and modeling. This explains the apparent mismatch between the experimental data and the geometric Lambert's Law [4] which assumes infinitely small incident wavelength. Small perturbation theory [5, 6] accounts for the finiteness of the incident wavelength and captures the correct functional dependence of the scattering signal, however underpredicts its level by about 10 dB in the back directions.

Using the separation of scale hypothesis I suggest that small features not accounted for by the first order small perturbation (SP) solution are responsible for the enhanced scattering in the back directions. To improve the model, I propose a composite boss - SP theory. Within this model, the solution is sought of as an incoherent superposition of contributions from small scales, accounted via the boss theory, and the SP solution. Conceptually this model is in line with the standard 2-scale theory [7], where the solution for a relatively large scattering patch is sought as a combination of SP and Kirchhoff solutions. Finally, I show that the model developed results in an improved fit with the experimental data (to within 3 dB).

1.4 Notation

I use complex representation of the acoustic field parameters throughout, harmonic time dependence is implied unless otherwise stated. Consequently the physical value of a parameter is given by the real part of its complex representation. So, for instance, if ξ stands for the complex amplitude of the parameter ξ, the value of the parameter observed in an experiment is

$$\xi_{physical} = Re\xi = \frac{1}{2}(\xi + \xi^*), \tag{1.1}$$

where superscript star as usual means complex conjugate.

Overbar is chosen to designate time average of a random function. Often a square value of the complex amplitude of a harmonic function averaged over its period is of interest. In complex notation it becomes

$$\overline{\xi^2} = \xi \cdot \xi^*, \tag{1.2}$$

hence, for a physical (observable) value

$$\overline{\xi^2_{physical}} = \frac{1}{2}(\xi \cdot \xi^*) = \frac{1}{2}\overline{\xi^2}. \tag{1.3}$$

As a shortcut for the mean square value of a complex amplitude, the overbar is omitted, so for a harmonic function ξ^2 stands for $\overline{\xi^2}$ unless otherwise stated.

Angle brackets $\langle\rangle$ are chosen to indicate an ensemble average of a random function. An average over the period and the ensemble mean square value of the complex amplitude can be expressed as $\left\langle\overline{\xi^2}\right\rangle$ or equivalently in the shortcut notation as $\langle\xi^2\rangle$.

1.5 Thesis organization

First, in Chapter 2 I present a brief outline of the problem. I start the discussion with a review of the basics of sound propagation in the ocean. This naturally leads to the recapitulation of classical scattering terminology. It then becomes clear that an adequate model of rough surface scattering is a cornerstone in understanding reverberation phenomena and, consequently, reverberation noise. In Chapter 3 rough surfaces are described in terms useful for the subsequent development of the scattering theory used in this thesis. Chapter 4 briefly presents several classical rough surface scattering theories. In Chapter 5 the ARSRP experiment is described. This experiment was designed to refine our knowledge of low grazing angle reverberation. Analysis of higher order statistics in the time series acquired during the ARSRP experiment is presented in the Chapter 6. Subsequently in Chapter 7 I analyze the bistatic scattering strength observed during the ARSRP experiment. Finally, in the Chapter 8 I present a summary of the thesis and suggestions for future work.

Chapter 2

Problem Outline

A standard sonar experiment is designed as follows. A signal consisting of a sound pulse is radiated from a source. The signal propagates to the receiver in the inhomogeneous ocean environment. Knowing the source and the environmental parameters, one would like to compute the signal registered by the receiver. Several issues should be confronted in order to resolve the matter.

- First, a mixture of the signal with ambient noise is inevitably recorded. Hence, proper understanding and adequate modeling of the noise in the ocean is essential to detecting and studying scattering and reverberation.

- Second, a way must be found to determine the paths followed by the sound signals, and to decide how sound parameters might have been changing along these paths. This means that a model of sound propagation in the environment has to be established.

- Third, inhomogeneities are present in the path of the sound waves, hence there will be an interaction between sound and inhomogeneities, or in other words scattering of the incident sound wave from inhomogeneities. The properties of the sound wave can be dramatically altered during this interaction, hence the importance of studying scattering.

Traditionally three classes of scattering are distinguished. The first class consists of scattering from individual inhomogeneities that can be distinguished in the received signal. In turn, such an inhomogeneity is referred to as a "target" or "scatterer". Often the observer attitude alone dictates the choice between target and scatterer, so that any unwanted target might be called a scatterer.

The second class may be described as follows. When scattering from many inhomogeneities, somehow distributed in the entire volume of the water, contribute to the received signal, the interaction of the acoustic field with these inhomogeneities is usually designated as volumetric scattering. Usually these inhomogeneities are considered small and abundant, so that individual scatterers are not seen, and the received signal is some sort of aggregation of individual contributions.

The third class is scattering from a surface. This type of scattering is encountered when the inhomogeneities are two-dimensional, or are a distribution of three-dimensional inhomogeneities on the interface. Usually within this class of scattering problems, scattering from rough surfaces is distinct from scattering from smooth surfaces, thus forming a lower level of categorization.

Sometimes, the combined effect of scattering from all inhomogeneities presented in the environment is called reverberation [8]. However, often reverberation has a more restrictive meaning, so that only scattering from the ocean surface, bottom and volume into one direction only (back to the source of the signal) is termed reverberation [9]. Sometimes the subdivision between different kinds of scattering, and between scattering and reverberation, appears artificial. For instance, reverberation clearly is not an independent phenomenon and can be understood through its components: propagation and scattering. However, the delineated classification often proves effective in distinguishing between different natural phenomena, and so will be followed.

To develop a proper understanding of the sonar experiment, all three problems outlined must be resolved. In this thesis I will mostly concentrate on scattering issues. However, results of the sonar experiment (ARSRP) will be used to enhance our knowledge about the rough bottom scattering. Hence, to build a basis for the interpretation of experimental results, I start here with a brief outline of how the first two problems (noise and propagation) can be approached, followed by the essential scattering terminology.

2.1 Ambient noise in the ocean

More complete discussion of ambient noise can be found in [4, 10, 11, 12]. A brief outline of the terminology follows.

Ambient noise is "the sound of the ocean" [10], i.e., that part of the acoustic field that exists in the ocean without any intervention from the researcher. Ambient noise constantly varies with time and location. Knowing its exact level at each moment is hardly possible, so stochastic models of noise in the ocean environment are pursued.

Mean square noise pressure p_n^2 detected by an omnidirectional receiver is a common measure of ambient noise energy. To indicate frequency dependence and directivity of the noise power, the spectral power density of noise $\tilde{W}_n(\omega, \vec{k})$ is introduced, where a Fourier transform is performed over both temporal and spatial variables, $\vec{k}$ is the wave vector associated with the noise and ω is the noise frequency. This quantity normally is used as a measure of the noise field. Mean square pressure p_n^2 is simply related to the power spectral density:

$$p_n^2 = \int_{-\infty}^{\infty} d\omega \int_{-\infty}^{\infty} \tilde{W}_n(\omega, \vec{k}) d\vec{k}. \tag{2.1}$$

The input power of the unwanted interference measured by the system with transfer function $TF(\omega\vec{k})$ is proportional to the actual mean square pressure of noise $p_{n,act}^2$:

$$p_{n,act}^2 = \int_{-\infty}^{\infty} d\omega \int_{-\infty}^{\infty} \tilde{W}_n(\omega, \vec{k}) TF^2(\omega, \vec{k}) d\vec{k}. \tag{2.2}$$

This number can serve as an indicator of the actual noise limiting the sonar performance. However, in practice usually its base ten logarithm, called noise level, is used instead:

$$L_n = 10 \log(p_{n,act}^2). \tag{2.3}$$

2.2 Sound propagation in the inhomogeneous environment

The science of sound propagation modeling is still growing nowadays. Several wave theories have been recently developed in addition to existing ones [13, 14, 15, 16, 17, 18, 19, 20].

The reason for continuous attention to this topic is that the ocean is an extremely complicated environment, where all parameters are constantly changing with depth, range and time. Due to the presence of boundaries (ocean surface and bottom, targets) several different paths connecting source and receiver are generally possible. This multipathing adds complexity to an already complicated problem.

Ray theory (which I will limit myself to) was the first to appear, as an extension of classical geometrical optics. Although a tremendous amount has been accomplished in pursuit of wave theories of sound propagation, rays are still a powerful tool for understanding and modeling [21, 10, 22, 23, 24].

Rays carry an intuitive meaning, and often can provide useful physical insights into the nature of sound propagation. Ray solutions require the least mathematical investment, and frequently can be performed analytically. And surprisingly enough, a properly executed ray solution often has the same level of quantitative precision as more involved wave theories do. I use rays in the analysis of the ARSRP experiment, hence a summary of the theory is briefly outlined here.

A ray is an imaginary line drawn in the direction locally normal to the wavefront. The computation of this line is referred to as ray tracing. Rays outline the direction of the field propagation, i.e., they are a geometrical property of the field. Additional considerations allow one to determine how energy associated with the field changes along the ray. To derive ray equations one often starts with a linear sound wave equation [22, 9]:

$$\nabla^2\Phi = \frac{1}{c^2(\vec{r})} \cdot \frac{\partial^2\Phi}{\partial t^2}, \tag{2.4}$$

where $\vec{r}$ is the coordinate vector in the three dimensional space, $c(\vec{r})$ is the sound speed in the ocean, t is time, and Φ is the scalar acoustic potential. All physical parameters of sound can be expressed in terms of the potential. For instance, particle displacement $\vec{d}$, velocity $\vec{v}$, sound pressure p and energy flux $\vec{F}$ take the following form:

$$\vec{d} = \nabla\Phi, \quad \vec{v} = \frac{\partial}{\partial t} \nabla \Phi, \quad p = -\rho\frac{\partial^2\Phi}{\partial t^2}, \quad \vec{F} = \rho\frac{\partial^2\Phi}{\partial t^2} \nabla \frac{\partial\Phi}{\partial t}, \tag{2.5}$$

where ρ is the density. Then solution to the wave equation is sought in the form of a harmonic wave: $\Phi = \Phi_0(\vec{r}) \cdot e^{-i\omega(t-\tau(\vec{r}))}$, where τ is called the eikonal. Ray approximations are valid when both $\Phi_0(\vec{r})$ and $\nabla\tau(\vec{r})$ are slow functions of $\vec{r}$, so that the following is correct:

$$\left|\frac{\nabla^2\Phi_0}{\Phi_0}\right| << \frac{\omega^2}{c^2}, \quad \left|\frac{\nabla\tau \cdot \nabla\Phi_0}{\Phi_0}\right| << \frac{\omega^2}{c^2}, \quad \left|\nabla^2\tau\right| << \frac{\omega^2}{c^2}. \tag{2.6}$$

Then the wave equation is reduced to the well known eikonal equation:

$$\left|\nabla^2\tau\right|^2 = \frac{1}{c^2}. \tag{2.7}$$

Approximating the solution as a locally plane wave, one ends up with

$$\nabla\tau = \frac{1}{c}\vec{n}, \tag{2.8}$$

where $\vec{n}$ is the local normal to the wave front. Ray tracing equations subsequently obtained for the case of in-plane propagation in the (xz) plane take the form:

$$\begin{cases} \frac{d}{dt}\left(\frac{1}{c}\cos\theta\right) = -\frac{1}{c}\frac{\partial c}{\partial x}, \\ \frac{d}{dt}\left(\frac{1}{c}\sin\theta\right) = -\frac{1}{c}\frac{\partial c}{\partial z}, \end{cases} \tag{2.9}$$

where θ is the grazing angle measured from horizontal.

Finally, for the range independent environment (2.9) can be further reduced to the differential Snell's law:

$$\frac{\cos\theta}{c(z)} = \sigma = const, \tag{2.10}$$

where the horizontal slowness σ acts as the ray label.

The ray solution gives only the direction of energy propagation. However it exposes an important property of rays. Substituting the solution in the form of the plane wave into (2.5) one can see that $\vec{F} = \rho\omega^3\Phi^2 k\vec{n}$, hence energy flow is parallel to the ray direction.

Consider now a tube of rays. Conservation of energy requires that energy flow through any tube cross section is constant. Then the equation for the sound energy change along the ray is:

$$p_2^2 = p_1^2 \cdot \frac{\rho_1 c_2 A_1}{\rho_2 c_1 A_2}, \tag{2.11}$$

where $p_{1,2}^2$ are mean square pressure amplitudes, $\rho_{1,2}$ are densities and $c_{1,2}$ are sound speeds observed in cross sections 1 and 2 with areas $A_{1,2}$, respectively.

Generally, equations (2.10) and (2.11) are solved numerically for any given sound speed profile $c(z)$. However, for several profiles there are analytical solutions. For instance, if the sound speed is a linear function of depth, i.e., $c(z) = c(z_0) + g(z - z_0)$, then the ray path is a circle with radius of curvature given by

$$r_c = -1/\sigma g. \tag{2.12}$$

Usually the sound speed profile is known through direct or indirect measurement at several depths. Then these measurements can be approximated with a piecewise linear curve. Each piece with a constant gradient g of the sound speed define a layer. In each layer ray calculations can be carried out analytically resulting in the following expressions for sound propagation forward from a point source [10]:

$$\begin{cases} R_{12} = \frac{1}{\sigma g}(\sin\theta_1 - \sin\theta_2), \\ Z_{12} = \frac{1}{\sigma g}(\cos\theta_2 - \cos\theta_1), \\ t_{12} = \frac{1}{2g}\ln\frac{(1+\sin\theta_1)(1-\sin\theta_2)}{(1-\sin\theta_1)(1+\sin\theta_2)}, \\ p_2^2 = \frac{\rho_2 c_1 W}{4\pi R_{12}}\frac{1}{\tan\theta_2}\frac{d\theta_1}{dR_{12}}, \end{cases} \tag{2.13}$$

where R_{12} and Z_{12} are horizontal and vertical distances traveled by the ray, θ_1 and θ_2 are grazing angles at the entrance and exit from the layer, respectively, determined via Snell's law, t_{12} is the travel time, and W is the power radiated by the source. Using the forms of (2.13) in each layer results in an efficient numerical solution for the sound pressure.

The first three equations in the (2.13) are an outcome of the ray tracing equations (2.9), hence valid when (2.6) is true. For a plane wave propagating in the layered medium with sound speed $c(z)$ having gradient $g(z)$ dependent on the vertical coordinate z only it is equivalent to [9]:

$$\frac{1}{k_z}\left|\frac{d}{dz}\log k_z\right| << 1. \tag{2.14}$$

For steep rays with $k_z = O(k)$ it can be further reduced to $g\lambda/c << 1$

[9], which sometimes is said to be the ray theory applicability condition. But in the vicinity of a turning point $k_z \rightarrow 0$ and condition (2.14) become inapplicable for an arbitrary small g. However, it was shown to primarily affect the phase accumulated along the ray path and the field amplitude calculation, and to have less profound effect on the ray direction calculation [9, 25]. The last equation in the (2.13) is a result of the energy conservation consideration along the ray tube. Near the caustic the ray tube diameter shrinks to zero. It results in an infinite value of the field amplitude, from use of the last equation of (2.13). More precise WKB approximations [9, 25] or more involved methods of the ray tube calculation [22] can in fact overcome this difficulty. Then caustics can be safely included into the ray theory applicability domain. Matched asymptotic expansion can be used to treat turning points correctly [25]. However, all this results in somewhat different and more complicated ray tracing equations. Using simplified forms (2.13) specifically restricts one to the regions away from caustics and turning points.

2.3 Basic scattering terminology

A ray can be an adequate tool for sound propagation modeling when inhomogeneities are smooth, i.e., when medium parameters are changing only slightly on the scale of the wavelength. Hence ray theory can not be used near rough boundaries. Examination of wave propagation theories indicate the same tendency: the presence of a boundary in the domain of the solution can not be handled. Approximations made to enhance performance of the theory in application to propagation preclude its use in the vicinity of boundaries. A specific tool is required to properly address the issue, i.e., a scattering theory. Then propagation theory can be used to trace the sound to and from the interface, and scattering theory then describes the interaction with the boundary.

Boundaries in the ocean are represented by the bottom and surface, by coast lines, and also by wanted and unwanted targets that may exist within the water column. In the next subsections essential terminology is briefly summarized.

Considering scattering it is advantageous to make use of the following two assumptions. First, it is known that sound waves decay exponentially as they propagate due to absorption. By no means can we neglect absorption in propagation. However only rarely does absorption affect scattering, hence it will be ignored from now on. The other limitation reasonable to presuppose is local homogeneity and isotropy of the medium in the vicinity of the target or scatterer. These two restrictions allow one to effectively isolate scattering effects from those imposed by propagation.

2.3.1 Scattering from targets: target strength

Consider a plane sound wave with pressure amplitude p_i, wave vector $\vec{k_i}$ and wavelength $\lambda_i = 2\pi/k_i$ incident upon a body. In scattering this body is often referred to as a target. Incident acoustic pressure causes vibrations on the surface of the target and within its volume, and a new system of waves originates from these vibrations. This part of the acoustic field is called the scattered field or equivalently the scattered wave.

Generally the scattered pressure field in the vicinity of the target is quite complicated. However, at large distances from the target with characteristic size D defined by $r >> D^2/\lambda_i$, the scattered field can be represented as a locally plane spherically spreading wave traveling out from the target to the observer. Thus, a target at large distances behaves as an effective directive source of the scattered wave. This is the so-called far field approximation.

The pressure p_s generated by this source can be expressed as [26]:

$$p_s(\vec{r}) = \vec{f}(\vec{k}_s, \vec{k}_\imath) \cdot \frac{e^{i\vec{k}\vec{r}}}{\vec{r}}, \tag{2.15}$$

where the scattering amplitude $\vec{f}$ incorporates both the amplitude and phase of the scattered wave in the far field in the direction $\vec{k}_s$ when the target is illuminated by a plane wave propagating in the direction $\vec{k}_i$. Therefore the scattering amplitude $\vec{f}$ is a complete description of the scattering process when distance from the region where scattering takes place is large enough. Equation (2.15) is a definition of the scattering amplitude $\vec{f}$. However in practice scattering amplitude $\vec{f}$ often is an outcome of a scattering theory, and the pressure field in the far zone is then determined via (2.15).

It is customary to introduce several more measures of scattering called “cross sections” and “target strength”. Even though descriptions in terms of a cross section or a target strength is incomplete, it is often convenient and traditionally used.

First, for targets of finite extent it is appropriate to define a geometric cross section σ_g which is equal to the normal projection of the area of the target on the direction of incident wave propagation.

Then the scattering cross section σ_s is introduced as a measure of the equivalent source level of the scattered wave [26, 27]:

$$\sigma_s(\vec{k}_i) = \lim_{r\to\infty} \frac{W_s(\vec{k}_i)}{I_i}, \tag{2.16}$$

where I_i is the incident wave intensity, and W_s is the total power scattered, averaged in time, due to a plane wave incident from direction $\vec{k}_i$. Imagine the scattering process as an energy transfer from the incident to the scattered wave. Then the scattered power W_s is equal to the power carried by the incident wave in the absence of the target through its scattering cross section area σ_s. Hence, scattering cross section conveniently measures the effective geometrical cross section of the target as seen by the incident wave.

With σ_s so defined, the scattered mean square pressure at large distances from the target can be expressed as

$$p_s^2 = p_i^2 \cdot \frac{\sigma_s(\vec{k}_i)}{4\pi r^2} \cdot \frac{B_t^2(\vec{k}_s, \vec{k}_i)}{d_t(\vec{k}_i)}, \tag{2.17}$$

where $B_t^2(\vec{k}_s, \vec{k}_i)$ is a squared beam pattern of the effective scattering source, and directivity factor $d_t(\vec{k}_i) = 1/4\pi \cdot \oint B_t^2(\vec{k}_s, \vec{k}_i) d\vec{k}_s$ is a mean square beam pattern averaged over the entire angular space. Clearly, both values of the beam pattern and scattering cross section are required to describe the scattering. A convenient way to merge these two terms into one is to introduce the differential scattering cross section:

$$\sigma_d(\vec{k}_s, \vec{k}_i) = \lim_{r \to \infty} \frac{r^2 I_s(\vec{k}_s, \vec{k}_i)}{I_i}, \tag{2.18}$$

where I_s is the scattered wave intensity observed at range r in the direction $\vec{k}_s$ due to the plane wave propagating in the direction $\vec{k}_i$. Consequently, the scattered pressure at large distances from the target is given by:

$$p_s^2(\vec{k}_s, \vec{k}_i, r) = p_i^2 \cdot \frac{\sigma_d(\vec{k}_s, \vec{k}_i, r)}{r^2}. \tag{2.19}$$

Frequently in applications, bistatic scattering cross section and backscattering cross section are used along with the differential scattering cross section:

$$\begin{cases} \sigma_{bi}(\vec{k}_s, \vec{k}_i) = 4\pi\sigma_d(\vec{k}_s, \vec{k}_i), \\ \sigma_b(\vec{k}_i,) = 4\pi\sigma_d(-\vec{k}_i, \vec{k}_i). \end{cases} \tag{2.20}$$

Except for a scaling factor, bistatic and differential scattering cross sections can be used interchangeably. Backscattering cross section has a much more restricted meaning since only one direction is considered.

The other way of target description is found through its target strength defined as follows:

$$T(\vec{k}_s, \vec{k}_i) = 10 \log \left[\lim_{\vec{r} \to \infty} \frac{r^2 \cdot p_s^2(\vec{k}_s, \vec{k}_i, r)}{r_{ref}^2 \cdot p_i^2} \right], \quad dB\, re\, r_{ref}, \tag{2.21}$$

where usually the reference distance $r_{ref} = 1m$. Sometimes the target strength definition is restricted to backscattering only. Since I am generally interested in scattering into all directions, I shall use (2.21) as the target strength definition. Target strength so defined can be easily related to scattering cross sections, e.g.:

$$T(\vec{k}_s, \vec{k}_i) = 10 \log \frac{\sigma_d(\vec{k}_s, \vec{k}_i)}{r_{ref}^2}, \quad dB\, re\, r_{ref}. \tag{2.22}$$

Appropriate modification of (2.19) result in the following expression for sound pressure level in the scattered signal:

$$L_p(\vec{k}_s, \vec{k}_i, r) = 10 \log \frac{p_i^2}{p_{ref}^2} + T(\vec{k}_s, \vec{k}_i) - 10 \log \frac{r^2}{r_{ref}^2}, \quad dB\, re\, r_{ref} \& p_{ref}, \tag{2.23}$$

where the usual definition of the sound pressure level is used:

$$L_p = 10 \log \frac{p^2}{p_{ref}^2}, \quad dB\, re\, p_{ref}, \tag{2.24}$$

where in underwater acoustics $p_{ref} = 1 \mu Pa$.

Historically notation of target strength is preferred in acoustics, and scattering cross section is a conventional choice in electromagnetics. There is no reason beyond tradition to favor target strength, differential or bistatic cross section as a scattering descriptor.

Although all methods of target characterizations outlined here are frequently used interchangeably, only scattering amplitude is a complete descriptor. Neither cross section nor target strength carry information about the scattered wave phase. Frequently phase has no relevancy and can be safely ignored. However, not always is this the case. Careful examination of possible effects associated with phase change due to scattering is essential prior to use of target strength and scattering cross sections as descriptors of the scattering process.

2.4 Scattering from surfaces

The same approach used for targets can be used for characterizing scattering from surfaces and volumes. However such a treatment has a clear disadvantage. Within the boundaries of this approach, different segments of the same surface represent different targets, and target strength must be determined for each piece independently. This combines effects of the sonar system, propagation and scattering into one quantity, hence target strength is not a property of either the medium or of the surface only. A somewhat different approach can give a simpler result, if applicable.

Historically in underwater acoustics target strength T_s for scattering from the ensonified patch A of the rough surface is approached in the following way:

$$T_s(\vec{k}_s, \vec{k}_i, A) = S_s(\vec{k}_s, \vec{k}_i) + 10 \log \frac{A}{r_{ref}^2}, \quad dB\, re\, r_{ref}, \tag{2.25}$$

where scattering strength S_s is given by

$$S_s(\vec{k}_s, \vec{k}_i) = 10 \log \left[\lim_{r \to \infty} \frac{I_s(\vec{k}_s, \vec{k}_i) \cdot r^2}{I_i \cdot r_{ref}^2} \right], \quad dB. \tag{2.26}$$

Equivalently, S_s can be expressed in terms of cross sections, e.g.,

$$S_s(\vec{k}_s, \vec{k}_i) = 10 \log \frac{m_s(\vec{k}_s, \vec{k}_i)}{2\pi}, \quad dB\, re\, r_{ref}, \tag{2.27}$$

where m_s is a bistatic scattering cross section.

The form (2.25) is only useful if S_s does not depend on the ensonified area. Then scattering from a unit ensonified area of the surface can serve as a descriptor of surface scattering properties, which are now separated from the effects imposed by the sonar system and propagation contributing to the interrogated area A. In this case, assuming reference distance to be unity, forms (2.25)-(2.27) allow one to choose scattering strength per unit area S_s or bistatic scattering cross section per unit area m_s as a sole descriptor of the scattering process. Determination of S_s or m_s then constitutes the essence of the surface scattering theory.

However, the meaning of the resultant scattering strength is more restrictive then the meaning of the scattering cross sections (2.18, 2.20) and target strength (2.21). The simplifying assumption was made that the power scattered from a surface is simply proportional to the area contributing to the scattering. This in turn presupposes that scattering from different parts of the ensonified area are contributing to the target strength incoherently. Clearly, only random and very rough surfaces can posses such a property. Hence, neither smooth nor slightly rough surfaces can be adequately described by (2.25) unless S_s depends on the area A, which would violate the initial assumption and consequently make the form (2.25) useless.

Physically, describing scattering properties of the surface in terms of its scattering strength per unit area one is restricted to cases when incoherent scatter exceeds the coherent component. It is usually the case that incoherent scatter is formed when several independent scatterers are contributing to the received signal simultaneously. Then one can describe the combined scattering using the scattering strength per unit area notion. However each individual scatterer acts coherently, and there can be coherence between adjacent scatterers if they are close enough. Therefore, there is a transition at a specific scale. We can use S_s only if the scattering patch is large enough to encompass several scattering zones, and these zones are large enough so that adjacent zones contribute to the received signal incoherently. These coherent zones are usually associated with Fresnel zones (appropriate correction for roughness through the Rayleigh parameter implies, see Chapter 4). Therefore, only when several Fresnel zones are covered by the sonar footprint can we use S_s as a descriptor of scattering. It shows that even when applicable, S_s does not reflect the physics of the scattering process. It simply is an indicator of the fact that several major independent contributors can not be resolved using the current resolution. Physical processes underlying the scattering phenomena are coherent, and only low resolution of the experiment permits use of the S_s as the descriptor. Consequently, this means, that as sonar engineering progresses, the usefulness of S_s diminishes.

Such a limitation is not inherent when a description is made in terms of scattering cross sections and target strength. Coherent scattering is described in terms of σ and T as well as incoherent scattering. Any dependence of the scattered wave on the ensonified area can be described using σ and T. That makes scattering cross section and target strength more general (however, less convenient) descriptors.

2.4.1 Reverberation in underwater acoustics

The significance of reverberation is normally measured by an equivalent plane wave reverberation level RL defined as the level of the axially incident plane wave which produces the same hydrophone output as that produced by the received reverberation [4]. In order to compute RL, first the problem of sound propagation from the source to the scattering surface is solved to determine the interrogated area and the incident pressure level. Then S_s is determined from the properties of the surface using specific scattering models, and via (2.25) target strength is found. Finally, sound propagation to the receiver is calculated, leading to the value of the scattered sound pressure or intensity at the receiver location. The presence of several possible paths connecting source and receiver has to be accounted for in order to properly determine reverberation level.

However, expression (2.25) is inadequate for the description of high resolution surficial scattering. This in turn suggests that the classical treatment of the surficial reverberation using scattering strength per unit area as a parameter is inadequate. It can be used only when the sonar footprint is large enough, which is no longer true.

2.5 Summary

To conclude I would like to state some end results in a summarized format:

- Basic understanding of all aspects of sound under water (including propagation, noise, etc.) is essential to properly address scattering experiments.

- Ray acoustics is frequently an appropriate tool for modeling underwater sound propagation, and certainly the easiest one. Simplified forms (2.13) are an efficient way of modeling propagation away from caustics and turning points, i.e., within the first convergence zone for not very shallow grazing angles.

- Several measures of scattering are known. Of all, scattering amplitude (magnitude and phase) is a complete descriptor of the process. Scattering cross section and target strength can be used if phase of the scattered wave can be ignored. Scattering strength can be used when the experiment resolution is low enough, however it does not reflect the complete physics of the scattering process.

- Underwater reverberation ought to be understood through its components: propagation and scattering. The scattering part of the classical surficial reverberation theory is based on the use of scattering strength S_s, thus it is suitable for analysis of the incoherent part of the scattered field only.

Chapter 3

Rough Surfaces

3.1 General description of surfaces

Geometrically a surface in three dimensions is described by its distance $\varsigma(\xi, \eta)$ from a coordinate surface given by $\varsigma(\xi, \eta) = const$ [28]. Accordingly, this coordinate surface is referred to as a "mean" or "reference" surface. Then, in the Cartesian coordinate system (x, y, z) a surface is specified by its heights $z(x, y, t)$ above the "mean plane".

All natural surfaces are quite complicated in shape due to diverse physical reasons, or in other words rough. To a certain extent, the large scale surface shape characteristics can be measured, so some deterministic knowledge is available. Lacking precise knowledge about small scale features, however, one resorts to a statistical description.

Hence, a real surface always can be decomposed into a sum of two components (e.g., [29]):

$$z(x, y, t) = H(x, y, t) + h(x, y, t), \tag{3.1}$$

where H stands for the deterministic part of the surface, and h is a random statistical function of its arguments. The statistical part of the surface height h can be expressed employing standard measures of a stochastic function. Generally, the n-dimensional probability density

$$w_h^n(x_1, y_1, h_1; ...; x_n, y_n, h_n) \tag{3.2}$$

is a complete descriptor of a random function h as n approaches infinity. So an adequate description of a rough surface consists of the value H and n-dimensional probability density function for the h. In reality neither H nor w_h^n can be determined exactly, so certain approximations to real surfaces are accepted in order to proceed.

Other than specified by the (3.1) decomposition of the surface into its components can be performed. Often a "separation of scales" approach [2, 3, 30] is used to break surface roughness into its "large scale" and "small scale" components (see Chapters 4 and 7). Initially this method of surface decomposition was developed for cases when H consisted of scales too large to be of any interest at all in scattering applications. Then h was decomposed into its two components h_{large} and h_{small} to simplify the problem. However, ones ability to discard H is not a validity criterion for use of the separation of scales approach. These two methods of the surface decomposition can be successfully applied independently.

Sometimes in applications it is advantageous to realize that even when the surface in part is known deterministically, it is a deterministical knowledge about a particular realization of a stochastic process. In this case it is sometimes useful to extend the statistical description to scales normally known deterministically. It is especially used when average properties of the bottom are of interest (see Chapter 7 for more complete discussion on the surface decomposition in application to ocean bottom scattering).

3.2 Statistical description of natural surfaces

Equivalently to its description in terms of the probability density, h can be characterized through an infinite number of its moments. The first and second moments frequently used in scattering are defined as follows:

$$\langle h(\vec{r}_\perp)\rangle \equiv \langle z(\vec{r}_\perp)\rangle = \int_{-\infty}^{\infty} z \cdot w_1(\vec{r})dz, \tag{3.3}$$

$$\left\langle h^2(\vec{r}_\perp)\right\rangle \equiv \left\langle z^2(\vec{r}_\perp)\right\rangle = \int_{-\infty}^{\infty} z^2 \cdot w_1(\vec{r})dz, \tag{3.4}$$

where $\langle h(\vec{r}_\perp)\rangle$ is the mean surface height above the reference plane, $\langle h^2(\vec{r}_\perp)\rangle$ is the variance of heights relative to the reference plane, $\vec{r} = (x, y, z)$ and $\vec{r}_\perp = (x, y)$.

Conventionally the reference plane is chosen so that mean height and mean slope are both equal to zero, and the standard deviation of height (often called "root mean square height" in underwater acoustics, abbreviated as "rms height"), is used instead of variance as a descriptor of the surface:

$$h_{rms}(\vec{r}_\perp) = \sqrt{\langle h^2(\vec{r}_\perp)\rangle}. \tag{3.5}$$

Some qualitative understanding of rough surface scattering is obtained with the rms height alone. However, a better description is achieved if higher moments are considered. The correlation function B_h and power spectral density $\tilde{W}_h$ of surface heights play an extremely important role in surficial scattering. By definition the correlation function of the surface heights is

$$B_h(\vec{r}_{\perp,1}, \vec{r}_{\perp,2}) = \int_{-\infty}^{\infty} z_1 z_2 w_2(\vec{r}_1, \vec{r}_2)dz_1 dz_2. \tag{3.6}$$

Consider now a realization of a rough surface $z = \varsigma(\vec{r}_\perp)$. This realization can be expanded into the Fourier integral:

$$\varsigma(\vec{r}_\perp) = \int_{-\infty}^{\infty} \tilde{Z}(\vec{K}) \cdot e^{i\vec{K}\vec{r}_\perp} d\vec{K}, \tag{3.7}$$

where $\tilde{Z}(\vec{K})$ is the complex random amplitude of a plane wave component in the expansion, having surface wave number $\vec{K} = (K_x, K_y)$. Then the spectral power density is simply

$$\tilde{W}_h(\vec{K}) = \left\langle \tilde{Z}(\vec{K}) \cdot \tilde{Z}^*(\vec{K}) \right\rangle. \tag{3.8}$$

3.3 Spatially stationary stochastically rough surfaces

An appreciable simplification is accomplished when spatial stationarity of the surface statistics can be assumed. Generally, the spatial stationarity assumption does not require temporal independence. A case of stationary in space time-dependent surfaces can be considered (for example, see [31, 5]). For instance, time dependence is important when scattering from the ocean surface is considered. However, since I am interested in the ocean bottom, the more restricted case of fixed in time can be considered.

In this case the correlation function depends only on the distance $\vec{R}$ between $\vec{r}_{\perp,1}$ and $\vec{r}_{\perp,2}$. Thus

$$B_h(\vec{r}_{\perp,1}, \vec{r}_{\perp,2}) = B_h(\vec{R}), \tag{3.9}$$

where $\vec{R} = \vec{r}_{\perp,1} - \vec{r}_{\perp,2}$, and the spectral power density becomes a Fourier counterpart of the correlation function:

$$\begin{cases} B_h(\vec{R}) = \int_{-\infty}^{\infty} \tilde{W}_h(\vec{K}) \cdot e^{i\vec{K}\vec{R}} d\vec{K}, \\ \tilde{W}_h(\vec{K}) = (2\pi)^{-2} \int_{-\infty}^{\infty} B_h(\vec{R}) \cdot e^{i\vec{K}\vec{R}} d\vec{R}. \end{cases} \tag{3.10}$$

Mean, mean square, and rms height become independent of coordinates and can be easily expressed in terms of the correlation function or the spectral power density. For example, the mean square height now is simply

$$\left\langle h^2 \right\rangle = B_h(0) = \int_{-\infty}^{\infty} \tilde{W}_h(\vec{K}) d\vec{K} = const. \tag{3.11}$$

Clearly, the correlation function and the spectral power density can be used interchangeably as equivalent descriptors of the surface statistics. However the validity of this statement is restricted to the particular case of stationary surfaces.

Unless an infinite number of moments is considered, the description of a surface through its moments is incomplete. Characterizing a surface with second order statistics alone (correlation function or power spectrum) yields an approximation to real surfaces.

However, a large class of mathematical surfaces is fully defined by their first and second moment. These surfaces are referred to as "Gaussian" or "normal" and play an extremely important role in surface scattering theory. By definition a surface is normal if its n-point probability density of deviations of the surface from the mean plane is given by the normal law for any n. The central limit theorem of statistics assures that physical surfaces formed under influence of many independent additive factors are normal. Hence often a normal mathematical surface is an adequate approximation to a real surface.

3.4 Nonstationary stochastically rough surfaces

With a few exceptions, a stationary surface can be modeled as normal so that second order statistics is sufficient for its description, thus tremendously simplifying development of a scattering theory. However the convenient assumption of stationarity in reality is inadequate for natural phenomena. Often different parts of the surface were formed under very different conditions. Hence only locally can the surface be considered stationary.

As a result, the roughness parameters of the ocean bottom, like rms roughness and slope, correlation length etc., depend on the scale considered and on the geographic location of the experiment. For instance, in [32] measurements of the rms roughness on the bottom along a straight line path of length L_0 were analyzed for $10^{-1}\,km \leq L_0 \leq 10^2\,km$. It was shown that on these observation scales, the variance of the sea floor roughness is linearly proportional to the length scale L_0 involved:

$$\left\langle h^2 \right\rangle = C \cdot L_0, \tag{3.12}$$

where C is an empirical constant possibly depending on the geographic location and on the direction of the chosen path. It was also noted [33] that the one-dimensional power spectral density of ocean bottom roughnesses follows the so-called power law:

$$\tilde{W}_h(K) = \frac{F_0}{K^2 + K_{out}^2}, \tag{3.13}$$

where F_0 and K_{out} are parameters of the model, K is surface wave number, and the one dimensional power spectrum of the surface roughness $\tilde{W}_h(K)$ is calculated along a straight line. It is worthwhile to mention here that both model parameters, F_0 and K_{out}, are generally dependent on the path length L_0, with K_{out} asymptotically decreasing to a particular value as L_0 increases.

3.5 Fractal surfaces

Empirical observations summarized in the previous section are consistent with the idea of modeling one-dimensional cuts through the ocean bottom as a simple self-affine fractal stochastic process [34, 35, 36, 37]. However, "true fractals" exhibit power law behavior on all scales, but natural surfaces never do. First, there is a welll-known "cut-off" of roughness for large scales due to non-vanishing K_{out}. Second, natural surfaces tend to have less roughness for smaller scales [36]. This result in a change of the power law exponent at some value K_{in}, which usually happens at the *mm* scale (Fig. 3.1). Thus only for K ranging between K_{out} and K_{in} can a rough surface be modeled as a simple fractal. An analogy with turbulence [38, 39] suggests the designation of K_{in} and K_{out} as inner and outer limits of fractal behavior, respectively.

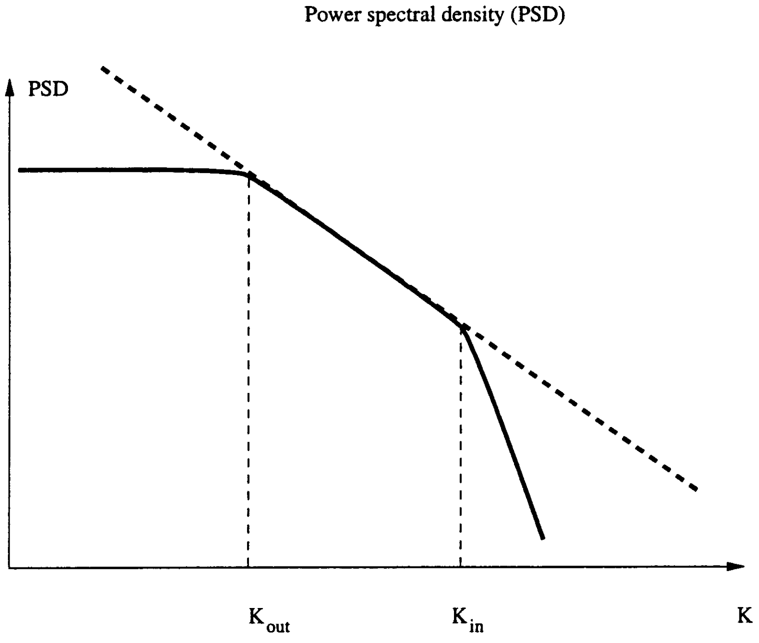

Figure 3.1: Power spectral density (PSD) of a natural surface as a function of the horisontal wavenumber. Cut-off at K_{out} and change of the fractal dimension at K_{in} are shown. Dashed line shows the simple self-affine fractal PSD

3.5.1 Two-dimensional fractals

An appropriate generalization of (3.13) for two-dimensional anisotropic roughness was developed by Goff and Jordan [29, 40]. Their model was applied to the problem of sound scattering from a rough ocean floor [41, 42, 43]. In this model, the rough surface is assumed to be a realization of a Gaussian zero-mean two-dimensional stochastic process having a "Goff-Jordan" power spectral density in the form

$$\tilde{W}_h(\vec{K}) = 4\pi\nu h_{rms}^2 \cdot \left|\vec{Q}\right|^{-1/2} \cdot \left[\vec{u}^2(\vec{K}) + 1\right]^{-\nu+1}, \tag{3.14}$$

where $\nu = 3 - D$ is related to the fractal (Hausdorff) dimension D, and $\vec{u}$ is a dimensionless norm of $\vec{K}$: $\vec{u}(\vec{K}) = \left[\vec{K}^T\vec{Q}^{-1}\vec{K}\right]^{1/2}$. Anisotropy enters the model through the dimensionless ellipsoidal (Riemannian) norm $\vec{R}(\vec{r}_\perp) = \left[\vec{r}_\perp^T\vec{Q}\vec{r}_\perp\right]^{1/2}$, where Q is a positive-definite, symmetric matrix whose elements have the dimension of $(length)^{-2}$, which can be expressed in terms of its eigenvalues K_n^2 and K_s^2 and normalized eigenvectors $\vec{e}_n$ and $\vec{e}_s$: $\vec{Q} = K_n^2\vec{e}_n\vec{e}_n^T + K_s^2\vec{e}_s\vec{e}_s^T$.

For the case of isotropic roughness (3.14) can be reduced to an equivalent of (3.13):

$$\tilde{W}_h(\vec{K}) = 4\pi\nu h_{rms}^2 \cdot K_0^{-1} \cdot \left[\frac{K^2}{K_0^2} + 1\right]^{-(\nu+1)}, \tag{3.15}$$

where $K_0 \equiv K_{out}$ is the outer scale of a fractal, and K is the absolute value of surface wavenumber $K = \left|\vec{K}\right|$. Clearly, a Goff-Jordan surface exhibits fractal behavior on all scales between K equal to K_0 and infinity.

3.5.2 Moments of the fractal stochastic process

By the choice of reference plane, the mean height and slope are both equal to zero. The power spectrum density in the form (3.13), (3.14) and (3.15) allow easy calculation of various moments observed in the ocean. For example, square values of rms roughness h_{rms}, rms slope s_{rms}, and correlation function of heights B_h, are given by

$$\begin{aligned} h_{rms}^2 &= \textstyle\int_{K_{min}}^{\infty} \tilde{W}_h(\vec{K}) d\vec{K}, \\ s_{rms}^2 &= \textstyle\int_{K_{min}}^{\infty} K^2 \cdot \tilde{W}_h(\vec{K}) d\vec{K}, \\ B_h(\vec{R}) &= \textstyle\int_{K_{min}}^{\infty} \tilde{W}_h(\vec{K}) \cdot e^{i\vec{K}\vec{R}} d\vec{K}, \end{aligned} \tag{3.16}$$

respectively.

In (3.16) the finite nature of experimental data is accounted for by introduction of scales $K_{min} = 2\pi/L_0$, corresponding to the maximum scale L_0 (size of inhomogeneous patch, size of sonar footprint on the bottom, etc.) encountered in the experiment.

In the case of anisotropic roughness one expects to see an anisotropic correlation function. However, an important feature of (3.16) is that anisotropic behavior can be seen also in the case of purely isotropic roughness (3.15), due to anisotropy in the footprint shape. Also it is clear that rms slope is unbounded, unless the power spectral density decays faster then K^{-4} for large absolute values of surface wavenumber $K \to \infty$. Since the observed decay rates fall in between K^{-2} and K^{-3} on the $10^{-2} - 10^{2}$ km observation scale [32, 33, 36, 37], the inner fractal scale must yield a physically meaningful bounded value of rms slope, or discontinuous surfaces must be dealt with.

It highlights an interesting feature of natural surfaces. It is intuitively clear that discontinuities are only important in scattering when they are comparable to the wavelength. Scattering from discontinuous surfaces was considered and it was found numerically that discontinuities can be rounded, or, in other words, infinite Fourier series representation of the surface can be truncated at a certain value of surface wave number large compared to the incident wave number [44]. It also means that we can truncate integrals in (3.15) at some value of $\left|\vec{K}\right| >> k_i$ and it must have no effect on parameters relevant to the scattering, since the exact behavior of the surface wave number spectrum $\tilde{W}_h(\vec{K})$ at large values of $\vec{K} \to \infty$ does not affect surface scattering properties. As one can see from (3.16), for observed decay rates rms roughness is insensitive to such a truncation, hence it is a robust descriptor of the surface roughness. The same can not be said about the rms slope. Hence applicability of any scattering theory that makes use of the rms slope is limited. In other words, a good scattering theory for rough ocean bottoms must be able to deal with discontinuous surface slopes, either through use of appropriate mathematics, or by employing physical considerations.

Chapter 4

Scattering from Spatially Stationary Surfaces

Truly stationary surfaces hardly exist, yet often a local stationarity assumption can suffice in practice, i.e., any fraction of the surface can be considered as a stationary stochastic process having a locally constant mean, standard deviation, etc. The fact that stationarity notably simplifies the problem explains why so much attention has been devoted to scattering from such surfaces.

Some approaches presented in this chapter do not make explicit use of the surface statistics, instead they operate with integral measures of surface shape like rms roughness. Still, applicability of these methods to scattering from real (nonstationary) surfaces has to be carefully evaluated on a case-by-case basis prior to use.

4.1 The general scattering problem

The boundary value problem

The idealized scattering problem for a bounded volume of fluid consists of the wave equation for the scalar potential inside the volume, and the appropriate boundary conditions. Often a Fourier transform is applied to the wave equation to simplify the problem. The result (the Helmholtz equation) takes the form [15, 45, 25]:

$$\nabla^2\Phi + k^2\Phi = 0, \tag{4.1}$$

where $k = \left|\vec{k}\right|$ is the wave number and Φ is the complex amplitude of the acoustic potential, respectively, and a time dependence term $e^{-i\omega t}$ is implied. Appropriate boundary conditions should be defined in order to complete (4.1).

If a fluid half space is considered instead of a closed volume, the radiation boundary condition $\Phi(|\vec{r}| \to \infty) = 0$ is necessary to uniquely determine the solution.

On the scattering interface Dirichlet, Neumann or more inclusive impedance boundary conditions are often used, mainly due to their relative simplicity. The generalized impedance boundary condition is written in the form

$$\left[\xi\frac{\partial\Phi}{\partial\vec{n}}+\Phi\right]_A=0, \tag{4.2}$$

where A is the scattering interface, and the parameter ξ is related to the acoustic impedance of the surface. Generally ξ is a frequency dependent complex quantity.

The major limitation associated with the use of the impedance boundary condition is its local nature [15, 21, 13]. Using (4.2) implies that the acoustic motion at each point on the surface is independent of motion of surrounding points. Unfortunately, this is not generally true for the ocean bottom. For instance, consider the case of a scattering interface that supports acoustic waves (e.g., fluid-elastic interface). Then motion of different surface points will be related through these wave motions, thus making the boundary condition (whatever it is) non-local. The applicability of Dirichlet or Neumann boundary conditions is even more limited.

Other kinds of boundary conditions are also occasionally used (e.g., smoothed boundary condition [46, 47, 48, 49, 50])

Since there is only one equation, solving it with appropriate boundary conditions seems mathematically appealing. However the applicability of this approach is limited by ones ability to determine the appropriate boundary condition, which in the general case is difficult to do.

An alternative approach is to consider the entire space. Then the problem of scattering from the surface considered consists of two half spaces of different media, and the scattering surface is represented by an interface between these half spaces [15]. Usually boundary condition relating acoustic motion across the interface can be determined from physical considerations.

In the simplest case where each half space is filled with a fluid, two linear homogeneous wave equations for scalar acoustic potential $\Phi_{1,2}$ (or for pressure $p_{1,2}$) at opposite sides of the interface are to be determined. Physical considerations on pressure and normal velocity continuity across the interface

$$[p_1 = p_2]_A \, , \quad [v_{1n} = v_{2n}]_A \, , \tag{4.3}$$

are applied to solve for $\Phi_{1,2}$. That is, the wave equations for the scalar potential are coupled through the condition (4.3).

The scattering problem becomes much more complicated if the more general case of a fluid-elastic interface is considered [13]. Then in addition to the scalar potential Φ the vector potential Ψ has to be introduced, resulting in three additional coupled scalar wave equations for its three components. In turn boundary conditions (4.3) are replaced by the more general requirement of continuity of the stress components across the interface, as well as normal velocity.

4.1.1 The integral equation formulation

Sometimes it is more convenient to confront an integral equation instead of solving the differential equation plus boundary conditions. Equivalently, when the entire space has to be considered in order to define applicable boundary conditions, two coupled integral equations are defined on opposite sides of the interface.

The acoustic field everywhere can be expressed in terms of the Helmholtz integral equation [15, 13]:

$$\Phi(\vec{r}) = \Phi_i(\vec{r}) + \int_A \left\{ \Phi(\vec{r}_0) \cdot \frac{\partial G(\vec{r}, \vec{r}_0)}{\partial \vec{n}_0} + G(\vec{r}, \vec{r}_0) \cdot \frac{\partial \Phi(\vec{r}_0)}{\partial \vec{n}_0} \right\} dA, \tag{4.4}$$

where Φ_i is the incident acoustic potential, Φ is the total (incident plus scattered) acoustic potential, A is a surface of integration, $\vec{n}_0$ is the local normal to that surface, $\vec{r}_0$ represents position on the surface, and $G(\vec{r}, \vec{r}_0)$ is the Green's function for an unbounded medium given by

$$G(\vec{r}, \vec{r}_0) = \frac{1}{4\pi} \cdot \frac{e^{i\vec{k}|\vec{r}-\vec{r}_0|}}{|\vec{r} - \vec{r}_0|}. \tag{4.5}$$

Integral (4.4) can be evaluated over any surface A. If a surface can be found on which the acoustic potential and its normal derivative are known simultaneously, (4.4) allows one to find the acoustic field everywhere in three-dimensional space. However, simultaneous determination of Φ and $\partial\Phi(\vec{r}_0)/\partial\vec{n}_0$ is seldom possible. The usual way to find the solution is to evaluate (4.4) over the scattering interface and to apply appropriate boundary condition.

4.2 Rayleigh parameter

The integral equation sets up the mathematically precise scattering problem. However, only in the simplest cases is an analytical solution possible. Instead, approximate or numerical solutions of (4.4) are normally considered to solve the scattering problem. A simple qualitative consideration helps one to enter the realm of approximate solutions.

All surfaces are complicated in shape, i.e., in some sense rough. However, usually the distinction is made between rough and smooth surfaces. The basis for the differentiation is purely qualitative. When most scattered energy is directed into the specular direction, the surface is referred to as "smooth", and scattering is termed "coherent". Conversely, if a significant part of the scattered energy is directed away from the specular direction, the surface is rendered "rough", and the scattering is denoted as "diffuse", or "incoherent". This clearly indicates that surface can be considered neither rough nor smooth. The demarcation between rough and smooth is a function of surface properties and characteristics of the incident field, taken together.

Conventionally the surface is considered smooth, or at most slightly rough, if its rms roughness satisfies

$$h_{rms} << \frac{\lambda}{8 \sin \theta}, \tag{4.6}$$

where λ and θ are the wavelength and grazing angle, respectively. This inequality is known as the Rayleigh criterion, and the value

$$\gamma = \frac{8 \sin \theta \cdot h_{rms}}{\lambda} \tag{4.7}$$

is called the Rayleigh parameter [10, 15]. Thus if the Rayleigh parameter is $\gamma = 0$, the interface is flat, if $\gamma << 1$ the interface is slightly rough, and $\gamma \geq O(1)$ characterizes rough surfaces.

It is interesting to point out the meaning of the phenomenological coefficient 8 in the (4.7). It is well known that in the perturbation solution of the scattering problem (see following sections on small perturbation) the expansion parameter is $k_z h$, where k_z is the vertical component of the incidence wavenumber. Since $k = 2\pi/\lambda$, the expansion parameter becomes

$$\frac{2\pi \sin\theta}{\lambda} \cdot h. \tag{4.8}$$

This shows the relation between smallness of the Rayleigh parameter and ones ability to use the low order perturbation solutions, and highlights the physical meaning of the Rayleigh parameter as an expansion parameter in the small perturbation solution technique.

Knowledge of the Rayleigh parameter alone rarely allows a satisfactory description of the scattering, however it helps to choose an approach and gives some qualitative prediction of the scattering.

4.3 Approximate solution of the scattering problem

4.3.1 Scattering from surfaces having a small Rayleigh parameter value: perturbation approach

Scattering from a flat interface

Even though there are no flat interfaces in the real ocean, due to its simplicity and analytical tractability this case plays an important role in developing understanding. It also can be considered as a limiting case of a very smooth surface when the Rayleigh parameter approaches zero. For example, in the easiest case of two half spaces of fluid with densities $\rho_{1,2}$ and sound speeds $c_{1,2}$ separated by a smooth plane interface, solution for the total acoustic field consists of three waves: an incident wave with complex amplitude of pressure p_i, a scattered wave p_s and a transmitted wave p_t. Incident and scattered waves exist in one half space, and transmitted in the other. By definition, reflection and transmission coefficients are given by $\mathcal{R} = p_s/p_i$ and $\mathcal{T} = p_t/p_i$, respectively. In this case scattering is completely defined by the two complex coefficients $\mathcal{R}$ and $\mathcal{T}$, and the total field in both fluids can be found as a superposition of incident, scattered and transmitted waves:

$$\begin{cases} p^{(1)} = p_i + p_s = (1 + \mathcal{R}) \cdot p_i, \quad fluid\ 1, \\ p^{(2)} = p_t = \mathcal{T} \cdot p_i, \quad fluid\ 2, \end{cases} \tag{4.9}$$

where bracketed superscripts (1) and (2) refer to upper and lower fluids, respectively, and the incident wave is coming from the upward direction.

Scattering from slightly rough surfaces

Naturally, the next case to consider is a slightly rough surface $\gamma << 1$. The small parameter in roughness allows a variety of perturbation solutions. Normally all parameters are expanded into a series where successive terms are of the same order of magnitude multiplied by a small parameter ϵ:

$$\xi = \xi_0 + \epsilon\xi_1 + \epsilon^2\xi_2^2 + ..., \ \ \xi_0 = O(\xi_1) = O(\xi_2) = ..., \ \ \epsilon << 1. \tag{4.10}$$

Then a succession of equations, or a successive order of approximation, is formed collecting terms with the same power of ϵ. When the perturbation parameter ϵ is very small, only the few first orders contribute to the solution, thus making possible an analytically tractable perturbation solution.

Classical small perturbation technique

The usual way to use expansion (4.10) is to insert it into the wave equation and boundary conditions. Consequently, the solution for the pressure potential in fluids (1) and (2) takes in the form [31, 51, 52]:

$$\Phi^{(1),(2)} = \Phi_0^{(1),(2)} + \epsilon\Phi_1^{(1),(2)} + O(\epsilon^2) + \ldots , \tag{4.11}$$

where $\epsilon = k_z h$. Boundary conditions defined on the rough interface in the form (4.3) are subsequently expanded into the Taylor series near $h = 0$. The next step is to substitute solution (4.11) into the boundary conditions and collect terms of the same order of magnitude [31, 5, 13]. In each successive step of the solution, the wave equation with specified boundary conditions is solved. However, via the Taylor expansion, boundary conditions are mapped on a flat plane, so the initial problem of scattering from the irregular surface is substituted with the succession of flat surface scattering problems, each having an analytical solution.

Since the zero order solution satisfies boundary conditions on the flat surface, it is given by (4.9). After collecting first order terms one ends up with an equation where the value of the first order field on the flat plane is related to the shape of the rough surface and the value of the zero order field on the surface. Again, since the value of the first order field is known on the plane, a full space solution can be derived via the integral equation (4.4) using formulas (4.9). This situation may be thought of as flat interface scattering which generates the zero order solution plus additional sources located on the flat interface, generating the first order solution. Conventionally these sources are referred to as "virtual" or "equivalent" sources. Knowing these sources, one can construct the solution via an integral equation as a summation of individual source contributions.

Clearly, applicability of the first order perturbation solution is limited to slightly rough surfaces with small rms slope and rms heights. Additionally, it does not account for multiple scattering effects. However, the first order perturbation is robust and does not make explicit use of the smallness of slopes criterion.

Higher order perturbation (e.g., by Howe [53, 54, 55] or Thorsos [56, 6]) takes into account multiple scattering effects and stresses their significance at small grazing angles. However, these solutions are still limited to moderate heights and small slopes. For larger values of surface slopes, convergence of the perturbation series may become non-uniform. For instance, a second order solution by Howe diverges, and in the solution by Thorsos [56] when the four first terms were considered two higher order terms in the expansion have greater absolute value then the first term, but an opposite sign, so that they cancel each other. Since a good match with a numerical solution of the integral equation was achieved using the first four terms, it was further concluded that "sixth- and higher-order terms essentially cancel, since they are not needed to give agreement with exact result". Yet there is no analytical basis for this conclusion. This indicates a potential problem one can encounter with a higher order perturbation expansion. Generally, higher order perturbation terms contain higher order derivatives of the surface roughness. And even the first derivative of the surface roughness can be discontinuous. Since surface slopes are brought into the consideration, only particular behavior of the roughness at high surface wave numbers is allowed. So for instance, σ^{22} of [56] computed for a one-dimensional surface has a bounded value only if the roughness spectrum decays faster then $K^{-1.5}$. For comparison, in [44] the power spectra with decay rates proportional to K^{-1} were successfully considered using the integral equation formulation.

Boundary operator expansion technique

This recently introduced technique [57, 58] is closely related to the boundary integral method ([59]. An analytical solution for the first order perturbation field is considered that incorporates effects of elasticity. As usual, the flat surface solution is a zero order approximation. However, now an elastic surface, or in the more general case, a succession of flat elastic layers, is considered. Virtual sources on each interface are computed to account for the elastic properties of the medium, and the solution is obtained via the integral equation as a summation of individual source solutions.

This technique is still restricted to surfaces with not too large rms heights. If other than horizontal interfaces are encountered, the solution domain has to be divided into a sequence of segments, each segment having a locally flat interface [60, 61]. Then the solution is obtained in each segment, and matched through a global inversion technique, which increases the required computation time. But since elasticity is accounted for, this technique is powerful for modeling of high resolution rough elastic ocean bottom scattering experiments.

4.3.2 Scattering from gently undulating surfaces (Kirchhoff approximation)

An other way to introduce a small parameter into the governing equation comes about if the surface slopes are gentle. It results in the so called "Kirchhoff" or "tangent plane" approximation [5, 62, 63, 64], by far one of the most used techniques in solution of scattering problems when not very shallow grazing angles are considered. In this method it is assumed that the scattering surface is so smooth that at each point the entire field can be accurately represented as a sum of the incident field and the field reflected from the local tangent to the surface plane according to the plane interface solution formulas. Since now both the acoustic field and its derivative are defined on the scattering surface, a solution for the entire space can be obtained via the integral equation (4.4). The general applicability condition for the Kirchhoff approximation can be stated as

$$ka \sin \theta >> 1, \qquad (4.12)$$

where k is the absolute value of the incident wave wavenumber, a is a characteristic radius of curvature, of the surface, and θ is the grazing angle. This clearly limits the approximate technique to gently sloping surfaces and to steep incidence and scattering angles θ.

Since the Kirchhoff approximation is valid for gently sloped surfaces only, scattering from small scales can not be accounted for. If additionally to slopes, surface heights are also small, both Kirchhoff and perturbation theories may be valid. When both are valid, numerically better performance is usually achieved using the Kirchhoff approximation [65, 56] than the first order perturbation expansion. With the introduction of an appropriate shadowing function, a second order Kirchhoff approximation can account for multiple scattering, hence for such effects as enhanced backscattering [62, 66, 67, 68]. Unfortunately, as incidence or scattering grazing angle decreases, Kirchhoff theory quickly become inapplicable and quantitative performance of the solution degrades.

4.3.3 Scattering from rough surfaces

Scattering from surfaces that are in some way smooth (e.g., small slopes, small heights from the reference plane compared to the incident wavelength, or both) represent the most developed part of scattering theory. However, experiments on scattering from natural surfaces often do not comply with applicability limits of smooth surface scattering theories. Thus one needs a scattering theory applicable to large roughness.

Boss scattering theory

Within this approach, the scattering surface is first modeled as a collection of simply shaped three-dimensional objects on a flat base plane [46, 69, 48, 49, 70, 71, 72]. Then a precise solution for the scattering can be derived in closed form.

Boss theory entails no small parameter, hence in theory large roughness can be described with the same degree of success as small roughness. However, the boss approximation is seriously limited by the ability to model a real surface as a collection of bosses. Any chosen expansion of a real surface as a collection of bosses is often inadequate. It results in shrinking the applicability domain of the boss theory. A certain degree of success has been reached in cases where the actual roughness appears as a collection of well defined deterministic shapes, or is small enough and appears in clusters. For example, in under ice scattering large well defined ice ridges with smaller keels superimposed were modeled as a collection of two boss types, one being an infinite cylinder, and the other a hemisphere or semiellipsoid [47, 73, 74]. However, surface expansions of this type are hardly possible for the ocean bottom and in this case boss theory will be difficult to apply.

Lambert's Law

Lambert's Law was an early method used to describe scattering in underwater acoustics [4], and it remains by far the one that is most used for this purpose. It has its origin in optics [75]. The idea underlying this scattering theory is fairly simple. The surface is assumed to be very rough, so that the local grazing angle between the incident field and scattering surface is uniformly distributed over all values. Then it is intuitively clear that each small piece of the surface scatters incident energy into all directions with equal probability. The total energy scattered by a piece of the surface is then proportional to the amount of energy incident on it, and to the apparent area of the piece as seen by the observer. Since part of the energy can be lost during the interaction, conservation considerations then result in the simple form for the scattering strength:

$$S_s = \mu \sin\theta_i \sin\theta_s, \tag{4.13}$$

where as usual θ_s, θ_i are scattered and incidence grazing angles, and μ is a constant dependent on the amount of energy lost in the interaction. If no losses are presented, $\mu = 1/\pi$.

When Lambert's Law is used in optics, the quantity $\pi\mu$ is usually called the albedo of the surface. In underwater acoustics the coefficient μ has its own name: it is usually referred to as the Mackenzie coefficient. The value of the Mackenzie coefficient for Lambert's Law is related to the amount of energy lost from the interaction between the incident wave and the surface, and can be predicted knowing scattering surface properties.

Lambert's Law is rigorously applicable to cases where the scattering surface is extremely rough. With modifications [76, 77, 78, 79, 80, 81], it demonstrates excellent performance in optics, including the appearance of the moon disk. The only visible discrepancy exists between theory and experiment in the exact backscattering direction, since a coherently enhanced backscattering effect is not accounted for [78].

Initially good performance of Lambert's Law was reported in underwater acoustics [4, 9, 82]. However, in these experiments the ensonified patch on the bottom was large and the rms roughness measured in the sonar footprint exceeded by many times the incident wavelength. Also, most early work was restricted to backscatter, so that the full bistatic angle dependence in Lambert's Law was not tested; at best data were matched with the adjustable Mackenzie coefficient to test the theory. In particular, a Mackenzie coefficient in the range from 0.1 to 0.001 was often used. With the increasing resolution of contemporary experiments, the sizes of the scattering patches decrease. Since the real ocean bottom exhibits fractal properties on scales encountered currently in underwater acoustics, smaller patch size results in smaller roughness within the footprint, hence degradation of Lambert's Law performance is expected. Yet because of its simplicity it is still widely used to predict scattering in underwater acoustics. However, when Lambert's Law is inapplicable, it tends to greatly overpredict scattering away from the specular direction, and underpredict the specularly scattered field. To compensate for it, a phenomenological coefficient is introduced (which traditionally is still called Mackenzie coefficient, but has nothing to do with amount of energy lost in the interaction). This coefficient in general depends on the incidence grazing angle, scattering grazing angle and the bistatic angle. Because of this, all scattering properties are effectively incorporated into it. Within this approach there is no known way to deduce the values of this coefficient for different angles from fundamental physical principles. It has to be measured experimentally. For instance, for backscattering Mackenzie coefficient from 0.001 to 0.1 is used. This result in the improved fit to backscattering data, however, model performance in the forward direction degrades even further.

Two-scale models

This method was first introduced by Kuryanov and, with certain modifications, is widely used since then [7, 83, 84, 85, 51, 2, 3, 30]. The irregular rough surface is assumed to be in the form of a superposition of small disturbances h on a gently undulating surface H. Plane wave incidence is usually considered. The perturbation expansion solution in the form (4.10) is inserted into appropriate boundary conditions. Then, as in the standard perturbation approach, boundary conditions are expanded into a Taylor series. However, now the expansion is made around the smooth surface H instead of doing it around the flat reference plane. Collecting terms of the same order in ϵ, successive solution orders can be derived. In this way the initial problem is reduced to solving the wave equation with certain boundary conditions defined on the smooth but undulating surface H.

For a general surface H the scattering problem with general boundary conditions can not be solved. However, since the surface is assumed to be gently undulating, at each step the Kirchhoff approximation can be invoked. To make the problem analytically tractable, the expansion is usually made to first order only.

If the initial surface is stochastic in nature, then averaging over realizations of h has to be performed. It is usually safe to assume that height variations on the small scale h are independent of those on the large scale H. Then averaging can be performed independently, and the resultant scattering cross section σ can be represented as a sum of two terms

$$\sigma = \sigma_1 + \sigma_2, \tag{4.14}$$

where σ_1 and σ_2 are outcomes of zero and first order solution, respectively. The zero order solution is found by solving the scattering problem for the smooth surface H with the original boundary conditions. The first order solution can then be shown to be an average of the small perturbation solution over all slopes present in the smooth surface H.

Two-scale theories were built to broaden the domain of the small perturbation solution. They are a mixture of the Kirchhoff solution and the small perturbation solution, and hence have inherent limitations [86, 87]. Generally, four conditions have to be satisfied. First, the surface must be "separable" into two scales. Second, slopes of large scale irregularities contributing to the composition of the rough surface must be "gentle enough" so that Kirchhoff theory is applicable. Third, slopes and heights of small scale irregularities must be small enough to allow a perturbation solution. And finally, there must be an overlap between applicability domains of solutions for large and small scales. Mathematically for stochastically rough surfaces with power spectrum of irregularities $\tilde{W}_h$, the restrictions are [88]:

$$\begin{aligned} &(kh_{rms})^2 << 1, \;\; h_{rms}^2 = \tfrac{1}{2} \cdot \textstyle\int_{K_{small}} \tilde{W}_h(\vec{K}) d\vec{K}; \\ &s_{rms}^2 << 1, \;\; s_{rms}^2 = \tfrac{1}{2} \cdot \textstyle\int_{K_{small}} \vec{K}^2 \tilde{W}_h(\vec{K}) d\vec{K}; \\ &(ka)^{1/3} >> 1, \;\; \tfrac{1}{a^2} = \tfrac{1}{2} \cdot \textstyle\int_{K_{large}} \vec{K}^4 \tilde{W}_h(\vec{K}) d\vec{K}; \end{aligned} \tag{4.15}$$

where h_{rms} and s_{rms} are rms height and slope, k and $\vec{K}$ are incident and surface wave number, a is the characteristic (rms) radius of curvature, and the entire surface wavenumber domain can be constructed by addition of overlapping small and large scale roughness domains K_{small} and K_{large}, respectively.

A somewhat different modification of this method was proposed in [89]. Instead of using the small perturbation solution for the surface h, modification of Lambert's Law is used. The solution is thus a superposition of the Kirchhoff solution for the gentle surface H and Lambert's Law solution for small scale roughness h, averaged over large scale surface slopes.

But Lambert's Law can be applied to large roughness surfaces only, and rapidly becomes inapplicable as the Rayleigh parameter decreases. To account for it, the Mackenzie coefficient is chosen as a free parameter to adjust the "theory" to the experiment. This highlights an essential weakness of this approach.

4.4 Applicability of scattering theories to underwater scattering and reverberation: summary comments

The integral equation formulation is a precise method for solving the scattering problem. However, it is too numerically extensive if complexities of real ocean bottoms are to be taken into account. Such a solution is often limited to the simple case of two-dimensional scattering from a rigid or free surface (e.g., [90, 91, 92, 93, 94]). Often periodicity of the surface is assumed to simplify the solution [95, 96, 44]. Attempts have been made to extend the use of this solution to three-dimensional scattering from an elastic surface [97]. However, computational time remains a limiting factor, and the practical use of the "exact" solutions is often limited to comparison and benchmarking of different approximation techniques.

Lambert's Law is rigorously applicable to surfaces with an "infinite roughness", or, in other words, for sonars having an "infinitely small" wavelength.

For such surfaces modified Lambert's Law demonstrates excellent performance. When low experiment resolution results in large roughness accumulated within the sonar footprint, and only one scattering direction is considered, an approximate description of the experiment can be achieved through Lambert's Law with just one value of the Mackenzie coefficient for a broad range of grazing angles, even when Lambert's Law is not rigorously applicable.

However, the contemporary trend in sonar design is toward higher resolution and bistatic configurations, hence lower roughness accumulated within the sonar footprint and more complex angular dependences to match. As a result, the use of other approaches is expected to broaden.

The second order Kirchhoff approximation was shown to give excellent results for steep incidence and scattering grazing angles [62, 66, 67, 68]. However, it is not applicable to small grazing angles.

Boundary operator expansion technique accounts for elastic properties of the scattering interface, hence ought to be used when elastic properties are expected to be important and roughness is small.

Two-scale theory is a combination of the Kirchhoff approximation and small perturbation technique. As such, it allows one to consider rigorously surfaces with large (yet not infinite) roughness without inherent Kirchhoff approximation failure to incorporate scattering from small scale roughness. Hence, the two-scale approach ought to be used when large roughness precludes using the small perturbation expansion. However, several major drawbacks of the two-scale theory can be noted in application to rough ocean bottom scattering.

First, it uses too simplistic boundary conditions. A heuristic two-scale model for fluid-fluid interface was presented in [83], but so far no extension has been made to the fluid-elastic interface. Second, shadowing and interreflection effects are not yet incorporated into the theory. Success of the second order Kirchhoff approximation [62, 66, 67, 68] and modified Lambert's Law [78, 79, 80, 81] stresses the importance of these effects. Finally, since a perturbation approach is used in the solution, discontinuities of the surface can not be handled correctly.

In effect, in far too many cases one is left without an adequate scattering theory. For instance, I will show later (Chapter 7) that bistatic scattering data collected during the ARSRP experiment are not described in all detail by any one of the existing scattering theories.

Chapter 5

Acoustic Reverberation Special Research Program (ARSRP) Experiment

5.1 Description of the experiment

To refine knowledge about low grazing angle reverberation, an Acoustic Reverberation Special Research Program (ARSRP) experiment was conducted [98, 1, 99]. This experiment took place in the Atlantic ocean, first in 1991 (ARSRP-91), and later in 1993 (ARSRP-93). In the following, data acquired only during ARSRP-93 are analyzed.

During ARSRP-93 three ships were operating in the Midatlantic Ridge area, also known as the Atlantic Natural Laboratory. Geographically the area of operations was centered at about 26^0 North latitude and 47^0 West longitude. Research Vessel (R/V) Knorr deployed deep moored arrays and performed several near-bottom scattering, coring and dredging measurements. R/V Cory Chouest and R/V Alliance performed monostatic scattering experiments and, operating simultaneously, performed bistatic scattering experiments. The scattering data were acquired with different temporal resolution, using frequencies ranging from 200 to 1000 Hz. The basic two-ship experiment using the Cory Chouest source is shown in Fig. 5.1. The acoustic signal radiated from the source can be received and recorded by both Cory Chouest and Alliance receivers, thus making possible both monostatic (backscattering) and bistatic measurements.

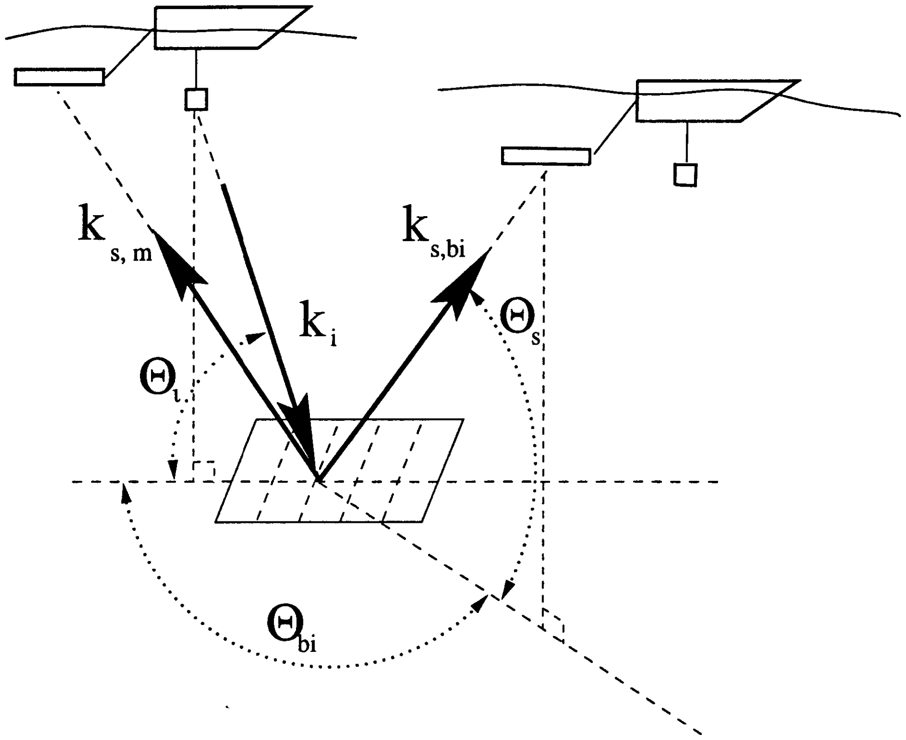
ARSRP experiment

Figure 5.1: Basic bistatic scattering experiment using two ships. Either ship can receive and transmit signals, but only one is shown. The actual size and shape of the ensonified patch on the bottom depends on the bistatic geometry, local bathymetry and source and receiver beampatterns. The incident wave vector $\vec{k}_i$, scattered wave vectors into two receiver direction $\vec{k}_{s,mono}$ and $\vec{k}_{s,bi}$, and incidence grazing angle Θ_i are shown.

5.2 ARSRP signals and systems

5.2.1 ARSRP-93 source

Each of Cory Chouest and Alliance carried an acoustic source. I used only Cory Chouest transmissions, hence I will limit myself to the Cory Chouest source description. For the same reason, the Cory Chouest source will be referred to as the ARSRP-93 source.

The Cory Chouest source was a vertical line array (VLA) of ten piezo-electric flextensional projectors. It was towed in an almost vertical string with 2.29 m separation between element centers. The depth of the array center was 181 m during the entire duration of the experiment. Uniform spatial array element weighting was used. The resultant source level at 240 Hz was 232 $dB\, re\, 1\, \mu Pa \,\&\, 1\, m$. The frequency band covered by the VLA was 200 to 280 Hz. The maximum source level in the band was observed at 200 Hz with no more then 3 dB down at any other point within the band. Array steering was possible in the angular range $0^0 - 45^0$ down from horizontal. However, all data processed in this thesis were collected with no source steering (horizontal beam).

5.2.2 ARSRP-93 wavetrains (pings)

During the ARSRP-93 experiment five different acoustic wavetrains, also called entries or pings, were transmitted by the Cory Chouest [1]. Since I am primarily interested in experiments with the highest possible spatial resolution, I concentrated on the frequency modulated signal designated as $WT93RP019$ transmitted by the Cory Chouest. This waveform is a linearly frequency modulated (LFM) slide up from 200 to 250 Hz, 5 s in duration. Its expected temporal resolution δt is given by [98, 100]

$$\delta t = \frac{1}{\sqrt{PT/S_n}} \cdot \frac{1}{W_{rms}} \tag{5.1}$$

where P is the transmitted power, T is the duration of pulse, S_n is the noise level at the carrier frequency, and W_{rms} is the rms bandwidth of the signal.

Alliance wavetrains are listed in [99]. Most of the Alliance pings are outside of the Cory Chouest Middle Frequency Array (MFA) receiving band, and none of them was used in this study.

5.2.3 ARSRP transmissions schedule

During the experiment both ships performed transmissions according to the ARSRP Pinging Schedule, which was rigidly kept. Five wavetrains were transmitted by the Cory Chouest, and six somewhat different wavetrains were transmitted by the Alliance. Pings were transmitted during a 12 *min* interval named "segment". Each three segment groups in turn was organized into 36 *min* "tables". The waveforms from the Cory Chouest did not change during its transmission times, however, those from Alliance cycled through five tables [1]. Five tables were organized into a "segment". The repetition of alternating tables was synchronized to start at every third hour, i.e., at 00:00, 03:00, 06:00, etc. A summary of the transmission scheduling terminology is given in Table 5.1 (compiled from [1]).

Each individual segment recorded during ARSRP-93 had its own number assigned ranging from 0001 to 1090. During each segment only one ship transmitted its series of waveforms (pings). Each wavetrain was repeated only once during the segment. Only scattering data due to Cory Chouest LFM pings $WT93RP019$ are processed for this study, so I will be interested in this particular waveform. This waveform was always transmitted first in the segment, with its beginning coinciding with the segment beginning. It is also convenient to start the time axis at the moment when the transmission began. Therefore, I will refer to the data starting at the beginning of the segment N either as "segment N" or as "ping N". However, depending

Label	Duration	Description
Ping	<10 *s*	The individual signals (LFM, CW, depth ping). Five different waveforms were used.
Segment	12 *min*	A series of five wavetrains transmitted over a twelve minute interval. This was the fundamental period for synchronizing with Alliance and DTAGS.
Table	36 *min*	Three segments. If both Cory Chouest and Alliance were operating, the Cory Chouest transmitted for the first two segments and then the Alliance. If just the Cory Chouest was operating, it transmitted during all three segments.
Sequence	3 hours	Five tables. The Alliance changed wavetrains during each with a periodicity of five. The sequences were synchronized to start every three hours of Zulu time, i.e., at 00:00, 03:00, 06:00, etc.

Table 5.1: Transmission schedules terminology.

on the goal pursued and the scattering geometry, I will use different data lengths.

5.2.4 ARSRP-93 data acquisition and storage

On the receiving side, both ships carried horizontal line arrays (HLA) of approximately 50 wavelength aperture. Depending on the steering direction, typical angular resolution for both HLAs employed in the experiment ranged from about 15^0 for endfire beams to about 1.5^0 at broadside. The Cory Chouest beamformer always generated 128 overlapping beams. The Alliance beamformer generated either 128 or 64 beams, however, all Alliance data processed so far have 128 beams. Thus, in all processed Alliance data, the beams are also overlapping. Typical overlap for both Cory Chouest and Alliance beams is about 30 %.

The Cory Chouest data

Two horizontal line arrays were towed by R/V Cory Chouest. LFM chirps were received by the Middle Frequency Array (MFA) consisting of 128 hydrophone groups separated by 2.5 m with four hydrophones in each (Fig. 5.2).

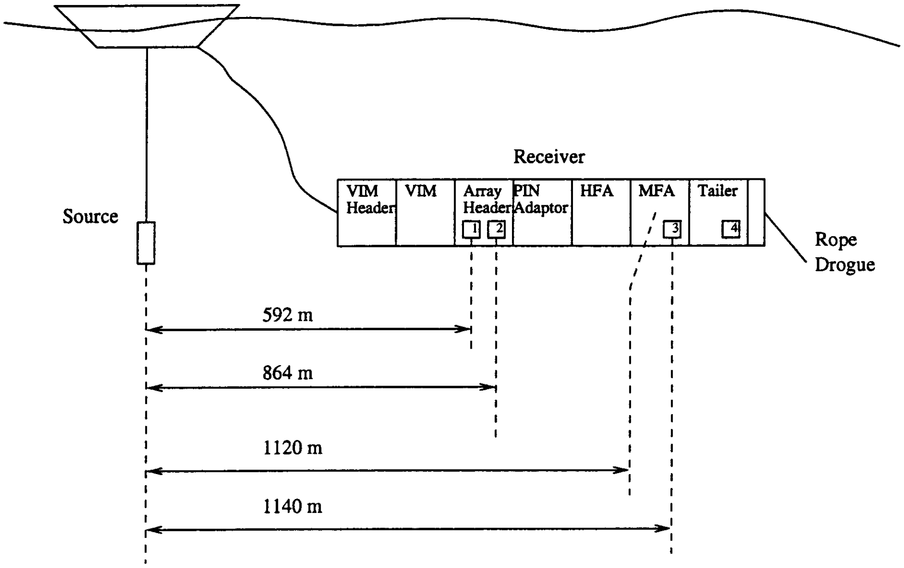

Figure 5.2: Some details of the Cory Chouest towed array design. VIM is the vibration isolation module. Eleven VIMs were used in front of the array and 5 VIMs were connected after the tailer. A rope drogue was attached to the end of the array to stabilize its shape. 1 and 3 are the depth sensors operational during the experiment. 2 and 4 are the forward and aft desensitized hydrophones. They had low gain so that the direct signal could be received without overloading. HFA is the high frequency array. MFA is the middle frequency array.

The array was towed at about 150 m depth. The acoustic center of the The MFA was calculated to be 1174 m behind the center of the ship. Analog signals from hydrophone groups were transmitted along individual twisted wire pairs. These reached the processing junction box, where the signals were filtered and digitized to 16 bit (14 bit + sign) at 1024 Hz sampling rate. Two forward hydrophone groups were not used during the experiment, to provide channels for a desensitized phone and a time zero (T-ZERO) signal. Consequently, digitized data from the Cory Chouest MFA were split and directed in parallel to the Metrum VLDS recorder (raw data on VLDS tapes) and to the Signal Processor of the Acoustic Receive Subsystem (ARS) [1]. The Signal Processor performed beamforming of the acoustic time series data, followed by matchfiltering. The beamformer had 128 beams and 128 Hz bandwidth (from 176 to 304 Hz), and provided full azimuthal coverage in the 200 to 280 Hz frequency band with no more then 0.01 dB ripple across the band [1]. Application of rectangular, hanning or hamming weighting across the array sensors was available. During the experiment hamming array taper with a 15 % pedestal was used. Complex envelope demodulation (downshift of the frequency band) and decimation was performed within the beamformer section of the Signal Processor. Beamformed but not matchfiltered data were recorded on the certified 8-mm tapes from high-density 8500 tape drives (Cory Chouest beam data, beam tapes).

In addition to 128 channels of data, four pass-through channels were recorded on beam tapes: forward Desensitized Phone, T-ZERO channel, forward Acoustic channel and aft Acoustic channel. Later these data, along with other information collected and recorded during the experiment, were stored on the ARSRP archive.

Complex bandshifted decimated data have approximately 60 Hz bandwidth and are sampled at 128 Hz. The center frequency for the frequency band shift was calculated to be 214 Hz.

The Alliance data

The Alliance towed array consists of three nested apertures of 128 hydrophones each [99] spaced at 0.5, 1.0 and 2.0 m, respectively, 256 hydrophones altogether. The acoustic center of array for the ARSRP experiment was located 1692 m behind the center of R/V Alliance. Prior to being transmitted to the dry end processing center on board the ship, raw data were digitized to 12 bits at a 6000 Hz sampling rate. These time series data from all 256 hydrophones were stored on the VLDS tapes. Additionally the low frequency aperture data collected in the frequency band 200 to 375 Hz were sent through a time domain beamformer. The beamformer applied hanning weighting across the array elements and generated 128 output beams covering the entire azimuthal space. Some of these beamformed data were then bandshifted to the "center frequency" 222.5 Hz, decimated to 128 Hz or 150 Hz sampling frequency, and stored on tapes (Alliance beam data, beam tapes).

The ARSRP Archive

All beam data can be found on the ARSRP archive at $ftp://arch.ucsd.edu$. Beam data are beamformed but not matchfiltered time series recorded on magnetic tape specific to the experiment format.

Monostatic data are stored on the archive in the "dsr format". Conversion to the geophysical industry data exchange format SEGY is done by the dsr2segy routine. Retrieved SEGY formatted data records consist of 132 channels (128 beams and 4 pass-through channels). The exact time when data starts and other important information is contained in the SEGY header.

Bistatic data are found on the archive in the "cbs format". Conversion to the SEGY is made by the cbs2segy routine. Retrieved SEGY formatted data may consist of either 64 or 128 beams, and can be decimated at 128 or 150 Hz. However, all data processed in this study consist of 128 beams decimated at 150 Hz.

Files stored on the Archive have file names corresponding to the day and time of the recording. A Julian calendar was used during the ARSRP experiment. Julian day 182 (beginning of the experiment) corresponds to July 1, 1993. All processed data were collected during Julian day 197, which corresponds to July 16, 1993. A complete conversion table from Julian to calendar dates can be found in [1]. Local Zulu time was used for the ARSRP clock synchronization.

5.3 Preparation of the ARSRP data

In this section I discuss in more detail issues relevant to the preparation of data. First, retrieved raw data must be matchfiltered to increase its temporal resolution. Then I ensure that all possible delays in the data recording scheme are accounted for, so that I have a correct time reference. The final issue to address is the receiver performance.

Here I will mostly concentrate on the monostatic data (Cory Chouest transmissions received by its own receiver) collected during pings 411 and 412. I believe that matchfiltering of the bistatic data follow the same pattern as monostatic, so that I will choose the same replica for both monostatic and bistatic data.

Cory Chouest and Alliance receivers are quite close in their design. For this reason I expect similar performance from the Cory Chouest and Alliance receivers, hence I will assign the same sidelobe level to the Alliance receiver as I measured for the Cory Chouest receiver.

The major difference between the monostatic and bistatic data is that often distance between source and receiver is larger for the bistatic geometry, hence higher transmission loss and lower signal-to-noise ratio may result. Following the same procedure, I will compute signal-to-noise ratio independently for a chunk of monostatically received data and a chunk of bistaticly received data.

5.3.1 The matchfiltering of the beamformed signals

Prior to use, data retrieved from the archive were matchfiltered. Several choices of a replica were possible. First is the T-ZERO signal, i.e., the recording of what was sent to the power amplifiers, and then transmitted into the water by the source array. Second is the signal recorded by a desensitized hydrophone (forward or aft acoustic hydrophones) during the direct arrival, i.e., what was injected into the water column close to the source. The desensitized hydrophones and their channels had different gains and somewhat different positions within the receiving array, hence one would expect to see like signals recorded by these hydrophones, except for the absolute level and exact time of arrival. This replica choice was not available for the Alliance transmissions because the Alliance receiver did not provide individual hydrophones close enough to its source to see the direct arrival, and neither did it provide for the T-ZERO signal recording. The third choice was to generate a replica according to what must have been transmitted electrically to the source system. Since this is somehow imposed instead of being measured, I designate it as a "computer generated" replica.

At first glance, using the desensitized hydrophone channels when available seems the best choice, however I tried all choices. A brief comparison of matchfiltering results with the different replicas follows.

Consider the monostatic experiment with geometry sketched in Figures 5.1 and 5.2, in which Cory Chouest transmissions were received by its own

MFA. Clearly, for a typical depth ranging between 4 to 5 *km* and typical sound speed of about 1500 m/s, the direct arrival is expected to be separated from the first bottom return by more then the LFM chirp duration of 5 *s*. Additionally, the path difference between direct and surface reflected arrivals results in the about 30 *ms* separation between them, which is larger then the spatial resolution of the LFM signal (high signal-to-nose ratio implied). Therefore, after convolving the signal received in the forward endfire beam with the desensitized hydrophone output, one would expect to see two resolved arrivals separated by 30 *ms*, or three points in the decimated data. However, this was not the case (Figure 5.3).

First, only one arrival is seen (I explain this later in the section on timing of the received signal).

Additionally, when the desensitized hydrophone signal was used as a replica generator (red line in the figure), high sidelobes with relative amplitudes up to -20 *dB* were found approximately 300 *ms* ahead of the direct arrival. This effect was not observed using the T-ZERO signal (blue line in the figure). However, higher overall sidelobe levels are seen, especially at further distances from the direct arrival (1 to 2 and 4 to 5 *s* in the figure). I finally concluded that matchfiltering with the computer generated replica,

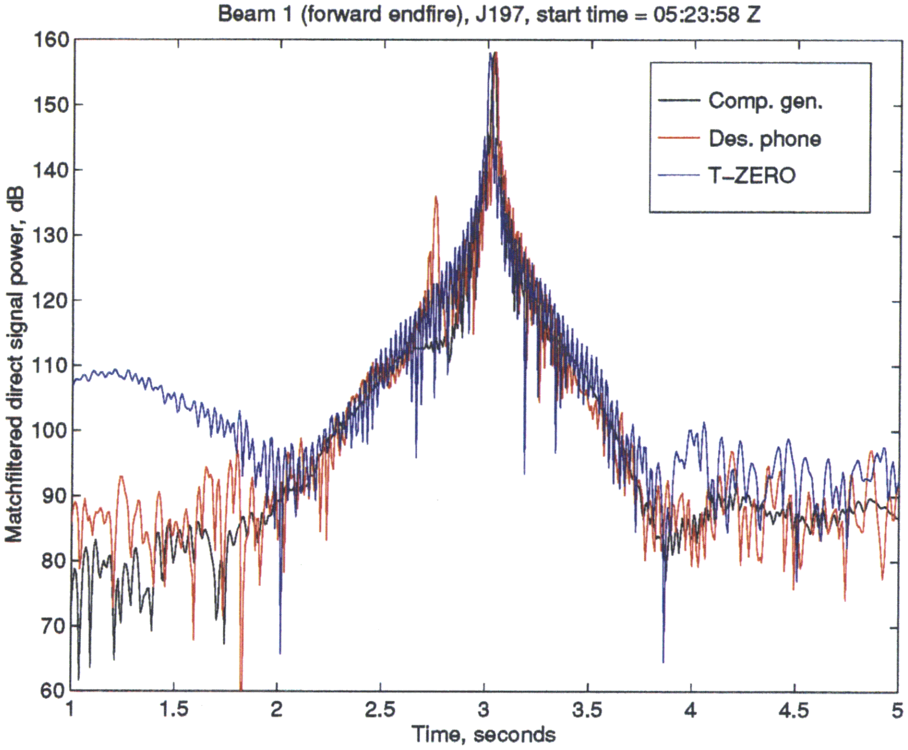

Figure 5.3: Signal received by the forward endfire beam of the Cory Chouest receiver matchfiltered with different replicas. The recording was made on J197 at 05:23:58 Z. Matchfiltering results with the computer generated replica, desensitized hydrophone and T-ZERO channel are plotted with the black, red and blue lines, respectively.

plotted as a black line in Figure 5.3, gives the lowest temporal sidelobes. Therefore, the computer generated replica was chosen for matchfiltering in both the monostatic and bistatic experiments.

Still sidelobe contamination is noticeably high with the first sidelobe at about -13 *dB*, as seen in Figure 5.4, and it must be accounted for when interpreting data.

5.3.2 The signal-to-noise ratio (SNR)

The definition of what is noise varies somewhat depending on researcher attitude. For example, when studying reverberation one might consider it as a signal, while for the purpose of whale search reverberation clearly is an unwanted sound. I am mainly interested in scattering from the rough bottom, hence for my purposes sound scattered from the bottom is a signal. This definition sets the noise to be a summation of ambient noise and system noise.

Gaussian noise

Ambient and system noise are both a result of addition of many independent noise processes. By virtue of the central limit theorem they both can be con-

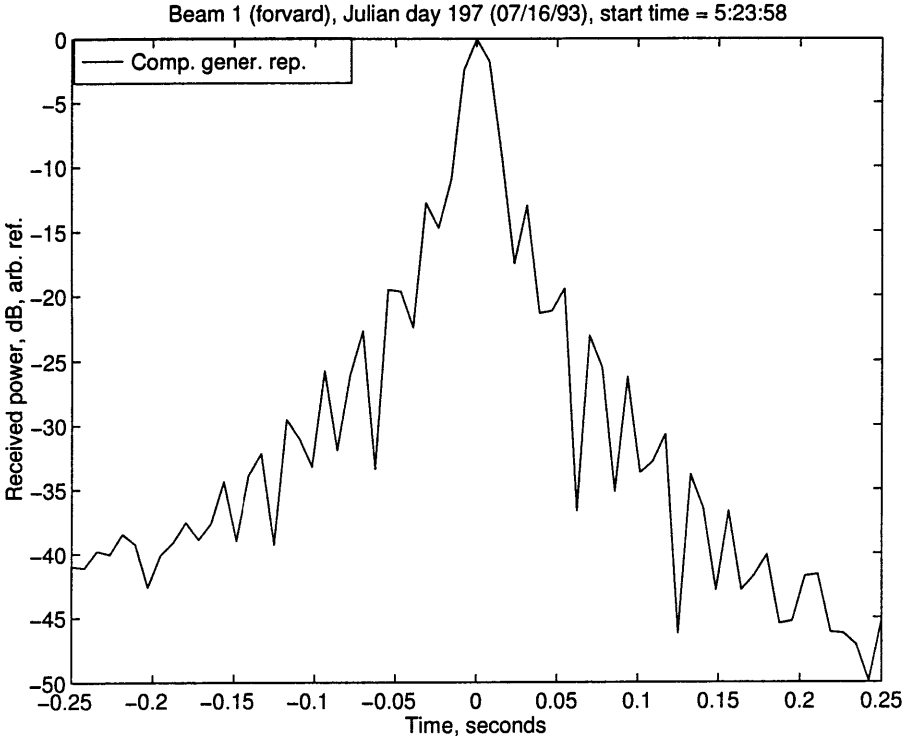

Figure 5.4: An expanded view of the direct signal received by the Cory Chouest array. The recording was made on the J197 starting at 5:23:58 Z. The received signal was matchfiltered with the computer generated replica and then normalized on its maximum value. High temporal sidelobes with up to -13 *dB* relative level are seen on the plot.

sidered stationary (on a time scale of ≥ 1 hour), and the received noise must be a Gaussian random function, possibly slowly varying in time as environmental conditions change. Then as output of the matchfilter one expects to see a stochastic process with Rayleigh probability density of its amplitude. To simplify terminology, I designate the sum of system and ambient noise as a "Gaussian noise" and I will not distinguish between these two components, treating the sum as a unified noise source of a certain level.

For assessment of the Gaussian noise level I consider data recorded by the Cory Chouest at the beginning of the segment 413, i.e., monostatic ping 413 in my terminology. This segment was recorded on the J197 starting at approximately 05:50 Z. During this segment Alliance transmitted its waveform, which started with a high frequency signal $RPL009$. Presumably, at the time of the measurement, this signal had not yet arrived at the Cory Chouest receiver. Additionally, its frequency is outside of the Cory Chouest MFA reception band. The last signal detectable by the Cory Chouest receiver was transmitted at 05:36 Z, i.e., 12 minutes prior to the beginning of the ping. I therefore assume that the reverberation due to it has decayed, and the received signal is the ambient plus system noise. In Figure 5.5 the power received in beam number 64 steered almost to broadside is plotted.

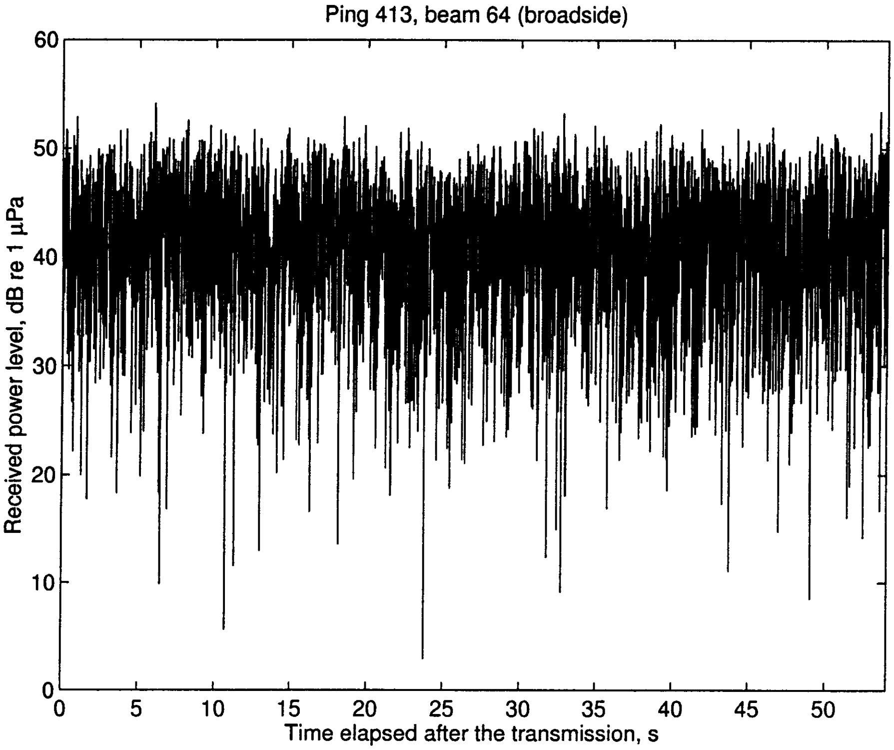

Figure 5.5: The recording of received noise level made on J197 starting at 05:48 Z. Noise level measured in the broadside beam (beam 64) of the Cory Chouest receiver is plotted.

The first thing to notice is that the signal appears stationary in time for the entire duration of the plotted data. The other thing is that the received noise level highly varies from sample to sample. The standard deviation of the noise level is 6 dB, or in linear space, the ratio of the mean received power computed for the plotted chunk of data to the standard deviation is 1.8, i.e., the standard deviation is almost the same as the mean value, as in the Rayleigh distribution. However, neither the mean value nor the standard deviation change noticeably with time.

Finally, to check validity of the Gaussian assumption I compute a histogram of received noise absolute value and compare it with the best fit Rayleigh distribution. I choose for processing 10 s of noise recorded starting 7 s after the beginning of segment 413. First I compute a histogram of the average across beams and normalize it by its maximum value. Then using the least square estimator I find the best fit Rayleigh distribution in the form $p(x) = (A/B)\exp(-x^2/B^2)$ approximating the data. Results are shown in Figure 5.6.

A good fit is seen visually. The mean square error was found to be 0.005 units. For reference, parameters of the Rayleigh distribution were found to be $A = 1.32$ and $B = 0.81$.

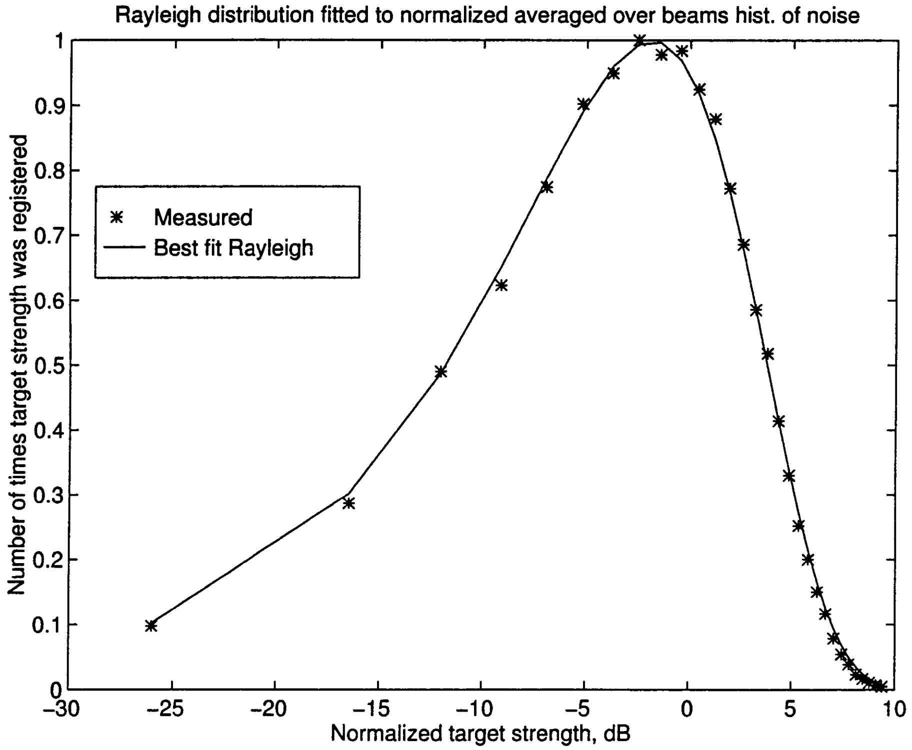

Figure 5.6: Histogram of amplitudes observed in the recording of noise (plotted with stars). Computed histogram is normalized by its maximum value. The best fit (in the mean square sense) Rayleigh distribution is plotted with a solid line.

The signal

The signal received at the beginning of segment 412 in the broadside beam 64 is plotted in Figure 5.7.

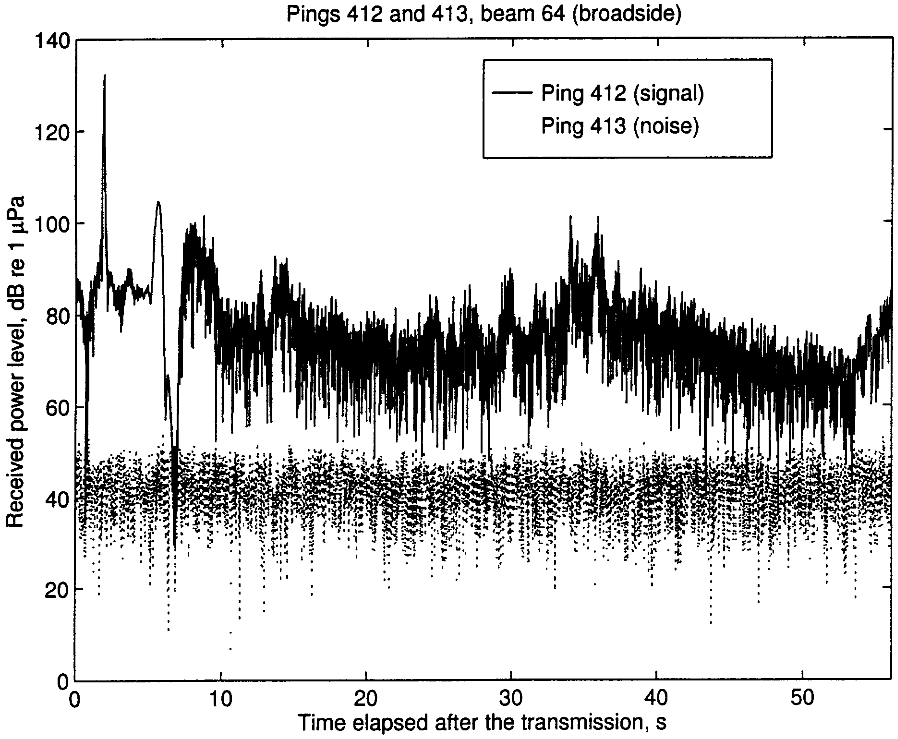

Figure 5.7: Signal measured during ping 412 in broadside (beam 64) of the Cory Chouest receiver is plotted with a solid line. The recording of the signal was made on J197 starting at 5:36 Z. The signal received in the same beam 12 *min* earlier (noise) is plotted for comparison with a dotted line.

During this segment, an LFM pulse was transmitted and subsequently received by the Cory Chouest. The dotted line on the plot represents the same "noise" recording as in Figure 5.5, however it is shifted backward in time 12 *min* to make its beginning coincide with the signal.

The levels of the data received in ping 412 differ noticeably from the Gaussian noise. Clearly, the signal observed during ping 412 is a nonstationary function, with its mean value changing noticeably with time. However, except for the mean level, it resembles in appearance the Gaussian noise, having about 6 *dB* standard deviation. To start with, I will consider qualitatively its short time average.

First, before the transmitted pulse of ping 412 arrives in beam 64 of the receiver, relatively low pressure levels are detected. However, these levels are much higher then the ambient noise observed in ping 413. Then the direct signal arrives in beam 64 and generates a high pressure peak at approximately 1 s from the beginning of the data record. Through temporal sidelobes of the matchfilter, this high level spreads and increases the observed level compared to the ambient noise, so that at time $t = 0$, when the pulse has not yet reached the array, and during time interval from $t = 1\ s$ to $t = 5\ s$ when the direct signal is already over and the bottom reflected signal has not yet arrived, the level detected is about 40 *dB* higher then the ambient noise.

Next, the maximum level of the bottom scattered signal is observed when the acoustic field is injected into the water through the source sidelobes, scattered from the bottom at almost the normal angle, and arrives at the receiver. A gradual decrease in the received level due to the increase of transmission losses, and the decrease in the incidence and scattering grazing angle follows during 7 to 25 *s*. Estimation of the absolute value of the scattering cross section of the bottom is quite complicated because the incident field amplitude is entirely determined by source sidelobes, which are hard to measure or to estimate robustly. However, relative measurements are possible, and certain second order statistics can be inferred.

A noticeable increase of the received signal can be seen at 25 to 40 *s*, when sound in the main lobe of the source reaches the bottom. The best estimate of the incident field amplitude, and consequently the most reliable measurement of the scattering cross section, can be made within this part of the data.

The signal-to-noise ratio against the Gaussian noise

Based on the foregoing, it appears reasonable to compute the "signal-to-noise" ratio (SNR). Since noise is a stationary function of time, its average value can be computed in each beam. Unlike the Gaussian noise, the mean value of the signal is not stationary, hence SNR is also a function of time. Averaging signal over too long time is meaningless, since it is clear that there is no signal at all after a long time after the transmission. To capture dynamics of the SNR as a function of time, one must use the local short time average of the received signal over a time short compared to the characteristic time of the signal nonstationarity, which is estimated to be about 10 s. On the other hand, the signal is a highly variable function of time, and not averaging at all would end up "hunting" individual target strengths of the scattering events, which is not yet my goal. I chose to average over a 1 s time interval, which is small enough to capture the SNR dynamics and large enough to make things "smooth". The resultant SNR shows the ratio of the entire reverberation signal to the Gaussian noise. It is plotted in Figure 5.8 as a function of the beam number and time elapsed after the pulse transmission. It is seen in the figure that the reverberation signal noticeably exceeds the ambient noise level, with the exception of the forward

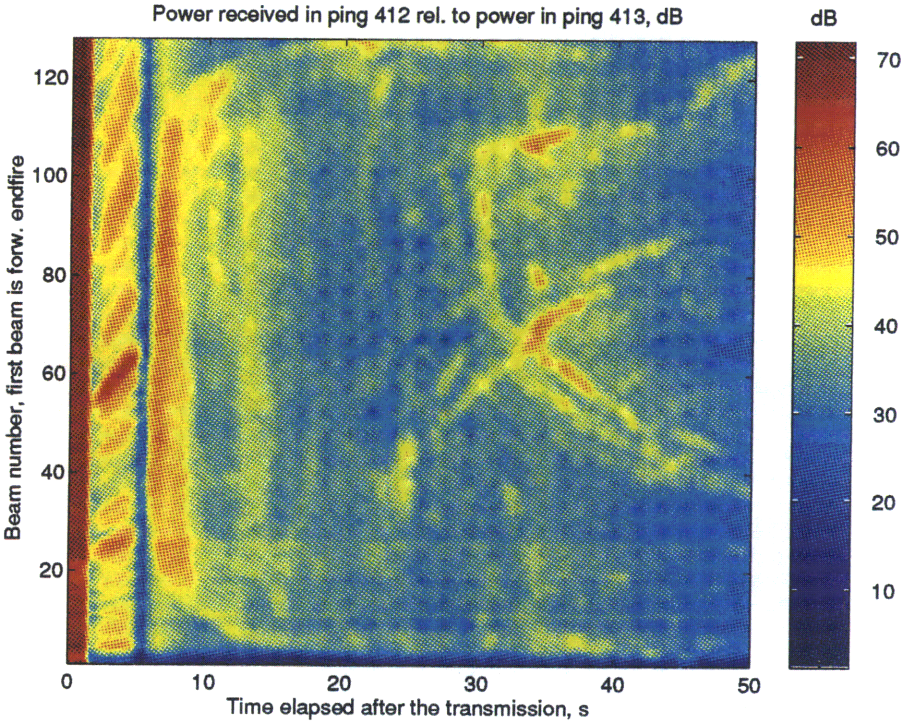

Figure 5.8: The SNR ratio against the Gaussian noise observed during ping 412. The recording of the scattering signal was made on J197 starting at 05:24 Z. Noise was recorded during ping 413 on J197 starting at 05:48 Z. Y-axis on the plot is the beam number, beam 1 is steered to the forward endfire, beam 128 is steered to the aft endfire.

beam, which is relatively noisy, no doubt due to ship noise. Another way to see that the first beam differs from others is to plot the average observed noise level as a function of the beam number (Figure 5.9).

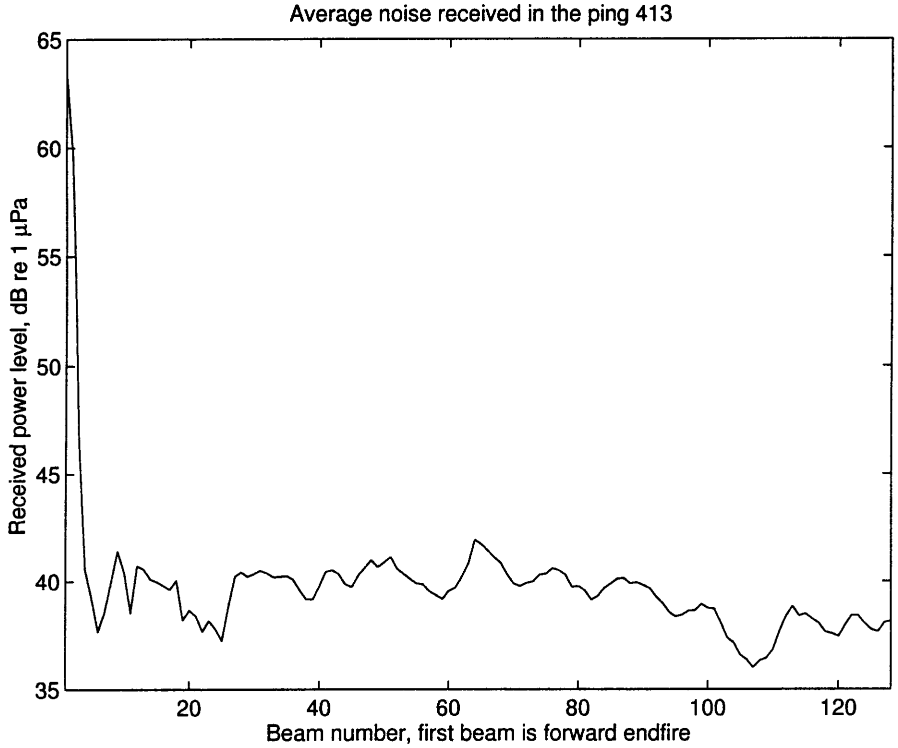

Figure 5.9: Average pressure level measured during 56 *s* observation in the ping 413 (noise). The recording was made on J197 starting at 05:23:58 Z. High noise level in the first (forward endfire) beam is seen.

The conclusion is simple: except for the forward beam, reverberation far exceeds Gaussian noise (a sum of the ambient noise, ship noise, system noise etc.). The forward beam is pointed toward the ship and receives ship noise, hence data in this beam often will be excluded from the data processing.

Following the same procedure, I compute the signal-to-noise ratio against the Gaussian noise for bistatic data. I choose bistatic ping 430 recorded by the Alliance receiver on J197 starting at 09:12 Z. Because of the large ship separation, it takes longer for the acoustic field transmitted by the Cory Chouest source to reach the receiver. Therefore I can choose data recorded at the beginning of the segment as a good estimate of the Gaussian noise. I choose 15 s of data recorded between 09:12:00 and 09:12:15 to compute the average noise level. I then choose data recorded between 09:12:20 and 09:13:16 as the signal. As for the monostatic data, I plot in Figure 5.10 the signal and noise received in the beam steered almost to the broadside direction.

Then I run a sliding 1 s average to smooth the received data and plot in Figure 5.11 the short-time averaged data level, relative to the noise level computed previously. It is seen from Figures 5.8 and 5.11 that the same conclusion can be made for both monostatic and bistatic data: reverberation noticeably exceeds the combination of ambient, ship and system noise together.

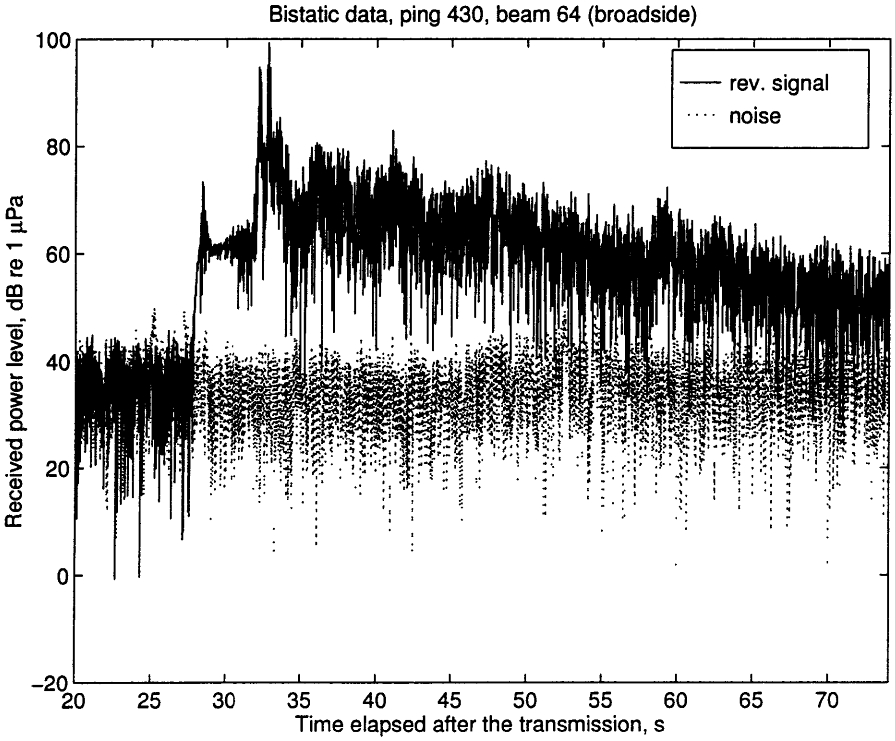

Figure 5.10: Signal measured during ping 430 in broadside beam 64 of the Alliance receiver plotted with a solid line. The recording of the signal was made on J197 starting at 09:12:20 Z. Signal received in the same beam 20 *s* earlier (noise) is plotted with a dotted line for comparison.

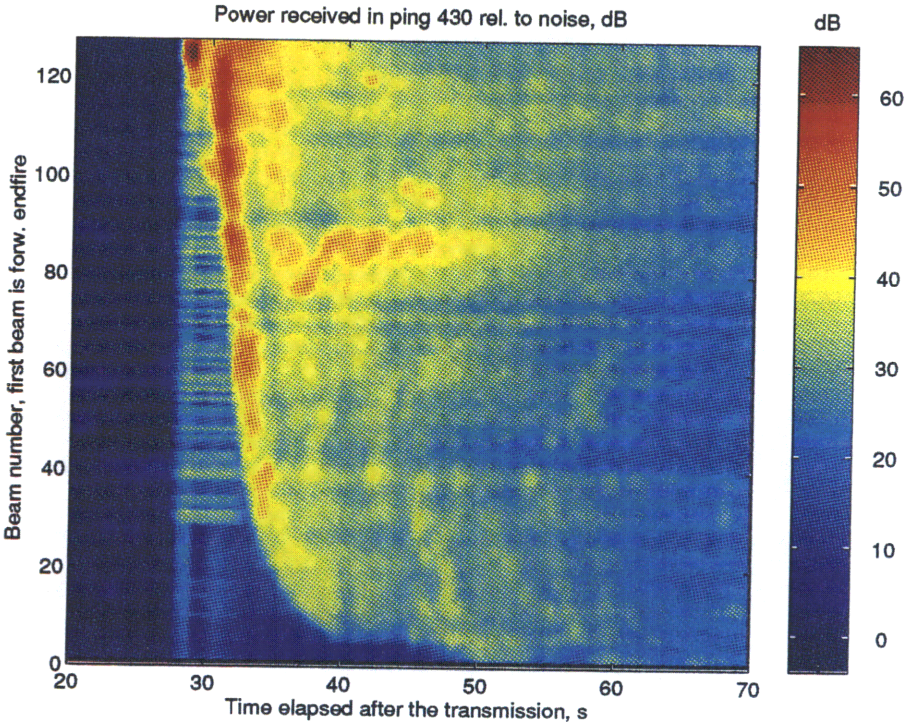

Figure 5.11: The bistatic SNR ratio against the Gaussian noise observed during ping 430. The recording of the scattering signal was made on J197 starting at 09:12 Z. Noise was recorded prior to the signal arrival. Y-axis on the plot is the beam number, beam 1 being steered to the forward endfire, beam 128 steered to the aft endfire.

5.3.3 Timing of the received signal

Given the source and receiver positions and the sound speed profile one can infer the expected time delay between beginning of the transmission and reception of the signal. For instance, I consider the monostatic geometry shown in Figures 5.1 and 5.2. Horizontal distance from the source to the desensitized hydrophone and to the center of the MFA array was 864 m and 1174 m, respectively. Source depth was 181 m, and receiver depth as measured by two depth sensors is 151 and 155 m, i.e., about the same.

Sound speed was constantly monitored during the ARSRP experiment. For the 200 m depth during the experiment, values of the sound speed were in the range from 1521 m/s to 1532 m/s [1]. The measurement of sound speed profile closest in time to the pings considered was made by the Cory Chouest on J197 at 04:40 Z, about one hour prior to the transmissions. The corresponding sound speed profile is shown in the left portion of Figure 5.12. In the right portion of the figure rays connecting source and receivers are shown. Raytracing was performed from the VLA source (horizontal range 0 m) to the desensitized phone (horizontal range 864 m) and to the center of the MFA (horizontal range 1174 m). Sound speed profile measured on J197 at 04:40 Z, source depth 181 m, and receiver depth 153 m for both

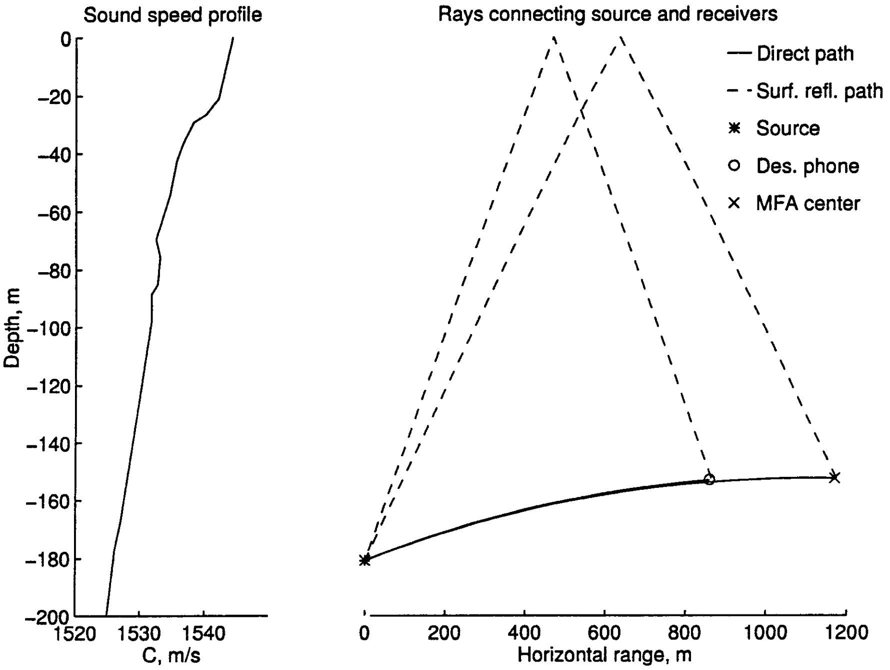

Figure 5.12: Direct and surface reflected paths connecting source (shown with a star) and center of the MFA (shown with a circle). Sound speed profile used for ray calculation is shown in the left portion of the figure.

desensitized phone and MFA were assumed.

Then from the ray tracing I expect to see arrivals at the MFA at times 770 *ms* (direct arrival) and 800 *ms* (surface reflected arrival). Corresponding transmission losses due to geometrical spreading of the acoustic field are estimated as 48 *dB* for direct and 56 *dB* for the surface reflected paths. Considering forward scattering losses at the surface for the typical sea state, the amplitude difference between direct and surface reflected arrivals becomes about 10 *dB*, i.e., close to the level of the matchfilter temporal sidelobes. This means that the dominant feature in the received signal is the direct arrival at 770 *ms*.

Arrivals at the desensitized phone are calculated at 570 *ms* and 600 *ms* for the direct and surface reflected paths, respectively. However, corresponding transmission losses are 30 and 50 *dB*, so that the surface reflected arrival will not be seen in the received signal.

Power received during the beginning of ping 411 is shown in Figure 5.13. As expected, only one distinct arrival is seen in the forward endfire beam (lower plot in the figure) and in the desensitized phone recording (upper plot). However, arrivals are observed at 850 *ms* (desensitized phone) and at 1040 *ms* (MFA). Therefore, a delay of signal arrival to the forward desensitized

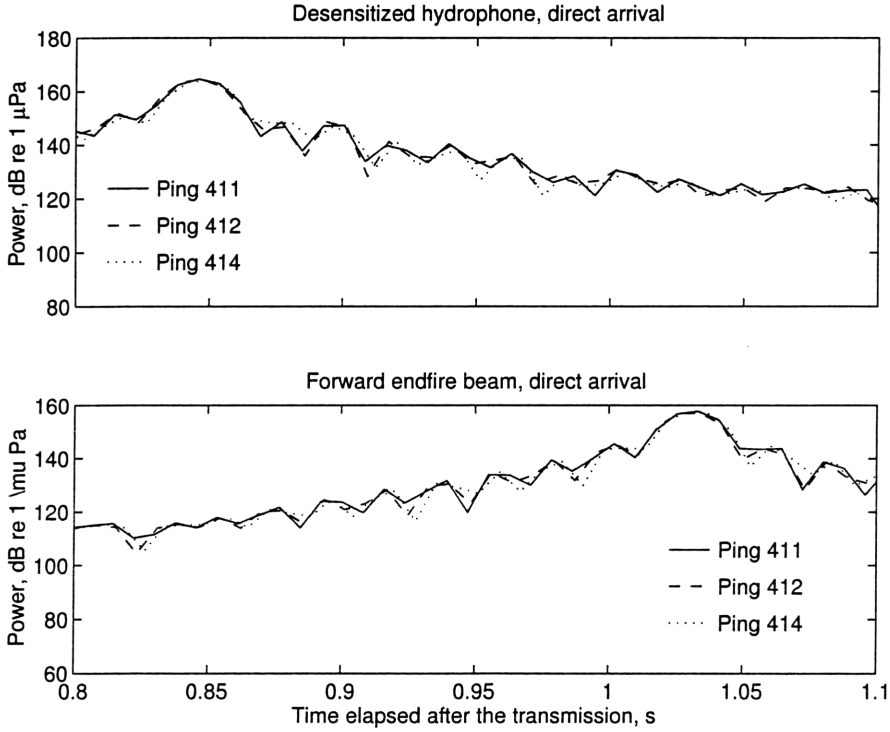

Figure 5.13: Direct arrival recorded in the forward looking beam of the Cory Chouest MFA (upper plot) and in the desensitized hydrophone (lower plot) on the J197. Solid line: ping 411, data starts at 05:24 Z. Dashed line: ping 412, data starts at 05:36 Z, shifted backward 12 *min*. Dash-dotted line: ping 414, data starts at 06:00 Z, shifted backward 36 *min*.

hydrophone and to the forward endfire beam of about 280 *ms* and 270 *ms*, respectively, is observed, which corresponds to the spatial error of about 400 *m*. To check consistency of the delay, pings 412 and 414 were also considered in Fig. 5.13. It is clearly seen in the figure that within experimental resolution the delay is consistent.

Clearly, observed delays can not be explained by the sound speed variation. Since observed delays translate into about 400 *m* spatial error, it is also unlikely that an error in time of arrival is due to the uncertainty in the distance between the source and receiver. It was assumed that the arrival delay is due to a time delay of the signal accumulated somewhere between the reception and recording, or is due to the slight mismatch between transmitted waveform and replica used for matchfiltering. Disregarding the mechanism of the delay, I will shift the monostatic data by 280 *ms* prior to analysis to account for the delay when it seems important.

5.3.4 The Cory Chouest receiver array degradation

Hydrodynamically, the array used in the ARSRP experiment is a soft slender body suspended in the water column. It is subject to two-dimensional bending under the influence of hydrodynamic forces. It is assumed straight by the beamformer, however reality clearly is not that simple. Generally, actual positions of each hydrophone at each moment of time is unknown. Distortion of the array shape results in array degradation. At first, degradation of sidelobes is expected, resulting in higher then expected sidelobe levels. Then, for large enough shape distortions the main lobe degrades, i.e., splits into several "sublobes" of comparable level (e.g., [101]).

It was also noted [1] during calibration procedures that some hydrophones in the array did not perform adequately. Several hydrophone groups had lower than expected gain, and some were dead. The presence of bad hydrophone groups in the array results in increased sidelobe levels. To understand these issues, the beam pattern was computed for a straight line array containing bad hydrophones. For steering in the broadside direction, it resulted in a uniform sidelobe level of -30 dB over the entire angular space.

From the above, sidelobes are expected to be higher than for an ideal array. One way to estimate actual array performance is to consider scattering from localized scatterers on the bottom observed by the array.

For the purpose of the array performance estimation I will consider only the strongest scattering events, since they are relatively easy to isolate. I will limit myself to the investigation of monostatic pings 411 and 412. To select only the strongest returns, I first consider data in the upper 20 dB dynamic range, clipping everything with amplitudes smaller than that.

Also, I observed that the time duration of any peak in any beam is about 30 ms, corresponding to 4 points of data at the 128 Hz decimation rate (see, for instance, Fig 5.4 for the direct signal duration, or the following figures with data). To account for it, I will average data over 4 points prior to analysis.

The splitting of the main lobe: analysis of the early arrivals

First I consider scattering at early times. Data for ping 411 and 412 are shown in the upper plots of Figures 5.14 and 5.15, respectively. The Y-axis is the beam number, where the first beam is the forward endfire beam, beams 63 and 64 are almost broadside beams, and the last beam plotted is beam number 128, which is the aft endfire beam. The temporal duration of each resolution bin in the figures is constant equal to 7.8 ms, and the angular resolution is one beam (expressed in degrees, which varies with the beam number). It is clearly seen in the figures that scattering at early times appears as a number of discrete events with somewhat different amplitudes. It is also seen that events observed in particular space resolution bins oc-

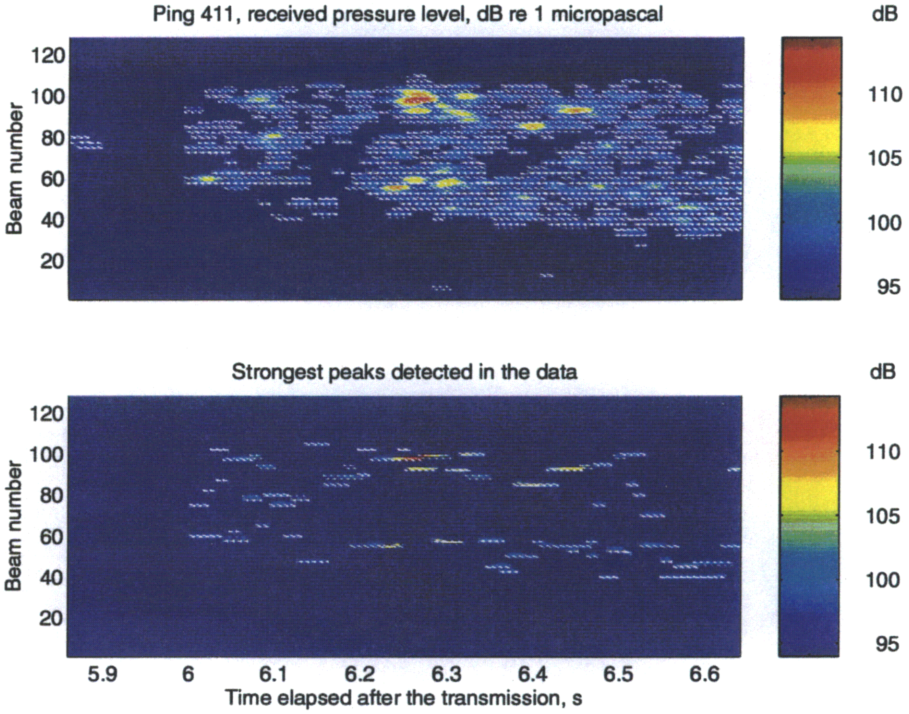

Figure 5.14: Upper plot: signal received at the Cory Chouest during ping 411. Lower plot: detected strong peaks in the received signal. Color shows received pressure level, $dB\ re\ 1\ \mu Pa$. X-axis is time. Early times, 5.9 to 6.6 s after the transmission, were considered. Y-axis is the beam number, where beam 1 is the forward endfire beam.

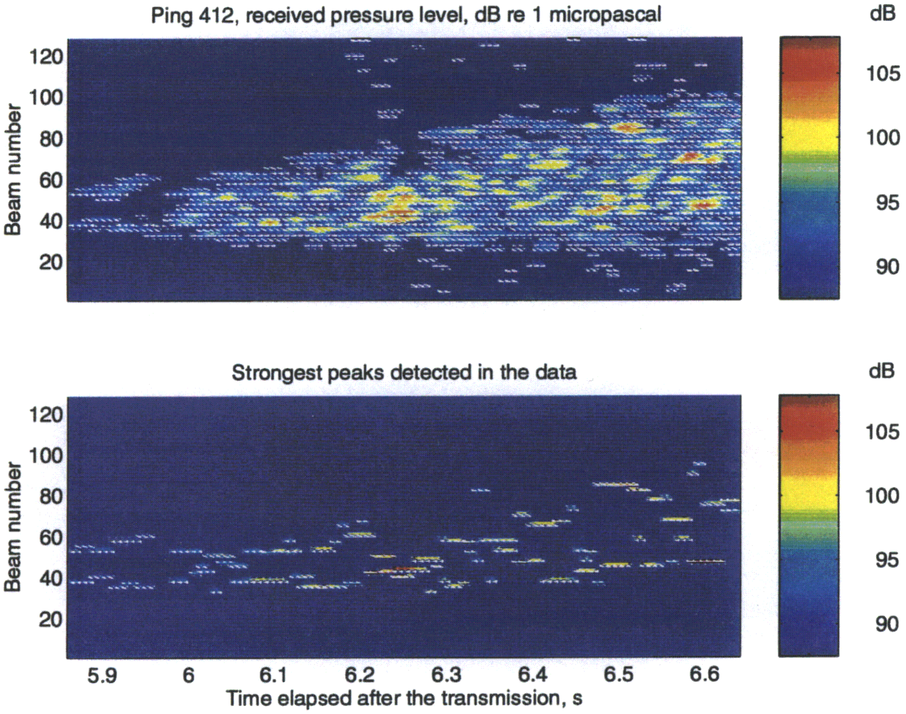

Figure 5.15: Upper plot: signal received at the Cory Chouest during ping 412. Lower plot: detected strong peaks in the received signal. Color shows received pressure level, $dB\ re\ 1\ \mu Pa$. X-axis is time. Early times, 5.9 to 6.6 s after the transmission, were considered. Y-axis is the beam number, where beam 1 is the forward endfire beam.

cupy several time-resolution bins. The discreteness and duration of observed events suggest that discrete scatterers or discrete areas with strong scattering properties are observed. If splitting of the main lobe actually occurred, I would expect to see "doubling" of the event, i.e., to observe at one particular time several events of comparable amplitudes in several beams most likely close in angular space, instead of one isolated event.

The other possible scenario for the main lobe degradation is to see broadening of the main lobe. This can happen if splitting of the lobe does take place, but not strongly enough to generate well separated individual sublobes. This would result in the "broadening" of the event, i.e., in the emerging of "wide" events occupying several adjacent beams of the receiving array.

However, neither doubling nor broadening of the received scattering events is seen in Figures 5.14 and 5.15. But generally I do see a high level of returns around strong events. Consider, for instance, beams 1 to 40 and 100 to 128 at 5.8 to 6 s. Via propagation considerations I know for sure that there must be no signal in these beams, and whatever is observed is most likely a leakage through sidelobes. However, the most important conclusion is that I do not see splitting of the main lobe.

Another way to approach this problem is to consider the statistical properties of strong events. First, I can measure the width of strong events. Because of beam overlap, I expect individual events to be seen in two adjacent beams, but not in three, unless main lobe broadening is observed. Then I can compute distances between separate events observed simultaneously in several beams.

To avoid accidental inclusion of Gaussian noise into the statistics, I will first clip data that are outside the upper 20 dB dynamic range. Next, at each sampled point in time I make a "cut" through all beams. In each cut I select the two strongest maxima. Then for each detected "strong" event I compute its 3-dB width using linear interpolation if necessary, and the separation between two peaks in the cut. Strong peaks detected in pings 411 and 412 are shown in Figures 5.14 and 5.15, lower plots. On these plots unit value is assigned to time-space resolution bins where the strong peak was detected, and a zero value is plotted if there was no detection.

Raw data for the angular width of individual strong peaks are shown in Figure 5.16. Zero values on the plot correspond to time resolution bins where less then two peaks in the cut were detected. The average spatial width at the 3 dB down level of all detected strong peaks shown in the figure was computed to be 2.4 beams, with a standard deviation 0.6 beams, where only

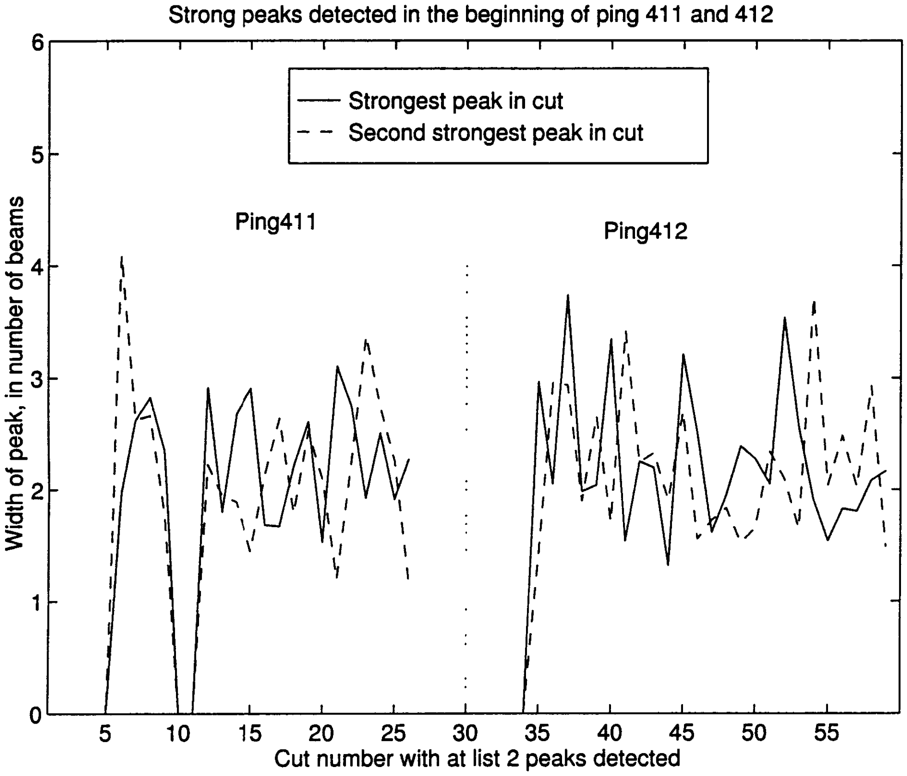

Figure 5.16: Angular width of individual peaks measured at the beginning of pings 411 and 412. Only strong peaks were considered. Zero values on the plot correspond to the case in which no strong peaks were detected in the time bin. Only the two strongest peaks in each cut were considered, if more then two peaks were detected. Width is in number of beams in which peaks can be seen at the -3 *dB* level. Linear interpolation of width was used when necessary, allowing for noninteger values of width.

cuts with at least two peaks were considered. It corresponds well to my expectation of seeing any event in two beams simultaneously.

Separations between the two strongest peaks in the cut, for each cut, as a function of cut number, are plotted in Figure 5.17. In the plot, negative separation means that the strongest peak is detected in the beam with a

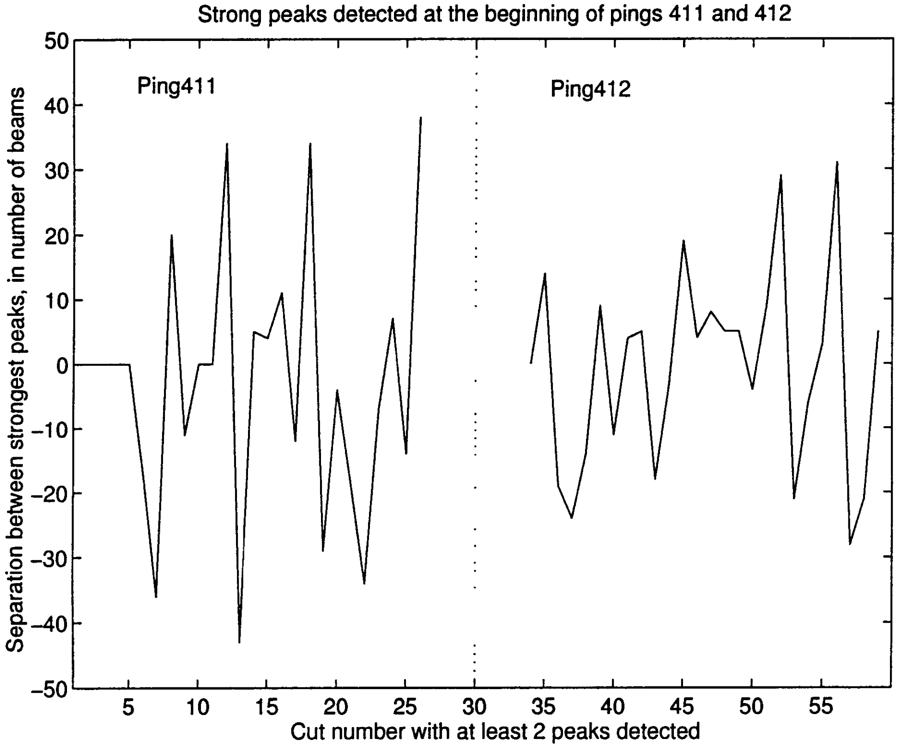

Figure 5.17: Separation (in number of beams) measured between the two strongest peaks found in the time bin. Zero values are plotted for cases in which less then two strong peaks were detected.

lower number then the second strongest peak. It appears that separations are about uniformly distributed in the -30 to +30 range. Again, zero values correspond to time resolution bins with less then two strong peaks detected.

To estimate the characteristic time scale of separation between the two strongest peaks in a cut as it changes with time, I computed the autocorrelation function (see Figure 5.18). It is seen in the figure that the correlation function has a narrow maximum at zero.

An expanded view of the autocorrelation function near zero correlation lag is shown in Figure 5.19. It is seen that at one lag time shift, the correlation function value drops from 1.0 to 0.2. This shift corresponds to cross-correlating of separations seen in a certain time bin with those seen in the next time bin, hence there is little correlation between separation observed in one time bin and the one observed in the next.

The splitting of the main lobe: analysis of the main lobe arrivals

An increase in the level of the received signal is seen in Figure 5.7 during the time interval from 25 to 40 s after the beginning of the transmission. This increase is due to the fact that the incident acoustic field during this time is within the main lobe of the source. In this time interval the most reliable

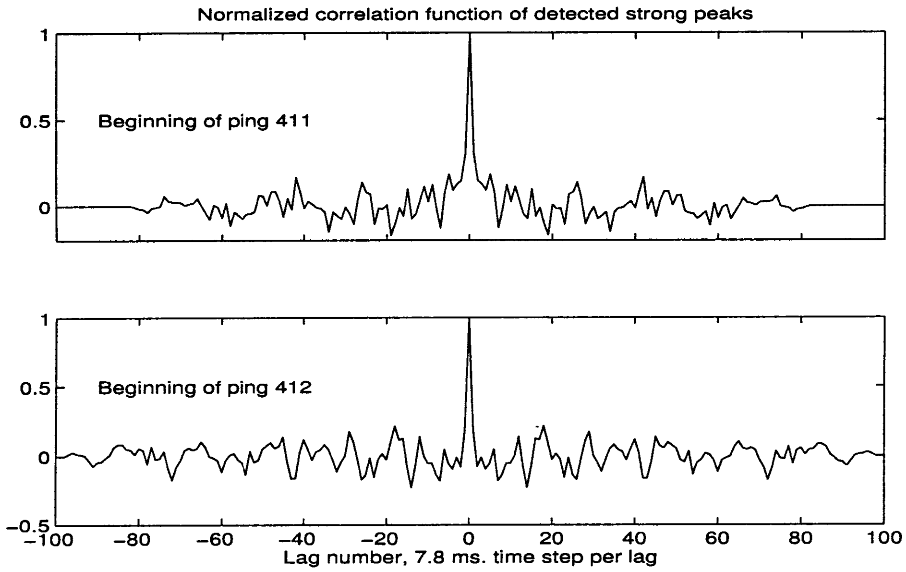

Figure 5.18: Autocorrelation function of separations between two strongest peaks detected at the time bin of data collected in the beginning of ping 411 (upper plot) and 412 (lower plot). Arrivals seen in the data 7 to 17 *s* after the transmission are considered (early arrivals).

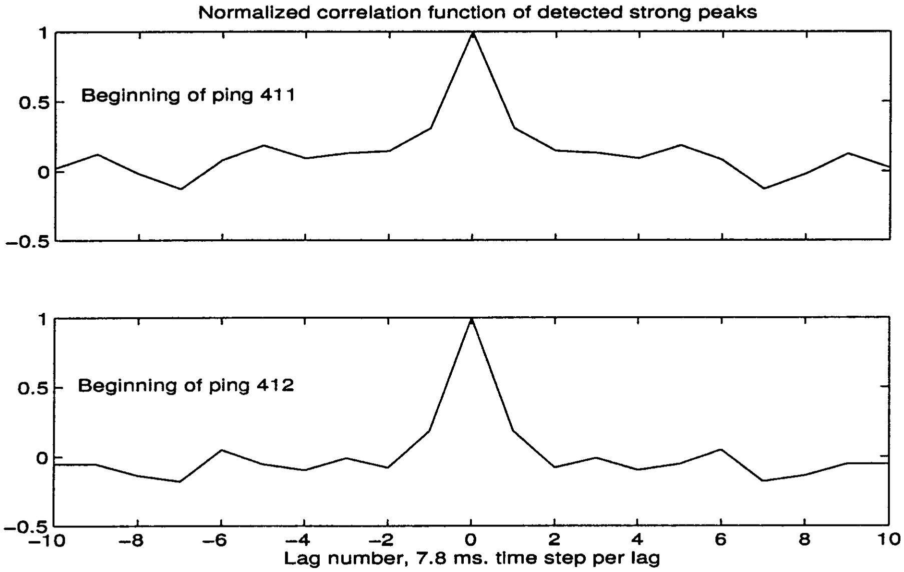

Figure 5.19: An expanded view of the autocorrelation function of separations for early arrivals seen in ping 411 (upper plot) and 412 (lower plot)

estimate of the incident field amplitude can be made, hence a good estimate of the scattering cross section can be achieved. Therefore, this part of the data will be useful in subsequent discussion. I will repeat the procedure outlined above, and investigate if the splitting or broadening of the main lobe occurs in data recorded in this time interval. Monostatic pings 411 and 412 will be considered again.

I first select a small data interval of 780 *ms* in length, starting at 31.25 *s* after the beginning of the transmission (Figures 5.20 and 5.21). It is seen in the figures that scattering again is discrete, i.e., I see isolated peaks. The same statistical procedure used for the early arrivals now gives, for the ping 411 data, a mean width for strong peaks of 2.1 beams, with a standard deviation of 0.4 beams. Corresponding numbers in the ping 412 data are: width of 2.0 beams, with a standard deviation 0.5 beams.

As for separation, I again compute the autocorrelation function (Figure 5.22). To make the width of the autocorrelation function more visible, an expanded view is shown in Figure 5.23. Again, no correlation between separation is seen in adjacent time bins.

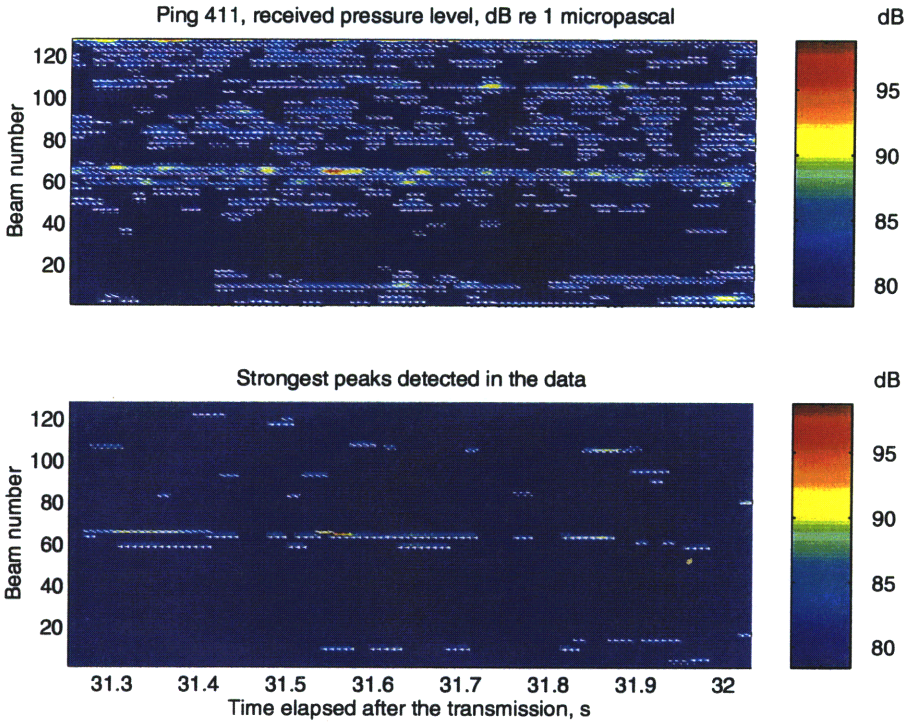

Figure 5.20: Upper plot: signal received at the Cory Chouest during ping 411. Lower plot: detected strong peaks in the received signal. Color shows received pressure level, $dB\ re\ 1\ \mu Pa$. X-axis is time. Times from 31.3 to 32 s after the transmission were considered. Y-axis is the beam number, where beam 1 is the forward endfire beam.

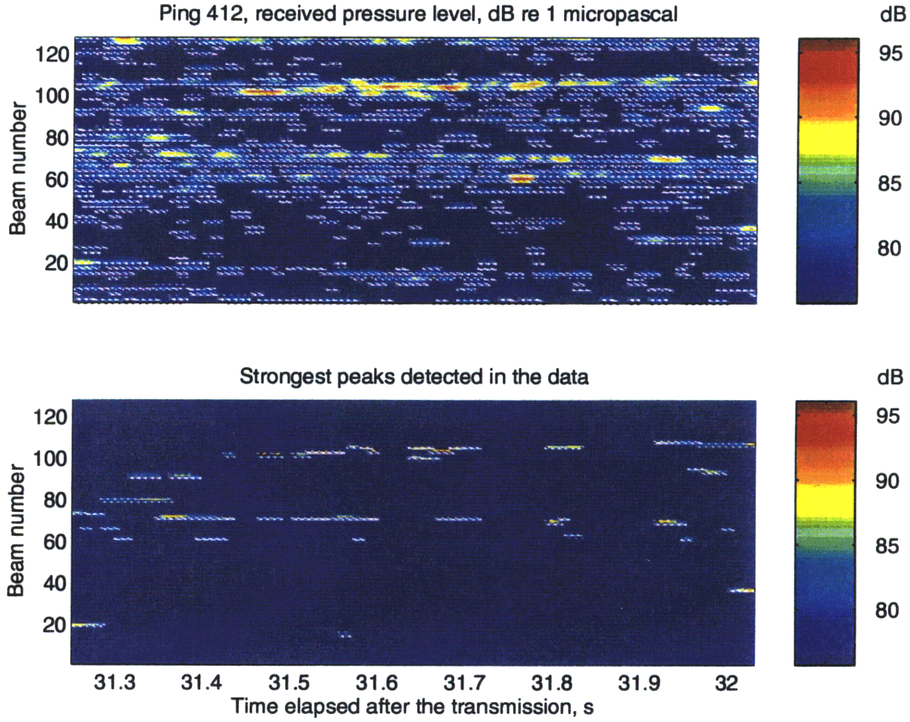

Figure 5.21: Upper plot: signal received at the Cory Chouest during ping 412. Lower plot: detected strong peaks in the received signal. Color shows received pressure level, dB re 1 μPa. X-axis is time. Times from 31.3 to 32 s after the transmission were considered. Y-axis is the beam number, where beam 1 is the forward endfire beam.

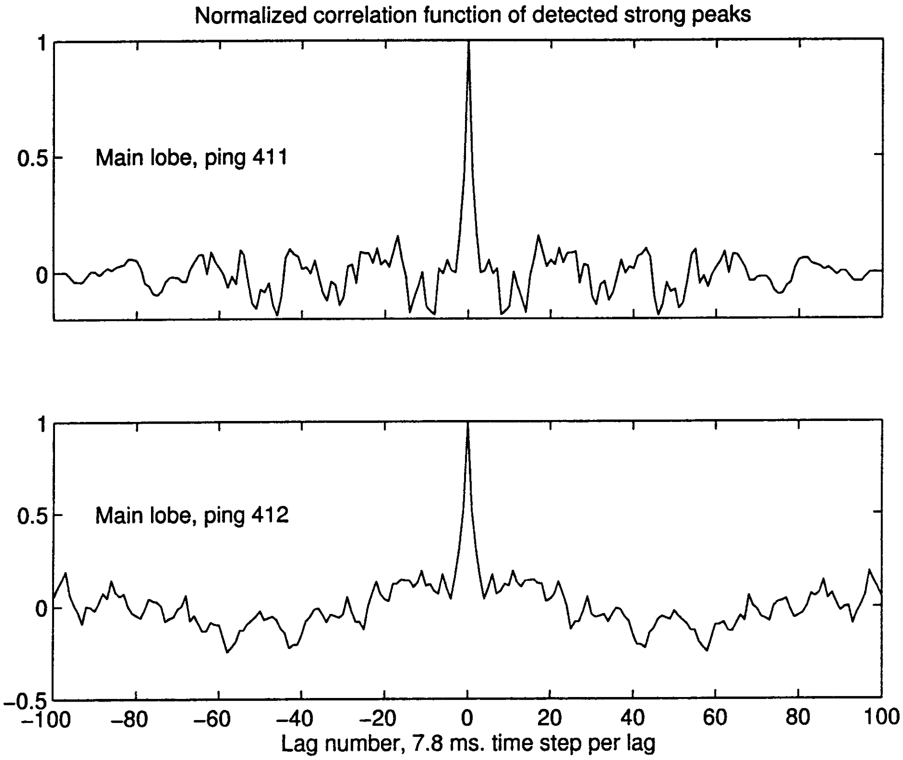

Figure 5.22: Autocorrelation function of separation between the two strongest peaks detected in the time bin of data collected at the beginning of ping 411 (upper plot) and 412 (lower plot). Arrivals seen in the data 35 to 45 *s* after the transmission are considered (main lobe arrivals).

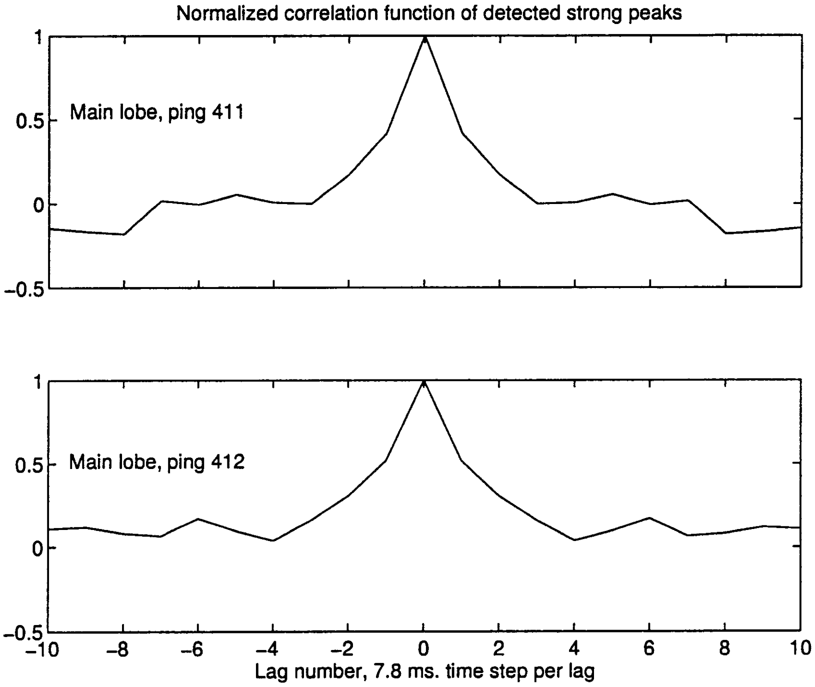

Figure 5.23: An expanded view of the autocorrelation function of separation for main lobe arrivals seen in ping 411 (upper plot) and 412 (lower plot)

Discussion

I found that an average event is seen at the -3 *dB* level in two beams only. This is consistent with the array main lobe width, and the beam overlap. For instance, consider broadside beams 63 and 64. These beams are expected to occupy the angular space from 88.83^0 to 90.26^0 and from 89.74^0 to 91.17^0, respectively. Correspondingly, an event located in the broadside direction will be detected in both beams with almost the same amplitude.

The separation between strong peaks detected at any given time in different beams was found to be about uniformly distributed in a range of ± 30 beams. I also found that the separation detected in one time bin is uncorrelated with the separation detected in an adjacent time bin.

If there was splitting of the main lobe due to the complexity of the array shape, I would expect the array beam pattern to change with the characteristic time scale of the array shape change. Therefore, I expect to see the unchanged beam pattern during a time interval shorter then the characteristic time of the array. The fact that I see no correlation between separations observed in one time bin with an adjacent time bin means that either there is no beam splitting, or that the array shape changes in a time scale smaller than the size of my time bin, which is set to 8 *ms*.

The characteristic time of the array shape can be related to its spatial translation (with the time scale $T_{c,1}$) and to the propagation of smaller disturbances along the array (with the time scale $T_{c,2}$). For a characteristic width of the array main lobe α, the corresponding interrogated length at distance R on the bottom is $L_1 = R \sin \alpha$. The corresponding translational characteristic time can be estimated as $T_{c,1} = L_1/U$, where U is the speed of towing $U \approx 2\, knots$. Using $\alpha = 1.5^0$ and $R = 5\, km$ results in a lower bound estimate of the characteristic translational time $T_{c,1} > 3\, s$. The characteristic time due to propagation of disturbances along the array can be estimated if their speed and wavelength Λ are known. However, it was shown [102] that disturbances of interest propagate along the array with the speed approximately equal to U, and $\Lambda = U \cdot T_f$, where T_f is the characteristic time scale of the forcing applied to the array [102]. Then $T_{c,2}$ is simply equal to the T_f. It is believed that ocean surface motion (swells with typical periods of about 10 s) is a primary source of the array disturbances [102]. This results in an estimate $T_{c,2} \approx 10\ s$. Therefore, the minimal time scale associated with the array motion is 3 s, which is much larger then the time bin size of 8 ms.

Hence I conclude that splitting of the array main lobe is not seen in the analyzed data.

The angular sidelobes of the receiving array

It seems difficult to generate a good estimate for the sidelobe level with my data. This difficulty is mainly due to the fact that in each beam, at each moment of time, I have a valid scattering signal. The pressure level received in the beam is a sum of the scattered signal and leakage of signals received in other beams through sidelobes of the beamformer. At no time and in no beam can I say for sure which part of the received signal in the beam is due to the scattering, and which part of the signal is sidelobe leakage, with only one exception. Because the source sidelobe ensonification of the bottom (depth is approximately 4000 m) starts about 6 s after the beginning of the transmission, let's consider again data recorded about 6 s after the transmission. Scattering is registered first from elevated areas in nearly broadside beams, since the round trip to the bottom takes longer for horizontally started rays then for vertical ones. Consider the very beginning of the record in Figure 5.15. For the ping 412 geometry, scattering is seen to appear first close to beams 40 and 50. On the lower plot I clearly see these two peaks detected in beams 38 and 54. However, on the upper plot one can notice that the recorded signal is nonzero in all beams, including for instance the aft beam which was generated by initially horizontal rays and could not possibly complete the round trip. Clearly, data in beams not close enough to those containing scattering events are generated by sidelobes of the two beams containing events. Then a cut through all beams made at an appropriate time may reveal the beam pattern of the receiver. In Figure 5.24 the signal recorded by the receiver at time $t = 5.859\,s$ after the beginning of the transmission (first data points shown in Figure 5.15) is plotted together with the summation of the idealized beam patterns of the array steered to the direction of beams 38 and 54, i.e., 65.33^0 and 80.48^0 from forward, respectively.

The idealized beam pattern was computed assuming an ideally straight line array, and a broadband signal occupying frequencies from 200 to 255 Hz. It is seen in the figure that the sidelobe level is almost constant throughout the entire angular range, and equal to about -25 dB, instead of the expected lower values.

Conclusions

It is therefore my conclusion that observation of early arrivals, and arrivals due to scattering within the source main lobe in pings 411 and 412, shows no significant broadening of the main lobe, and no noticeable splitting of the

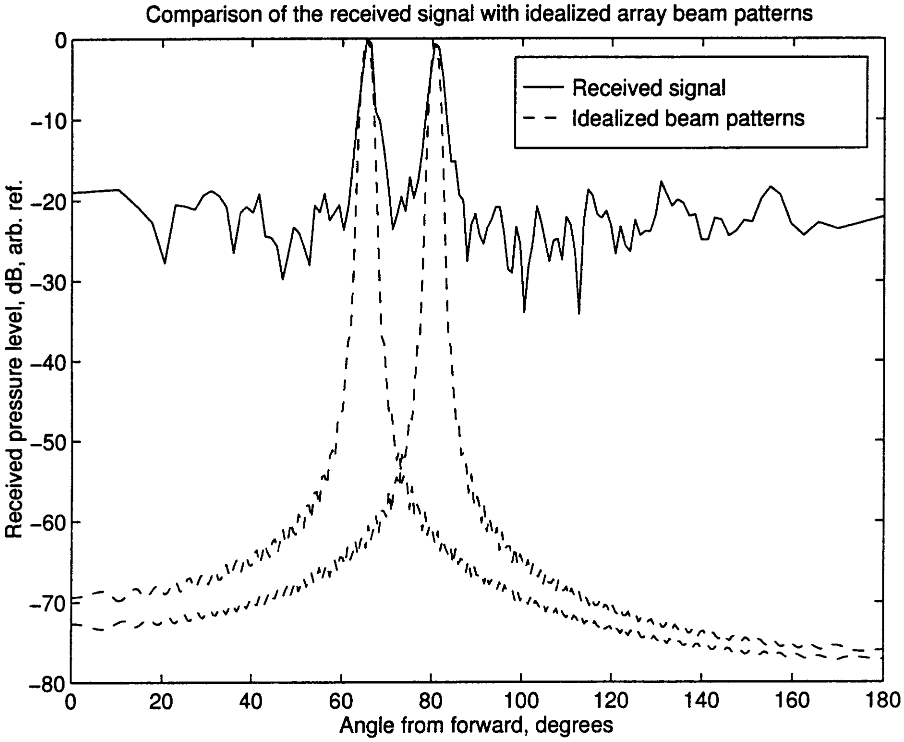

Figure 5.24: Comparison between signal recorded by the receiving array and idealized beam patterns of the receiver steered into the direction where strong events were detected. The recording was made 5.859 *s* after the beginning of the transmission. Data were collected during ping 412 on the J197, starting at 5:36 Z. High sidelobe levels compared to the idealized case are seen throughout the entire angular range.

main lobe. Since later I will analyze the statistical properties of individual peaks observed in the received signal, this conclusion is particularly important. Any strong peak observed in the received data is likely to be due to scattering from certain features within the beam, and not due to the leakage from another beam, or a split main lobe.

I do however see a relatively high sidelobe level, both in temporal and in angular space. Therefore, as far as weak features in the received signal are concerned, I can not be sure whether they are scattering data generated within the beam or leakage through high array sidelobes.

I estimate the actual angular sidelobes to occupy the entire angular space at about the -25 *dB* level for broadside steering of the array. It is 5 *dB* higher than estimated for the ideally straight array, when inadequately performing hydrophone groups were considered. Sidelobes higher than the -25 *dB* level were not found in the data analyzed.

Temporal sidelobes (Figure 5.5) are seen to decay with the increase of the separation from the event. Sidelobes are seen to drop to the -25 *dB* level at a temporal separation of about 70 *ms* from the event. However the first temporal sidelobe of the event with -13 *dB* level is seen at about 30 *ms* separation from the event.

Chapter 6

The Higher Order Statistical Properties of the ARSRP Data

6.1 Higher order statistics vs. first order statistics

It was clearly shown in Chapter 5 that the pressure level received in any of the receiver beams changes notably in time, and at least two time scales can be detected in the received signal.

The first time scale observed is associated with the frequency band of the transmitted signal, or, in other words, with the duration of the autocorrelation function of the transmitted signal (for instance, see Figure 5.4). If one considers the -3 *dB* width of the autocorrelation function, this scale would be approximately 25 *ms*. I will refer to this scale as a "transmitted pulse length scale", or simply "pulse length scale".

The other scale can be revealed by averaging data on an interval large compared to the pulse length. Running a 1 *s* sliding average of the data, I generate a "mean" received pressure level, which is seen to be a function of time (Figure 5.7 and 5.10, upper curves, Figure 6.1, upper plot). I refer to this averaged signal as the "mean signal" or "average signal". Its level is determined by both propagation effects (geometrical transmission losses suffered by the acoustic field, absorption), by source and receiver beam patterns, and by scattering properties of the patch on the bottom (where scattering is coming from).

Clearly, knowing how to predict the mean value of the observed signal for a given experiment geometry is of great importance for studying the reverberation. However, another question seems equally important: except for the mean level, which statistical measures (if any) are also relevant for understanding reverberation. For instance, it can be observed (see Figure 5.7 and 5.10, lower curves, Figure 6.1, lower plot) that removing from the

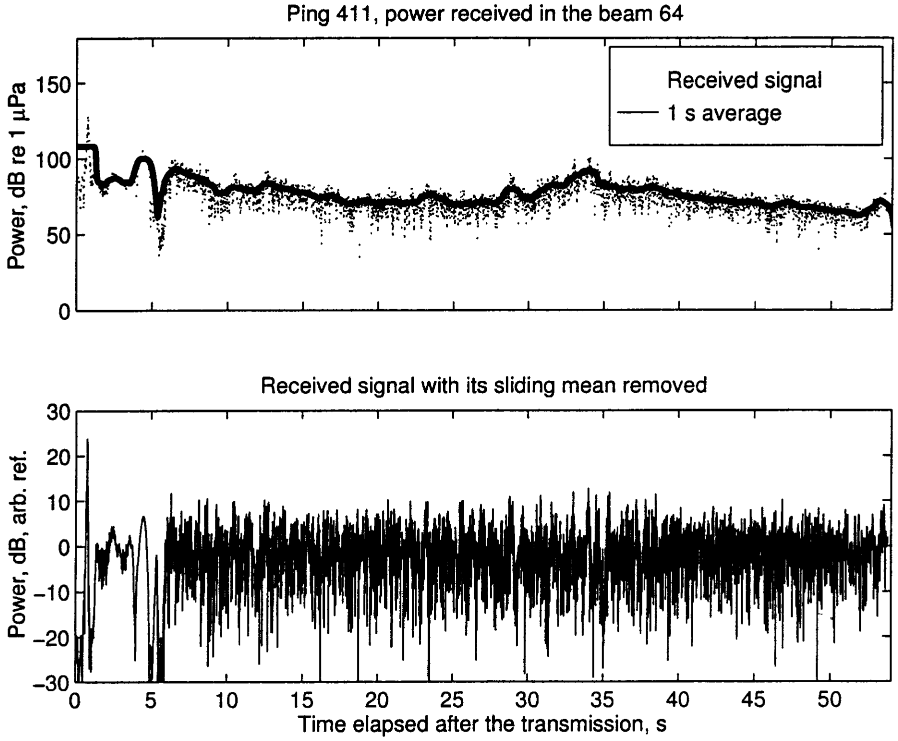

Figure 6.1: Signal received at the Cory Chouest. The recording was made on the J197 starting at 05:24 Z. The dotted line on the upper plot is the received signal. The solid line on the upper plot is the 1 *s* sliding average of the received signal (in logarithmic domain). The lower plot is the received signal with its 1 *s* sliding average subtracted.

received signal its sliding mean effectively "stationarises" the process. It could be called the equivalent of an automatic gain control (AGC). Consider in the figure the time interval from 7 to 50 s, i.e., away from the direct arrival. It appears that the AGC signal does not exhibit different behavior at the time of high reverberation (25 to 40 s in the plot) or when the reverberation signal is low (15 to 20 s in the plot), and in fact it does not differ much from recording of the noise.

I will first address this question, namely, except for the mean level, is there a difference between the recorded reverberation signal and a simple Gaussian stochastic process. This issue will be approached via accessing the statistics of the received signal normalized by its sliding mean. The "first order statistics" of the received signal, i.e., its mean value, is now excluded from consideration. Hence, I call investigation of the normalized or AGC signal (with zero mean) "the investigation of the higher order statistics". Later in a separate section we shall return to the mean value and consider the "first order statistics" of the received signal.

To measure the higher order statistics I normalize the data acquired in each receiver beam during pings 411 and 412 on their 1 s sliding mean value. It has to be understood that after normalization has been done there is no way to derive target strength from the normalized target strength, or measured noise level from the normalized noise level. In this sense normalized values have little physical meaning. Yet it is convenient to use these normalizations when higher order statistics are analyzed and the mean value is not an issue.

6.2 The higher order statistics in monostatic ARSRP data

6.2.1 Histogram of the received signal

One way to address higher order statistics is to compute histograms of amplitudes observed in the received signals. First I consider "main lobe returns", i.e., the reverberation signal received between 30 and 40 s after the beginning of the transmission, when the incident field reaches the bottom through the main lobe of the source (Figure 6.2 and 6.3 for pings 411 and 412, respectively). Then I compute histograms for the early returns recorded 7 to 17 s after the beginning of the transmission (Figures 6.4 and 6.5 for pings 411 and 412, respectively). During this time the incident field is source sidelobe dominated. Even though this makes it difficult to determine the exact amplitude of the incident field during these times, I know that the signal due to the reverberation exceeds the underlying Gaussian noise level significantly. I also know that the acoustic field is incident upon the surfaces at generally steeper grazing angles, and ensonifies a smaller patch, compared to values during main lobe returns. Last I consider the Gaussian noise, i.e., receptions during ping 413 (Figure 6.6). To be consistent, for analysis I chose 10 s of noise recorded starting 7 s after the beginning of the segment.

Several things can be noted from the comparison of Figures 6.2 - 6.6. First, it is seen that there is not much difference among histograms computed for different beams within one figure. Second, there is not much difference among figures either, i.e., the signal recorded early (steeper incidence grazing angles and smaller scattering area on the surface) has almost the same statistical properties as the signal recorded later (small incidence grazing angle, large ensonified area). It is seen that histograms for early and main lobe arrivals for both pings looks like each other and like the recording made during ping 413 (noise), i.e., they are "noise-like".

To check this statement I average over all beams and compute estimates of the probability distribution function (PDF) of the AGC signal and of the noise. Computed PDFs are plotted in Figures 6.7 and 6.8 for early and

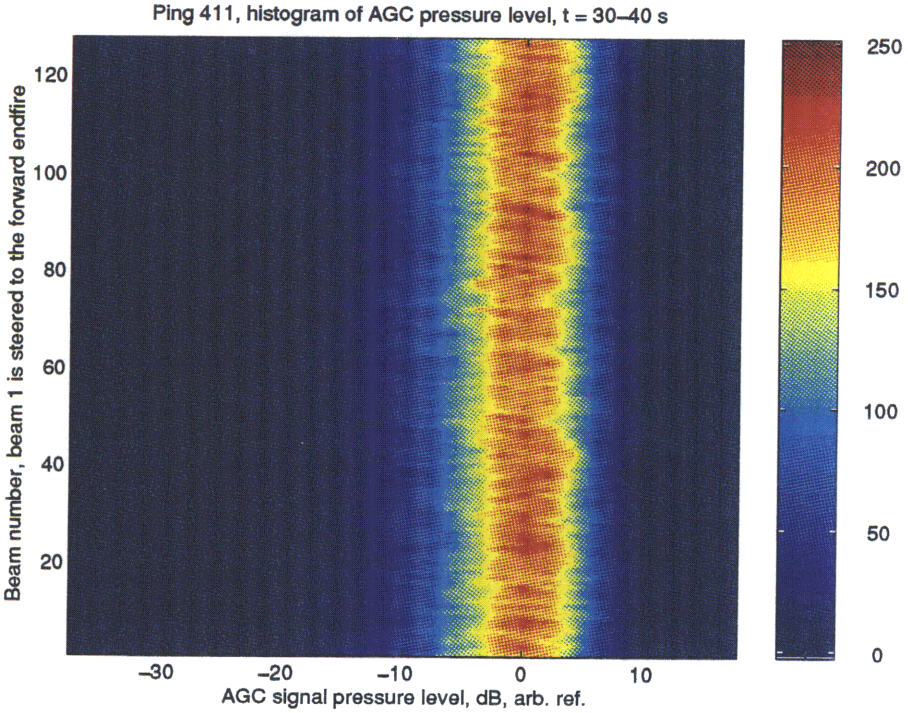

Figure 6.2: Histogram of the AGC scattering signal. 1 *s* sliding mean was removed for normalization. The recording was made during ping 411 (J197, starting at 05:24 Z), 30 to 40 *s* after the beginning of the transmission. The value of the normalized signal is plotted along the X-axis. Beam number is plotted along the Y-axis. Color shows the number of occurrences of the AGC signal value in each 2 *dB* resolution bin per 10 *s* of data considered.

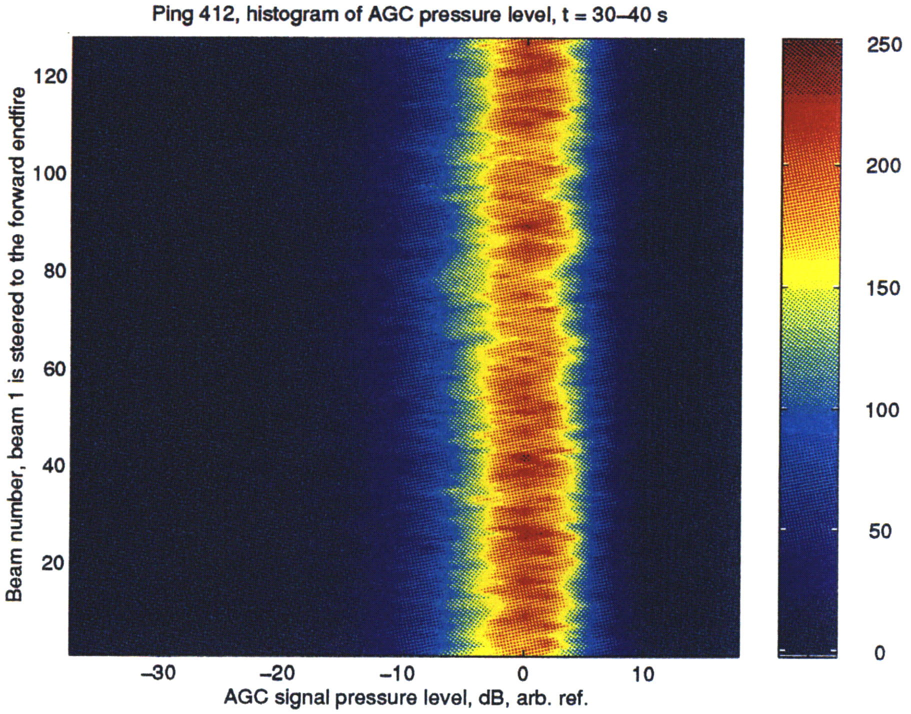

Figure 6.3: Histogram of the AGC scattering signal. 1 s sliding mean was removed for normalization. The recording was made during ping 412 (J197, starting at 05:36 Z), 30 to 40 s after the beginning of the transmission. The value of the normalized signal is plotted along the X-axis. Beam number is plotted along the Y-axis. Color shows the number of occurrences of the AGC signal value in each 2 dB resolution bin per 10 s of data considered.

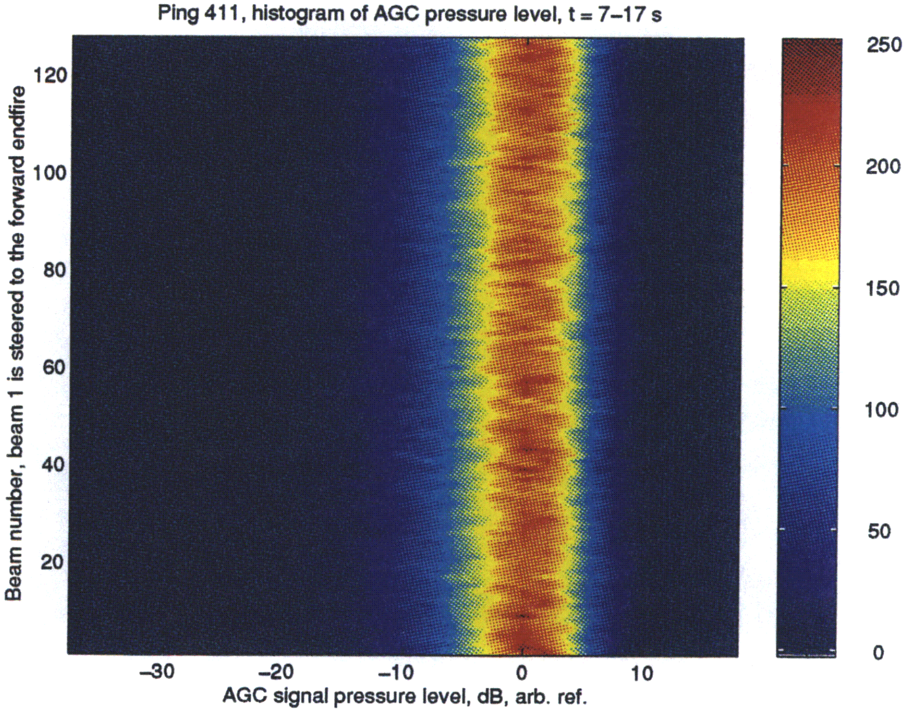

Figure 6.4: Histogram of the AGC scattering signal. 1 s sliding mean was removed for normalization. The recording was made during ping 411 (J197, starting at 05:24 Z), 7 to 17 s after the beginning of the transmission. The value of the normalized signal is plotted along the X-axis. Beam number is plotted along the Y-axis. Color shows the number of occurrences of the AGC signal value in each 2 dB resolution bin per 10 s of data considered.

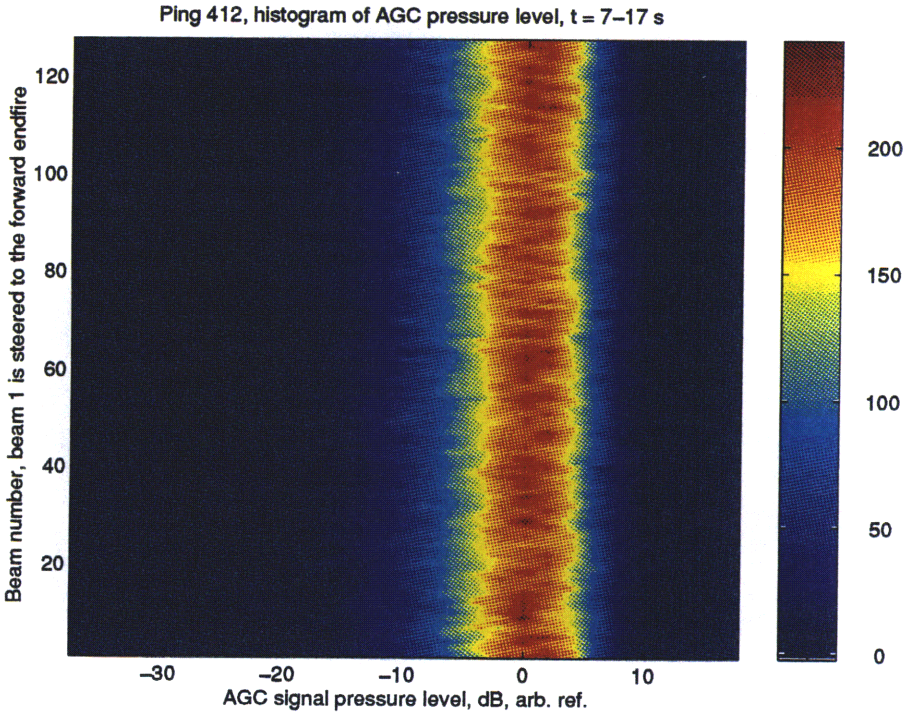

Figure 6.5: Histogram of the AGC scattering signal. 1 *s* sliding mean was removed for normalization. The recording was made during ping 412 (J197, starting at 05:36 Z), 7 to 17 *s* after the beginning of the transmission. The value of the normalized signal is plotted along the X-axis. Beam number is plotted along the Y-axis. Color shows the number of occurrences of the AGC signal value in each 2 *dB* resolution bin per 10 *s* of data considered.

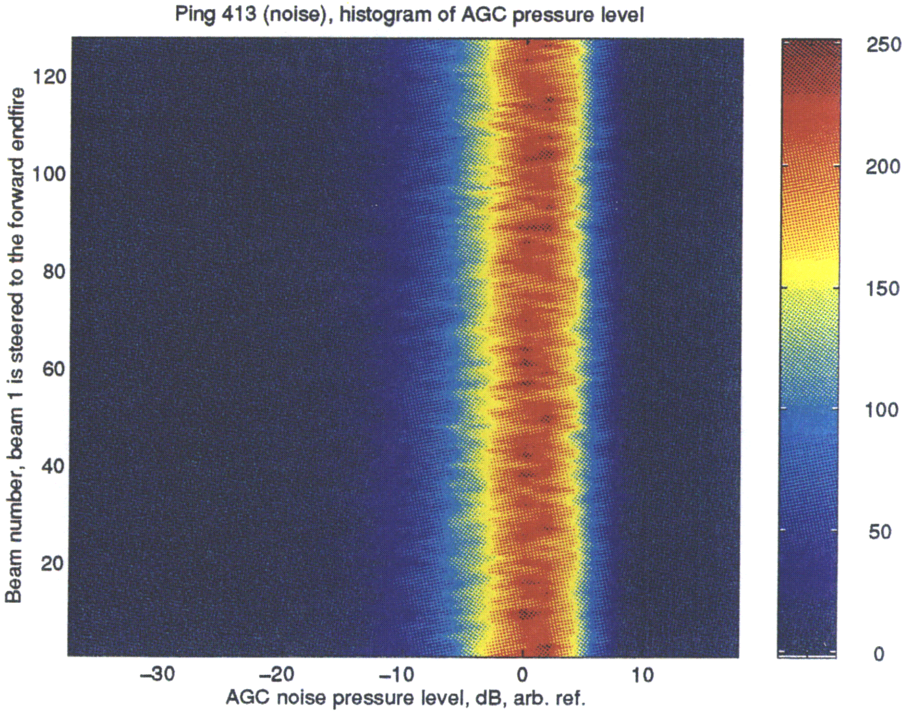

Figure 6.6: Histogram of the AGC noise. 1 *s* sliding mean was removed for normalization. The recording was made during ping 413 (J197, starting at 05:48 Z), 7 to 17 *s* after the beginning of the transmission. During this time no waveform receivable by the Cory Chouest was transmitted, therefore the reception is noise. The value of the normalized signal is plotted along the X-axis. Beam number is plotted along the Y-axis. Color shows the number of occurrences of the AGC signal value in each 2 *dB* resolution bin per 10 *s* of data considered.

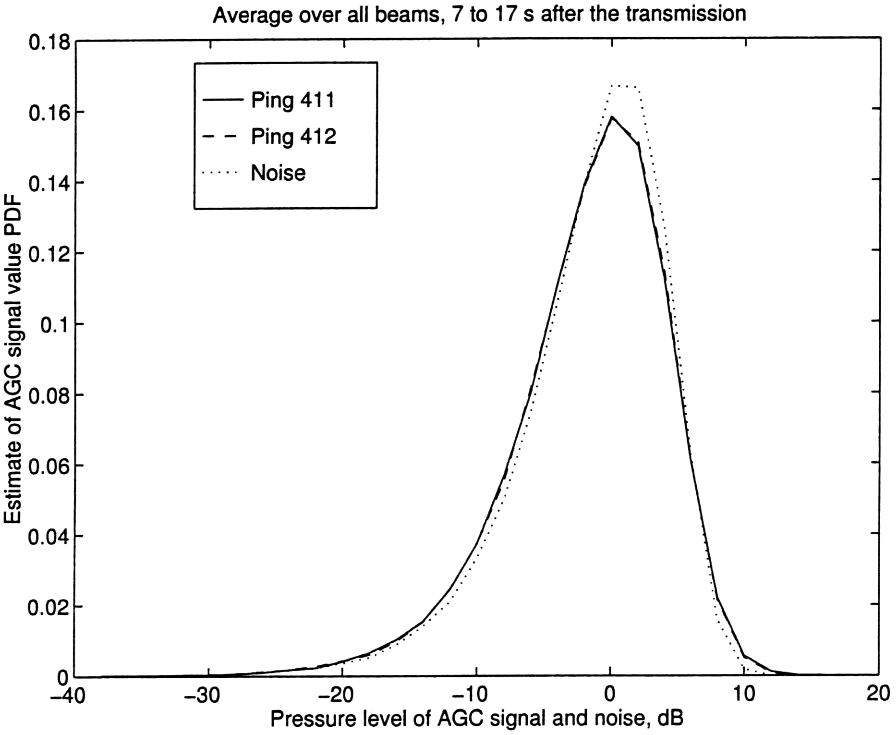

Figure 6.7: Histogram of the average over all beams, normalized signal, measured by the Cory Chouest receiver. Solid line: Ping 411 data. Dashed line: ping 412 data. Dotted line: ping 413 (noise recording). Value of the normalized signal is plotted on the X-axis, number of occurrences in the 2 *dB* bin is plotted on the Y-axis. Data were collected 7 to 17 *s* after the beginning of the corresponding segments.

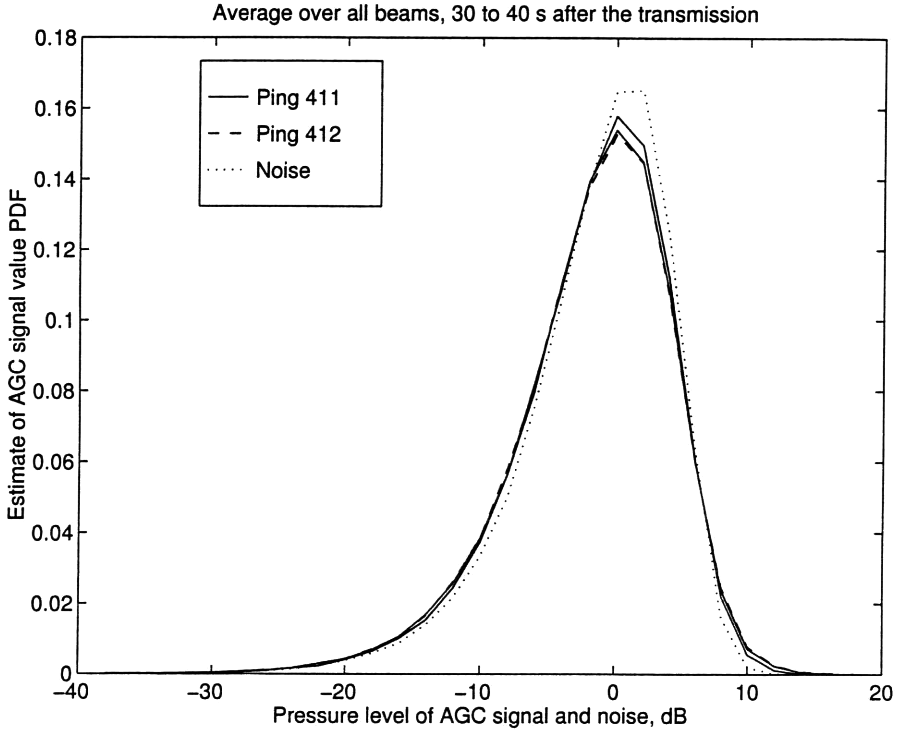

Figure 6.8: Histogram of the average over all beams, normalized signal, measured by the Cory Chouest receiver. Solid line: Ping 411 data. Dashed line: ping 412 data. Dotted line: ping 413 (noise recording). Value of the normalized signal is plotted on the X-axis, number of occurrences in the 2 *dB* bin is plotted on the Y-axis. Data were collected 30 to 40 *s* after the beginning of the corresponding segments.

main lobe arrivals, respectively. Data for ping 411 are plotted with a solid line, data for ping 412 are plotted with a dashed line, and data for noise are plotted with a dotted line in each figure for comparison.

Overall, recorded reverberation data and noise have almost similar histograms, and consequently, almost alike probability density distributions. However, there is some difference between data and noise. Histograms for data show a slightly lower most probable value and a slightly higher density for higher values. This means that the reverberation signal spends relatively more time at its extreme values (either high or low) then the Gaussian noise.

As for the comparison among reverberation data from different pings, or at different times, there is negligible difference.

6.2.2 Peak statistics in the received signal

The observed slight difference between noise and signal data prompts a concern that the data reduction and interpretation thus far may be inadequate. The reverberation data have slightly higher probability density at its extreme value than does the noise. Thus the data are more "peak-like" in nature. In fact that is what one would expect from a high resolution scattering experiment [103, 104, 105]. One way to highlight this kind of behavior is to trace the statistics of individual peaks in the data record. To do so, I set an arbitrary threshold and count the number of peaks exceeding the threshold per unit time.

I consider again the early returns found in the data 7 to 17 s after the transmission, and the main lobe returns in the recording 30 to 40 s after the transmission. I choose a threshold value equal to 2 dB. This value is "high enough" to select strong peaks only. The peak detector performance is demonstrated in Figure 6.9, where I plot the original data with a solid line, and the detected peaks are highlighted with stars. It is seen that only peaks stronger than the threshold are selected.

Next I peak detect the AGC signals in each receiver beam recorded during segments 411, 412 and 413, the latter one being noise. Results for the early returns, in terms of the average measured separation between two adjacent peaks, and their standard deviation, are presented in Figures 6.10 and 6.11, respectively. Corresponding results for the main lobe arrivals are plotted in Figures 6.12 and 6.13, respectively.

For both early and main lobe arrivals it is seen that on average consistently larger separations are detected in pings 411 and 412 (when the reverberation signal is present) than in ping 413. The other feature seen on

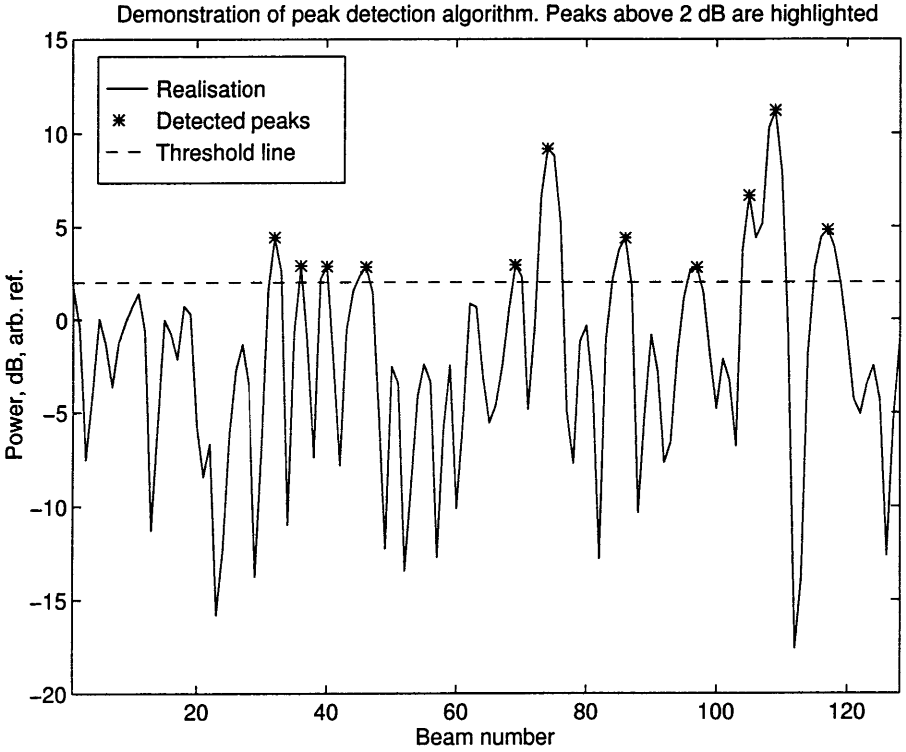

Figure 6.9: Demonstration of the peak detection algorithm. Only peaks exceeding the threshold (dashed line) are selected.

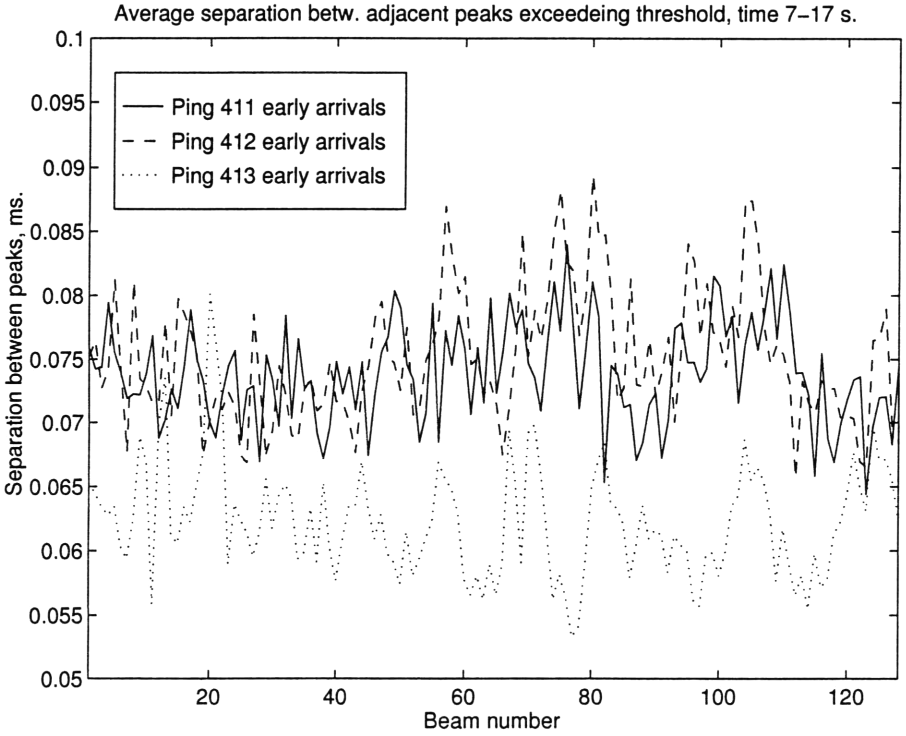

Figure 6.10: Average separation between two adjacent peaks as a function of the beam number. Data were recorded 7 to 17 *s* after the beginning of the corresponding segment (early arrivals). Solid line: ping 411. Dashed line: ping 412. Dotted line: ping 413 (noise)

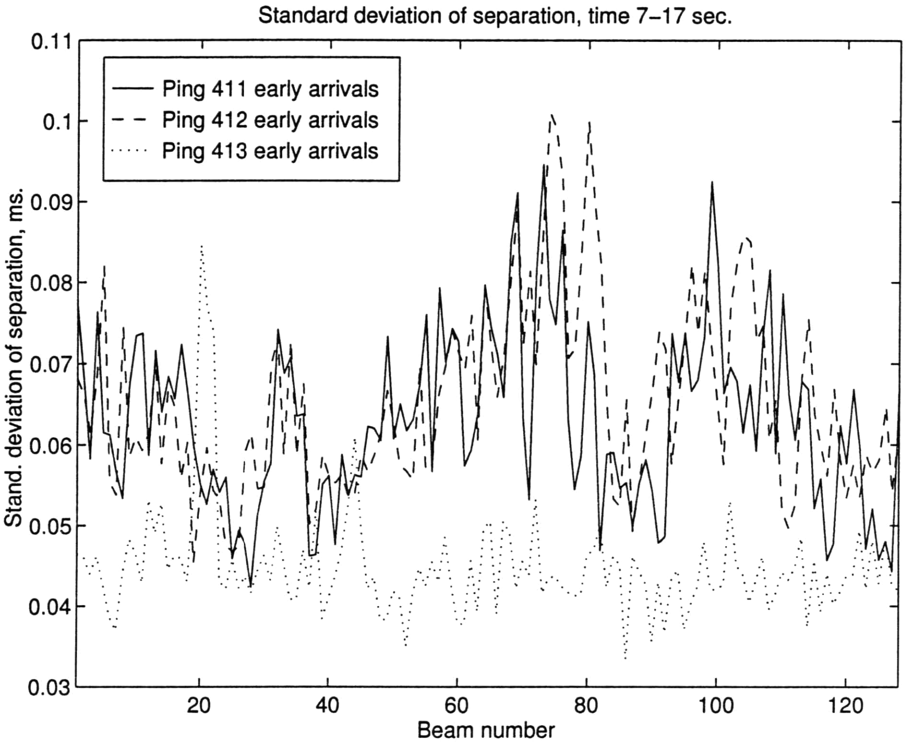

Figure 6.11: Standard deviation of separation between two adjacent peaks as a function of the beam number. Data were recorded 7 to 17 *s* after the beginning of the corresponding segment early arrivals). Solid line: ping 411. Dashed line: ping 412. Dotted line: ping 413 (noise)

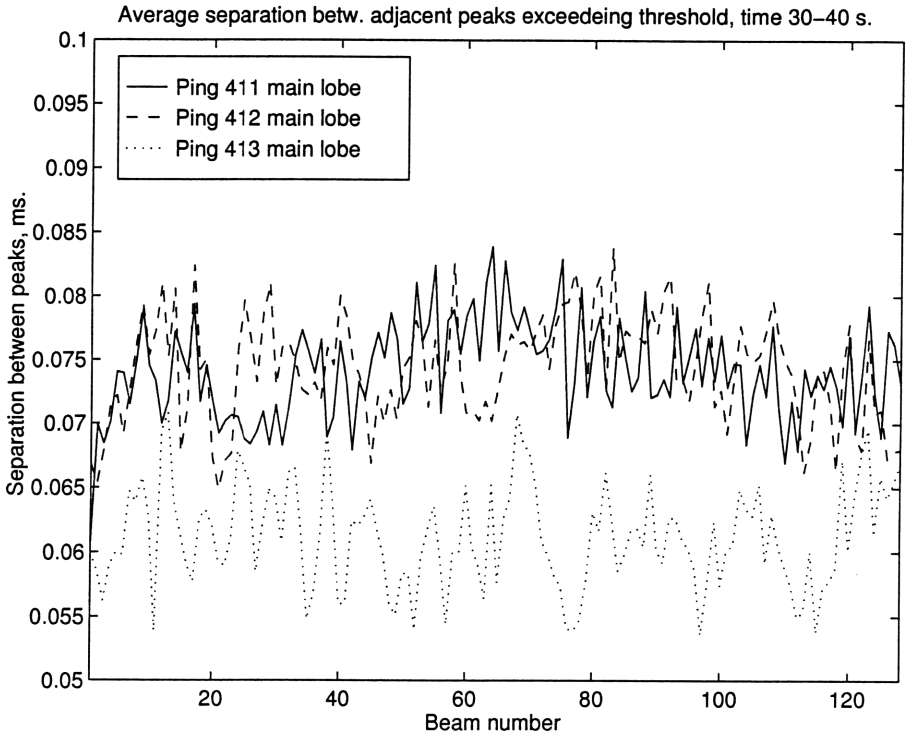

Figure 6.12: Average separation between two adjacent peaks as a function of the beam number. Data were recorded 30 to 40 *s* after the beginning of the corresponding segment (main lobe arrivals). Solid line: ping 411. Dashed line: ping 412. Dotted line: ping 413 (noise)

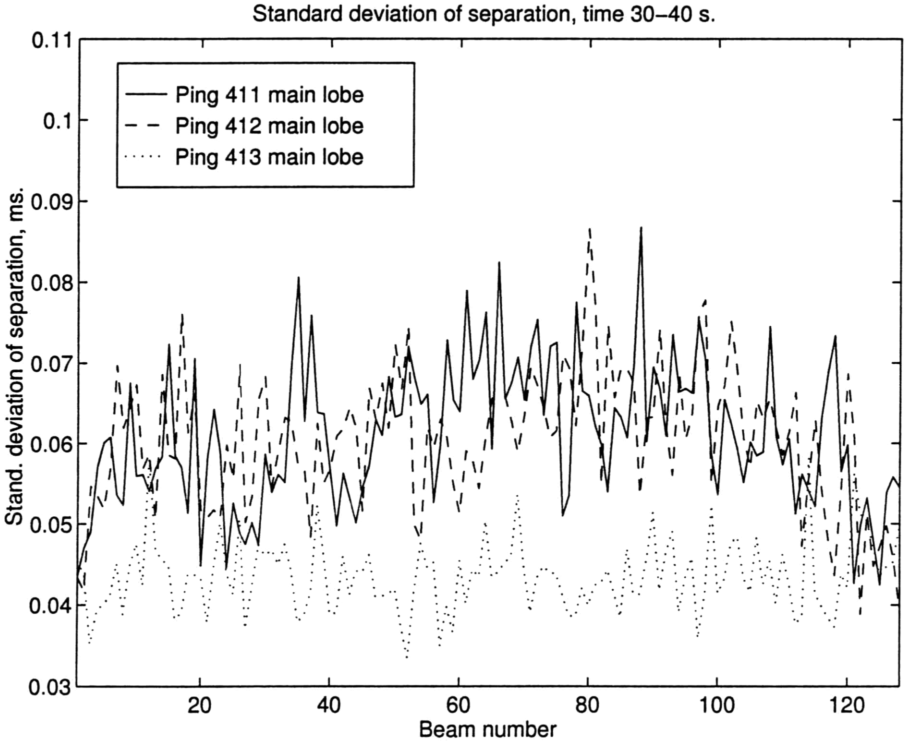

Figure 6.13: Standard deviation of separation between two adjacent peaks as a function of the beam number. Data were recorded 30 to 40 *s* after the beginning of the corresponding segment (main lobe arrivals). Solid line: ping 411. Dashed line: ping 412. Dotted line: ping 413 (noise)

the figures is that same average separation between adjacent peaks was measured for different beams and for different times. To summarize this point, I compute the average across all beams for each plot. Results are in Table 6.1. It is clearly seen in the table that separation observed between peaks is consistently larger when the reverberation signal is present.

Realization processed	Average separation, ms, between adjacent peaks
Ping 411, early arrivals	74.2
Ping 412, early arrivals	74.3
Ping 411, main lobe arrivals	73.9
Ping 412, main lobe arrivals	75.2
Ping 413, early arrivals	61.2
Ping 413, main lobe arrivals	62.3

Table 6.1: Average separation between adjacent peaks detected in early and main lobe arrivals of normalized (1 s sliding mean) data recorded during pings 411, 412 and 413. Strong reverberation signals were received during pings 411 and 412. No appreciable reverberation signal was present during ping 413.

One possibility for the larger interpeak separation is that the statistical properties of reverberation and noise are different. The other possibility is that normalizing the reverberation signal by its sliding mean did not remove all large scale components in the signal. To address this issue, I compare the mean value of the normalized signal when reverberation is present with the mean value of normalized noise. Results are plotted in Figure 6.14. In the figure I plot two curves. The dashed curve shows the average value of the AGC signal observed in each beam of the received signal during ping 411 main lobe arrivals, relative to the AGC noise (ping 413), measured at the same time and and in the same beam, expressed in percents. The solid curve shows average separation between adjacent peaks found in each beam in the ping 411 AGC signal during main lobe arrivals, relative to the corresponding interpeak separation of the ping 413, also expressed in percent.

It is seen that presence of the reverberation signal causes about 20% increase in the separation measured between adjacent picks, even though no significant difference is seen between mean levels of the AGC signal and AGC noise (amplitude of the AGC signal is about 100% of the amplitude of the AGC noise). I therefore conclude that peak detection reveals a real statistical difference between reverberation and noise.

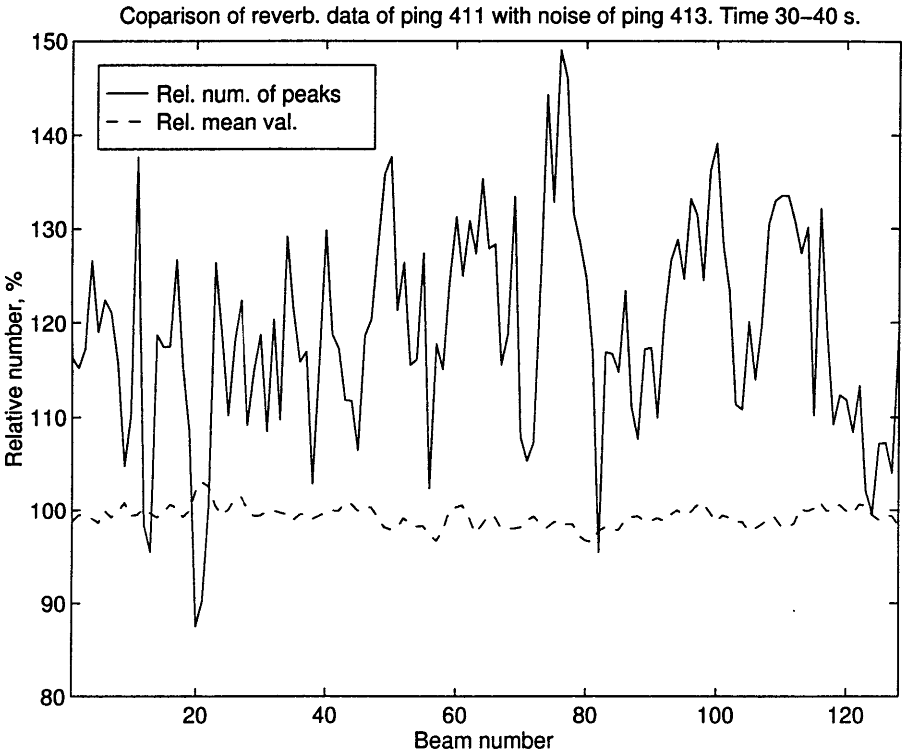

Figure 6.14: Dashed line: ratio of the average AGC signal (ping 411) to the AGC noise (ping 413). Solid line: average separation measured between adjacent strong peaks in the AGC signal (ping 411) relative to the average interpeak separation found in the AGC noise (ping 413). Signals in pings were recorded 30 to 40 *s* after the beginning of the transmission.

Finally, I conclude that there is no apparent difference for reverberation received early and late in time, and in different receiver beams. Signals received early in time are generally due to scattering at relatively steeper grazing angles than the signal received later in time. Signals received in the broadside beam are due to scattering from smaller patch sizes than signals received at the same time in the forward or aft beam. Therefore, since there is no difference in peak statistics observed at different times and in different beams, then there is no dependence of the separation between two adjacent peaks on both incidence grazing angle and ensonified area. To check for a possible time dependence, I compute an average separation between peaks during a relatively short time window of 1.4 s, as a function of time and beam number (Figure 6.15). It is seen in the figure that there is neither a well defined time dependence, nor a well defined dependence on the beam number, of the average separation observed between adjacent peaks. I also compute the standard deviation of individual separations contributing to the average value (Figure 6.16). It is seen in the figure that the standard deviation also appears uniform in time and across beams.

Therefore my conclusion is that there is no difference in the statistical properties of signals scattered from patches of different size on ocean bottom

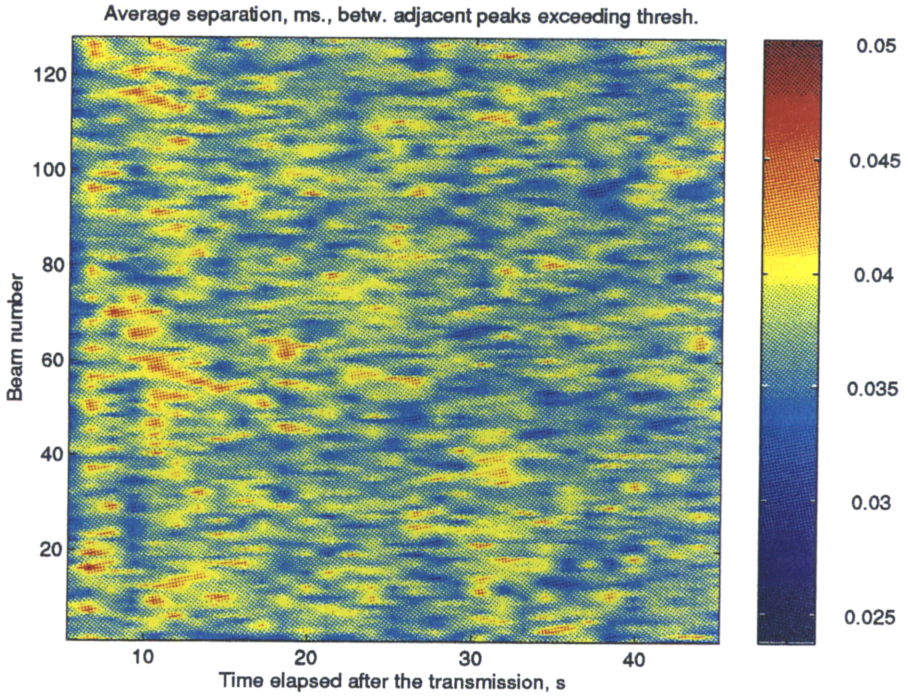

Figure 6.15: The average separation between adjacent strong peaks in the AGC signal as a function of time (X-axis) and beam number (Y-axis), in 1.4 s time window. The recording was made during ping 411. A relatively smaller number of peaks in each time/beam resolution bin results in higher variability of measured average separation from bin to bin. Color shows separation time in ms.

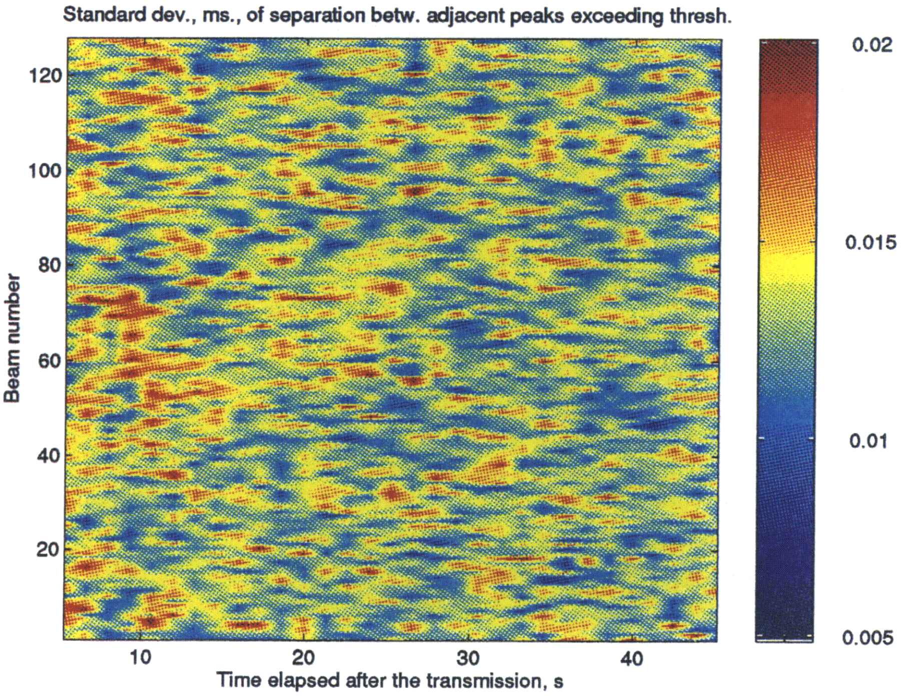

Figure 6.16: Standard deviation of separations between strong adjacent peaks observed in a 1.4 *s* window in the AGC signal as a function of time (X-axis) and beam number (Y-axis). The recording was made during ping 411. A relatively smaller number of peaks in each resolution bin results in higher variability from bin to bin. Color shows separation time in *ms*.

and at different incidence angles.

6.3 The higher order statistics in bistatic AR-SRP data

So far I analyzed backscattering data generated due to patches of different size on the bottom and for different incidence grazing angles, and found no significant difference. I shall now proceed to bistatic data. Considering bistatic data I can investigate dependence of the received signal statistical properties not only for backscattering, but for different bistatic angles as well.

6.3.1 Partitioning of the bistatic data

The experimental geometry for the monostatic experiment was relatively easy. For this, a generally smaller area is ensonified at any given time in the broadside beam of the receiver than in forward or aft beams. Also, as time evolves, the incidence angle changes from almost normal to almost grazing. So if there was a dependence of reverberation on area or grazing angle, I would readily detect its presence, although I would not know the exact functional form of the dependence.

It is not so simple with bistatic data. For any particular point in the received time series there is no general simple rule to attribute scattering from specific areas on the bottom, and to connect them with specific grazing angles. From raytracing it can also be shown that even close points in the time series can correspond to different values of the bistatic angle. Therefore bistatic data must be approached differently. First, through sound propagation considerations, I establish a relation between time and beam number in the received signal recording, and patch on the bottom, responsible for scattering. Then data must be grouped, and uniform data subsets have to be analyzed independently.

To make the subsets uniform, first I must guess which parameters are important, and then partition the data in such a way that all relevant parameters stay unchanged within the subset. I chose to partition data in incidence, scattering and bistatic angles only. Since analysis of the monostatic data showed no dependence of received signal statistics on the bottom patch area, I do not partition data in area, even though raytracing establishes the relation between ensonified area and reception time. For the same reason I do not partition data in transmission loss and source/receiver parameters found by the raytracing.

Since points close in time in the time series can now correspond to very different scattering conditions encountered on the bottom, I may have to remove short scales of the process before performing peak detection. I shall approach this issue in a slightly different manner. Instead of guessing the appropriate length of the sliding average, I shall try several possible lengths and explore the difference.

Additionally, partitioning of the data record into several subsets means that each individual subset may be small. Therefore, I have to use data acquired during several pings. I choose segments 430, 436, 469, 480, 486, 490, 492. These are consecutive segments in which beamformed signals recorded by the Alliance are available. Cory Chouest transmitted its LFM signal $WT93RP019$ at the beginning of each segment. A strong deterministic feature (known as B') is seen by the receiver in each segment. Even though it was useless during processing of partitioned data, it was helpful for the partitioning.

To perform partitioning I first need to solve a propagation problem, i.e., to relate levels measured at each time and in the each beam to bistatic and grazing angles. For all analyzed bistatic data I used raytracing to a flat horizontal plane located at 4500 m depth. Details on the raytracing together with some justification of the approach are in Appendix A.

After the propagation problem is solved, each particular point in the time series is assigned its unique values of angles. To group points, I select "bins", and group points with angles belonging to the bin. I choose 10 degree bins in grazing angle, and 20 degree bins in bistatic angle. For peak statistics I chose to analyze only "long range data", i.e., data collected 30 s and more after the beginning of transmission. The main reason for this choice is that due to large ship separation there is usually no scattering signal earlier in time. It also happens that when the propagation distance is large compared to the depth, a small error in depth results in even smaller error in the computed values of angles (Appendix A). Therefore, it is relatively safer to use angle values obtained from the flat bottom solution for sound signals propagated to long ranges.

6.3.2 The peak statistics in the received signal

Since analysis of individual peaks in the received data is a better indicator of statistical properties of the received signal, and hence a better reflection of the physics of scattering, I proceed by applying the peak detection algorithm to the bistatic data, so as to analyze the statistical properties of individual peaks.

Since no dependence of received signal statistics on bottom ensonification area and on incidence grazing angle was found for the monostatic data, I first try to uncover a possible dependence on bistatic angle. After partitioning the data in incidence, scattering and bistatic angle, I process low grazing angle data found in 10^0 bins of incidence and scattering angle. From the selected data records I remove a 500 ms, 213 ms or 107 ms sliding average mean. A value of 2.5 dB is chosen as a peak detection threshold.

As before, I compute the interpeak separation as a function of bistatic angle. Together with the standard deviation, it is plotted in Figure 6.17 for different values of length of the sliding mean. Additionally I compute the average normalized signal value observed in the peak and standard deviation (Figure 6.18) and, to indicate the statistical validity, the number of peaks detected (Figure 6.19). On all figures zero bistatic angle corresponds to the backscattering case, and 180^0 means forward scattering.

It is clearly seen that for any length of the sliding mean considered, both the average interpeak separation and the average peak value remains approximately the same, until a bistatic angle of about 100^0 is reached. Then

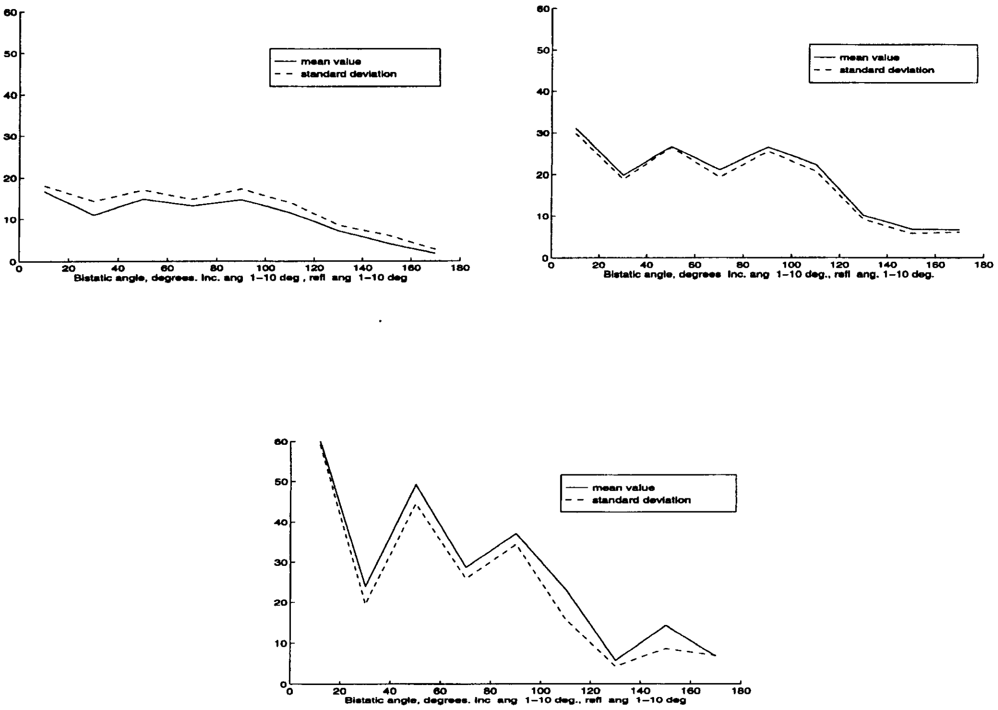

Figure 6.17: Solid line: average separation measured between strong adjacent peaks as a function of bistatic angle. Dashed line: standard deviation of separations. Bistatic angle 0^0 corresponds to the case of backscattering, 180^0 is forward scattering. Upper left plot: 500 *ms* sliding average removed. Upper right plot: 213 *ms* sliding average removed. Lower plot: 107 *ms* sliding average removed. Separation is measured in "pts", 1 pt = 6.67 *ms*.

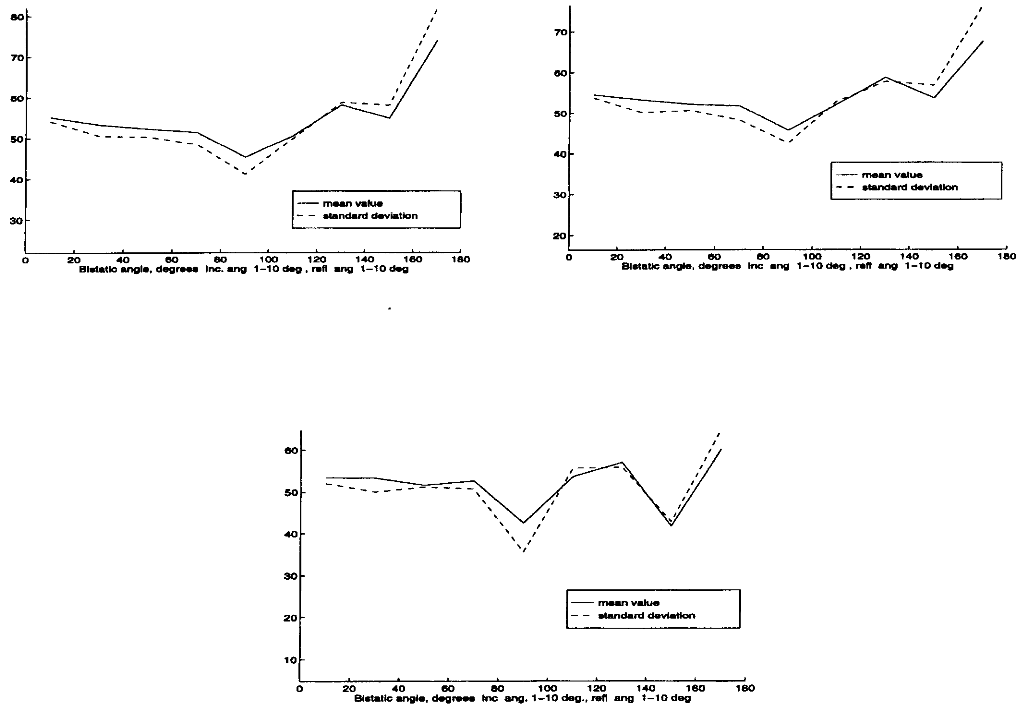

Figure 6.18: Solid line: average value measured in strong peaks as a function of bistatic angle. Dashed line: standard deviation of contributing values. Bistatic angle 0^0 corresponds to the case of backscattering, 180^0 is forward scattering. Upper left plot: 500 ms sliding average removed. Upper right plot: 213 ms sliding average removed. Lower plot: 107 ms sliding average removed.

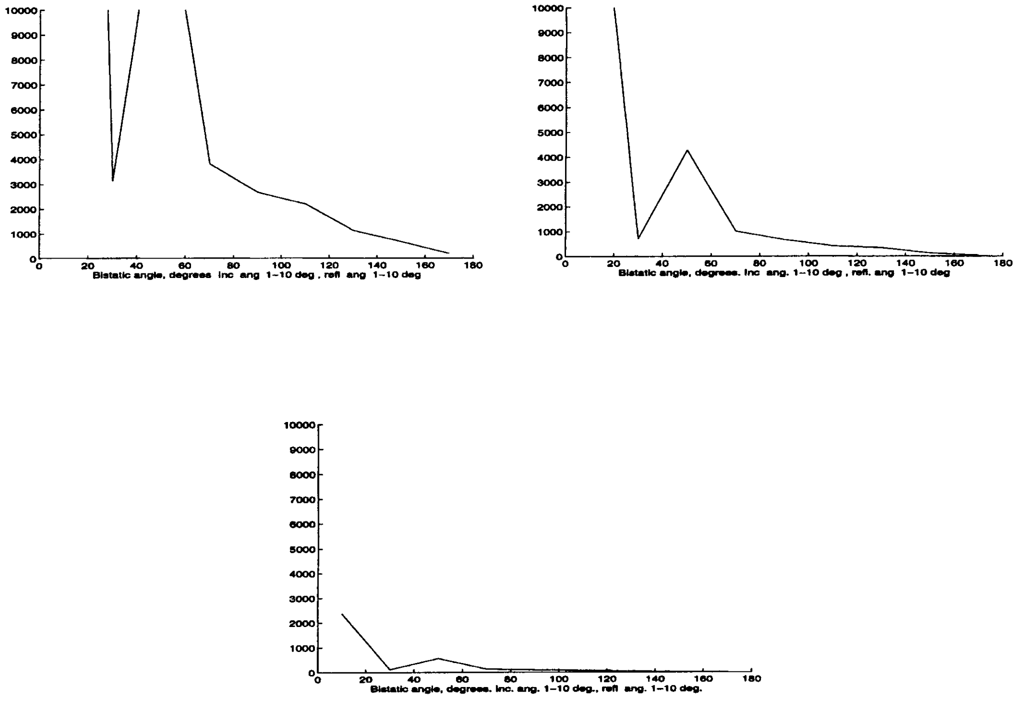

Figure 6.19: Number of processed peaks as a function of bistatic angle. Bistatic angle 0^0 corresponds to the case of backscattering, 180^0 is forward scattering. Upper left plot: 500 *ms* sliding average removed. Upper right plot: 213 *ms* sliding average removed. Lower plot: 107 *ms* sliding average removed.

the separation rapidly decreases and reaches its minimum value at forward scattering.

A different statement can be made on the observed normalized value. For longer averaging (500 and 213 ms), the average individual peak value increase with angle for bistatic angles larger than 100^0. However, smaller interpeak separations and higher peak values are observed simultaneously, and suggest that the average signal level is too high, i.e., that the normalization was not properly selected, and the averaged data do not have a stationary mean value. However, at the shorter value of the sliding mean (107 ms), the peak value remains approximately constant, while the interpeak separation still decreases at bistatic angles from 100^0 to 180^0. Thus I conclude that averaging over 107 ms results in a signal having an almost stationary mean value. And since there are notably smaller values of the interpeak separation for higher bistatic angles, I conclude that it is a statistical property of the data rather than the effect of improper normalization.

As for the number of detected maxima, it is fairly large for averaging, but becomes considerably smaller for the 107 ms case, especially for large bistatic angles. This precludes use of a sliding mean shorter than 107 ms, and explains the larger statistical fluctuations seen.

6.4 Discussion

6.4.1 Summary of observations

It was found that removing a 1 *s* sliding average from backscattering reverberation data effectively "stationarises" the mean value of the process and thus makes it more suitable for statistical analysis. Shorter scales were seen in the bistatic data, therefore shorter sliding averages were used.

Comparison of the statistical properties of normalized reverberation data for monostatic pings 411 and 412 with normalized Gaussian noise recorded during segment 413 yielded some differences. First, from computed histograms I discovered that the reverberation signal consistently spent more time at its extreme values (either high or low) than the noise. Second, the separations between two adjacent strong peaks (exceeding a 2 *dB* threshold) are consistently larger in reverberation data. These two findings are consistent. Since via normalization the mean value is set to be same for both reverberation and noise, fewer peaks observed means higher individual peak values.

I found no difference in backscattering for different incidence angles and areas of ensonified patches. Hence the physics of backscattering remains the same for the range of incidence angles and areas encountered, but different from those of the noise.

Analyzing low grazing angle bistatic data, I found that on average the separation between adjacent strong peaks remains constant for bistatic angles ranging from 0^0 (backscattering) to approximately 100^0. Then it rapidly decreases and reaches its minimum value at a bistatic angle equal to 180^0 (forward scattering). This behavior persists for different sliding means removed from data. Thus there is an important difference in the physics of scattering between forward scattering and scattering into all other directions.

6.4.2 The monostatic data

It has long been thought that scattering may be a discrete process, where geometrical features on the bottom contribute to the received signal more or less independently [2, 3]. However, with a sonar footprint large enough one would necessarily observe a combination of several discrete scatterers in each resolution bin. If scatterers are independent, by virtue of the central limit theorem of statistics the process should become Gaussian, and the amplitude and intensity of the observed signal are bound to have Rayleigh and χ^2 probability density distribution, respectively. Since noise is known to be

Gaussian, one would expect to see a "noise-like" appearance of the normalized signal. That explains why Rayleigh statistics of the received signal was inferred analytically and seen in the received signal [106, 107, 108, 109].

However, as resolution of the experiment increases, the observed statistics of the received signal deviates from Gaussian, and consequently the amplitude distribution deviates from Rayleigh [105, 110, 104, 111, 103]. It is usually observed that the probability of a strong return is higher than predicted by the Rayleigh distribution, i.e., the probability distribution function has a larger "tail" for the high resolution AGC signal than for the Gaussian noise.

Both these statements are consistent with observations. The difference between signal and Gaussian noise was found when strong returns were considered, with more high level returns than expected for the Gaussian distributed stochastic process.

I propose the following qualitative explanation of my observations. Strong features can be found both in noise and signal. However, since noise is truly a Gaussian stochastic process, strong features in it are generated when "pathologically many" infinitely small noise sources happen to contribute at the time of measurement. Hence for noise the probability of exceeding a large threshold is very small, and exponentially decays as the threshold increases.

For the signal, and continuing to appeal to the process of discrete scatterers, one concludes that, as for noise, one can see anomalously strong signals due to addition of scattering from "pathologically many small scatterers" that happen at the time of the experiment in the sonar footprint. Statistics of these is clearly Gaussian. However, each discrete scatterer size results in its own characteristic target strength. Hence, another way to have a strong feature in the signal is the presence of a "pathologically strong scatterer". And the statistics of these is not necessarily Gaussian. Instead, it likely reflects the statistical distribution of scatterer sizes on the bottom and the target strength dependence on scatterer size.

The distribution of heights seen on the ocean bottom is known to be fractal. Even though larger scatterers are less likely, there is a power law relation between scatterer size and probability of a given scatterer size. And since the power law gives a decay slower than the exponential, one would expect to see in the reverberation data more "highs" than in the Gaussian noise.

6.4.3 The bistatic data

Assuming that the previous section supports the discrete nature of scattering, I shall attempt to address peculiarities observed in the bistatic data from the discrete scattering point of view. Ideologically, I follow [2].

Consider several scatterers on the base plane. As long as they are small compared to the wavelength, they generate only weak scattering, uniformly distributed in angle. But scatterers of size comparable to the wavelength, and larger, are capable of generating strong returns. However, the bistatic cross section associated with these larger scatterers is not uniform. Instead, it has a strong maximum in the specular direction. Therefore, all strong scatterers present in the footprint will scatter into the specular direction. Considering finiteness of the scatterer size L relative to the wavelength λ, one can expect a strong contribution of those scatterers within their forward lobe, i.e., within a λ/L angular spread from the specular reflection direction. On the contrary, only those sitting on properly oriented local slopes will scatter away from the forward specular direction. As a result, for any given area, more overlapping strong scatterers will contribute in the forward direction than anywhere away from forward. And more overlap results in less separation between strong adjacent events.

It was assumed earlier that through a self-selection mechanism certain scales contribute most to the backscattering [2]. Scattering from larger scatterers is constrained to the specular direction, and the number of those from within a given footprint is bound to be relatively small. Small scatterers, even though present in greater abundance, are not capable of generating appreciable scattering. It was shown that if there is a self-selection process favoring certain scales on the bottom, then scatterers with sizes comparable to the wavelength would dominate the backscattering.

I believe that the same approach can be successfully used to explain bistatic scattering. Its statistical properties were observed to change for bistatic angles 100^0 and larger. This supports the conclusion that the in-plane total width of the forward lobe of scatterers contributing effectively to forward scattering is about 160^0. And this corresponds to a scatterer size of about one wavelength, i.e., a size consistent with the idea that wavelength size scales are responsible for the observed strength of scattering.

This conclusion emphasizes that in trying to address higher order statistical properties deterministically, one has to provide better than wavelength resolution in solution of the propagation problem, particularly in knowledge of the rough bottom. Given $\lambda = 6\,m$ in the ARSRP experiment, a characteristic depth of 5 km and propagation distances $> 10\,km$, this seems hardly possible. Strong scattering events seen once are very unlikely to be seen again at the same place, if the experiment is repeated, but of course would be repeated in a statistical sense.

6.5 Conclusions

In summary, I conclude

- That scattering is discrete in the monostatic reverberation data. It manifests itself in the variation away from Gaussian of the received time series statistics. The reverberation signal appears more peak-like than the Gaussian stochastic process, a result best seen when only strong peaks are analyzed.

- The scattering process is discrete in the bistatic data as well, at least with use of indirect arguments. Analysis of the bistatic data leads one to the conclusion that wavelength size scatterers are those contributing the most to the scattering process.

Chapter 7

First Order Statistics: the Reverberation Strength

7.1 The theory

Given that scattering can be dominated by wavelength-scale details of the rough surface, how should I now approach the scattering problem? Clearly, not completely deterministically.

7.1.1 Facets

Imagine a sound wave incident upon a rough surface (see Figure 7.1).

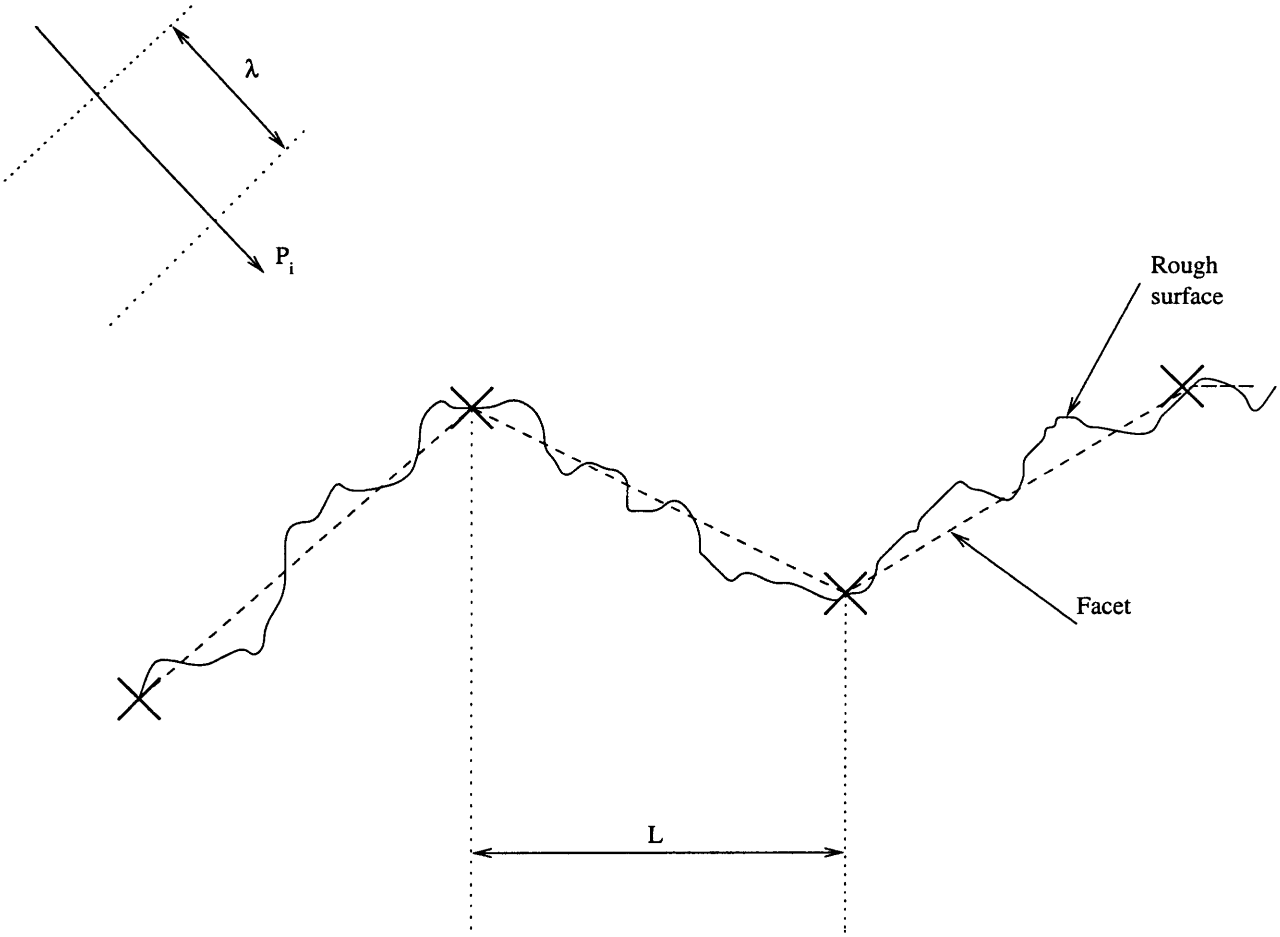

Figure 7.1: Representation of the surface in terms of facets.

In the figure some points are shown with crosses. These can be deterministically known points on the surface, i.e., a pointwise representation of the measured deterministic part H of the surface. Then one way to build an estimate of H is to connect them with straight lines. Deviations of the true surface from the resultant piecewise continuous estimate of H forms a stochastic part of the bathymetry h. To establish terminology, the part of real surface located between two crosses is what I call the "deterministic facet". (Clearly, in three dimensions three points define a three-dimensional facet. Only two dimensions are shown in the figure to simplify the reasoning, and a line connecting two crosses represents a projection of the facet onto the plane.) If both the size of a deterministic facet L_d and deviations of the real surface from it are small compared to the wavelength, then I can say that the surface consists of deterministic facets only, and scattering from it can be approached deterministically.

However, a deterministic approach is unlikely to be useful for the rough ocean bottom. For instance, even for a frequency of 10 Hz, which is too low to be used in most underwater applications, the wavelength is about 150 m, and for a deterministic solution bathymetry must be known with roughly 10 m resolution. In the typical ARSRP scenario $\lambda = 6\ m$ meters, and the bathymetry is mostly known only on a 200 m grid. Clearly, a deterministic approach will be useless. Not knowing the exact rough shape, I have to resort to a statistical description of the surface.

Consider a realization of the surface. To define the right approach to the scattering problem the Rayleigh criterion can be invoked. If the average rms roughness accumulated in the sonar footprint is small compared to the wavelength, and the grazing angle is small, I can use a perturbation approach to solve the problem. On the contrary, if the rms roughness is large, Lambert's Law is supposed to become useful. However how does one approach the intermediate case, where rms roughness is too large to allow a perturbation solution and yet too small for the Lambert's Law to be applicable?

I find it convenient to use a somewhat different approach. For surfaces not known well enough to allow a deterministic solution of the scattering problem, I define a scale L (or area S in three dimensions) on which the rms roughness is comparable to the wavelength. Then I put crosses separated by the distance L from each other. Connecting crosses with straight lines I create again a piecewise representation of the surface. Following [85], I designate the resultant straight pieces of the surface as rough facets ("rough line" in two dimensions).

Clearly, idealization as in the foregoing via facets is relevant when knowledge about the true surface is incomplete. However, usefulness of the rough facet notion can be easily extended further into the deterministic domain. Let us assume that the precise surface shape is miraculously known. Even knowing the ocean bottom with that much precision, we may be unable to establish precise source and receiver locations, sound speed profile etc., not to mention that the ocean bottom may be changing its shape and small size features via microtectonic or weathering processes. Equivalently, one may be interested in the scattering averaged over different realizations of bottom. In both cases deterministic knowledge is insufficient for the solution, the simplifying statistical approach can provide the solution, and the notion of the rough facet is useful. In either case, the mean local slope is derived from local slopes of the deterministic surface, and scattering properties corrected by this slope are derived from the rough facet properties.

7.1.2 Qualitative considerations

With this view of facets, a succession of scales is defined. The smallest scale relevant to the problem is the wavelength scale. The largest relevant scale is the sonar footprint size. Relation of these to the deterministic and rough facet lengths determines the scattering behavior of the surface. In this sense, facets are major building blocks in the assessment of scattering from the surfaces.

A major simplification can be achieved by use of the rough facet for the case of its size large compared to the wavelength. Then in the succession of scales it takes an intermediate position. Two cases are now possible.

First, consider the case where many rough facets can be placed within the sonar footprint. Then, at each instant of time, combined contributions from all rough facets will be received by the sonar. Since the rms roughness is comparable to the wavelength, it is suggested by the Rayleigh criterion that the contribution of individual facets can be added incoherently. This means that each scattering event registered by the sonar is a mixture of many independent individual events, arriving at random phase. By virtue of the central limit theorem, the resultant stochastic process is Gaussian, and only its first order statistic, i.e., the mean value, is of interest. To find the mean, in turn, I need to solve the scattering problem for one individual facet, and to average it over rough facet slopes. Compare it to the initial problem: initially I had a nonstationary surface, depending on the sonar footprint geometry, with a possibly large value of the Rayleigh parameter. Now the Rayleigh parameter for the individual facet is fixed at the unity level. It was shown by numerical modeling [56, 6] that in this case, even a first order perturbation solution gives a reasonable result. Therefore, a simple analytical solution is possible for an individual facet. The only remaining problem is averaging over rough facet slopes. Clearly, a notable simplification is achieved compared to the initial problem.

Another case to consider is where only a few facets are in the sonar footprint. In this case there is no averaging over local slopes. If an average over realizations of the surface scattering is of interest, then again it can be computed using averaging over local slopes, and the central limit theorem guarantees that its distribution will be Gaussian. However, it can not be said to be valid for an individual scattering event. At each instant of time we see scattering from a particular local slope, and the distribution of these slopes together with the shape of the bistatic scattering cross section of the individual facet will dictate the received signal statistical distribution.

7.2 Scales involved in the ARSRP experiment

Since footprint and rough facet sizes are important for understanding the scattering process, I estimate both for the experimental environment, starting from the footprint.

7.2.1 Interrogated patch on the bottom

The size of the interrogated patch on the bottom is determined by two scales: L_1, which is determined by the pulse temporal resolution, and L_2, which is determined by the receiving array beamwidth.

Under an assumed generic sound speed $c = 1500\ m/s$, the pulse temporal characteristic length L_t can be determined to be about $20\,ms$. The corresponding interrogated length in the ensonified direction on the bottom can be calculated from geometrical considerations:

$$L_1 = L_t / \sin\theta_i \tag{7.1}$$

where θ_i is a local incidence grazing angle between incident wave vector $\vec{k}$ and a local reference plane on the bottom.

The interrogated length perpendicular to the L_1 direction is determined by receiver array beam width α, and distance R traveled by the sound:

$$L_2 = R \sin \alpha \tag{7.2}$$

These two length scales can be quite different. For instance, for a 5000 m depth, and for a typical sound speed profile, it can be found that a grazing incidence angle $\theta_i = 10^0$ on the horizontal bottom corresponds to R of about 20 km. Then L_1 for $L_t = 20\, ms$ is approximately 100 m, and L_2 for the broadside and endfire beams is equal to approximately 500 and 5000 m, respectively, which are an order of magnitude larger.

7.2.2 The ARSRP geology

The ARSRP experiment was conducted in the Midatlantic ridge area North-East of the Kane fracture zone. It is well known that the power spectral density in the collected bathymetry data comply very well with the Goff-Jordan spectrum. Therefore, at any scale, the statistical properties of the bottom can be found if parameters of the Goff-Jordan distribution are known.

I start with a direct estimate of the rough facet size. The highest resolution data (2 m sell size) are available in a rectangular area which extended 550 m along the X coordinate and 1050 m along Y, with the origin of the patch located at (191150; 2944100) UTM coordinates, or approximately at

26.5840^0 North and 48.1010^0 West. The size and resolution of these data allows one to compute roughness statistical characteristics of the bottom for surface wavenumbers ranging from 3 m^{-1} to 0.01 m^{-1}. A contour plot of the patch is shown in Figure 7.2. It is seen that only part of the patch contains valid data. What appears in the left upper and right lower corners will be excluded from the processing. "Valid" high resolution bathymetry data chosen for processing are highlighted with gray color.

Within the valid data region I choose 20 patches of size 80 by 80 m. In each patch I first remove the best fit plane. The slope of the removed plane can be considered a local slope, and the remaining is a rough facet of size 80 by 80 m. Raw data for roughness observed in each individual patch are shown in Figure 7.3.

Averaging over facets, one ends up with a mean rms roughness equal to 6.4 m with standard deviation 2.5 m. The former is about equal to the acoustic wavelength, therefore the rough facet size can be estimated as 80 m.

The next thing to estimate is the correlation length measured within the rough facet. It can be estimated independently in X and Y directions. If there is anisotropy on the scale of the rough facet size, different correlation lengths would be expected in the two different directions. Raw data for

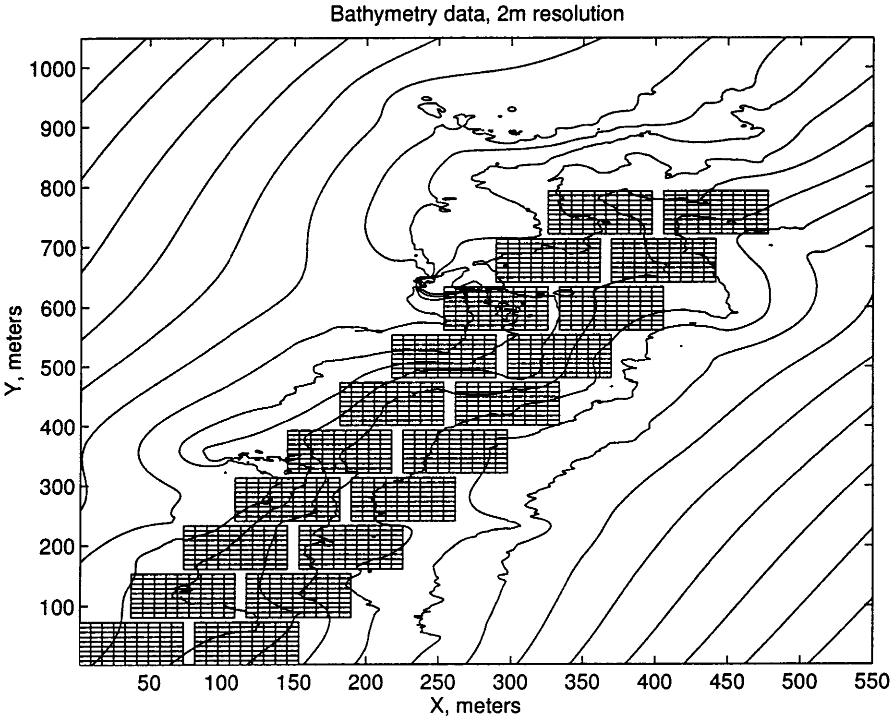

Figure 7.2: High resolution bathymetry data. "Valid" data selected for processing are highlighted with gray color.

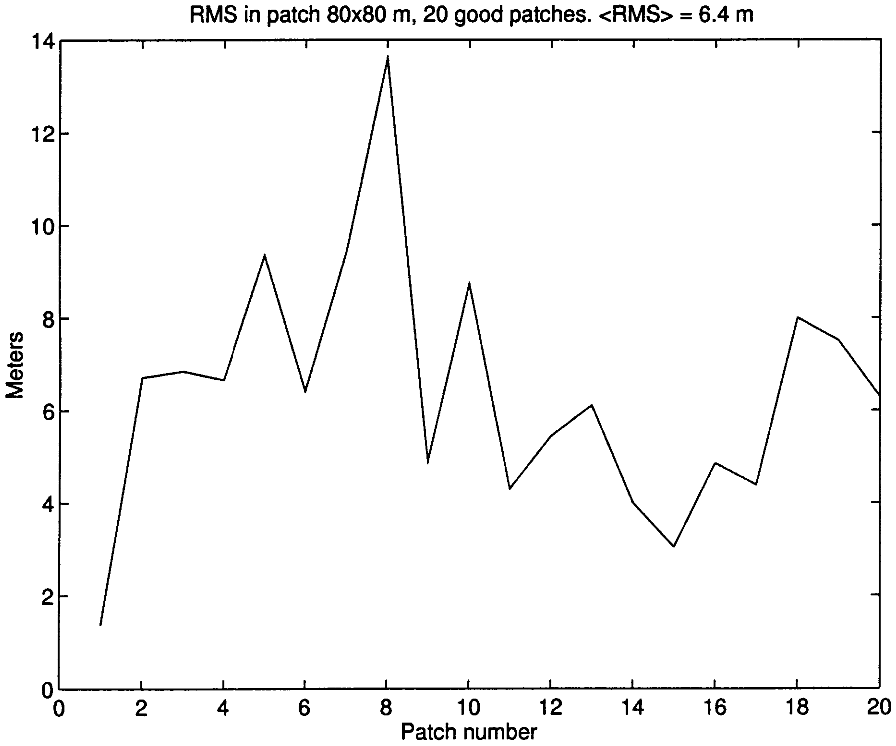

Figure 7.3: Rms roughness measured in the individual patch of size 80 by 80 m as a function of the patch number. The average over all patches rms roughness is 6.4 m.

correlation lengths seen along X axis and Y axis are shown in Figures 7.4 and 7.5, respectively.

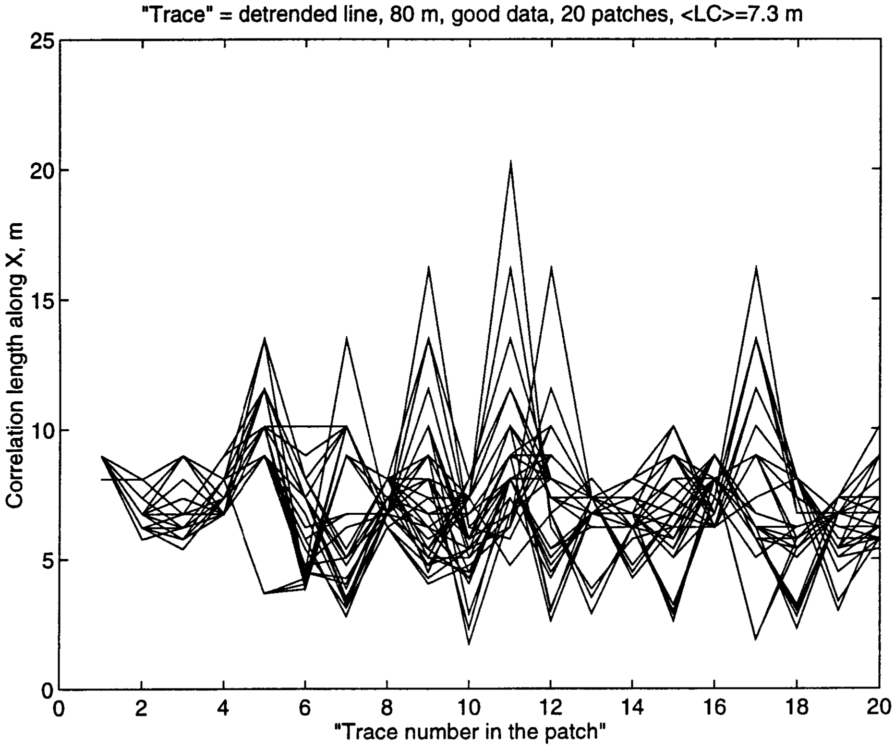

Figure 7.4: Correlation length measured in individual cuts of 80 meters length along the X axis. Average correlation length was found to be 7.3 m.

Average values of the correlation lengths computed along X and Y axis are 7.2 and 7.3 m, respectively, with standard deviations of 2.1 m, i.e., no anisotropy was seen in the high resolution bathymetry data on the 80 m length scale. It supports an observation [112, 32] that anisotropy is a large

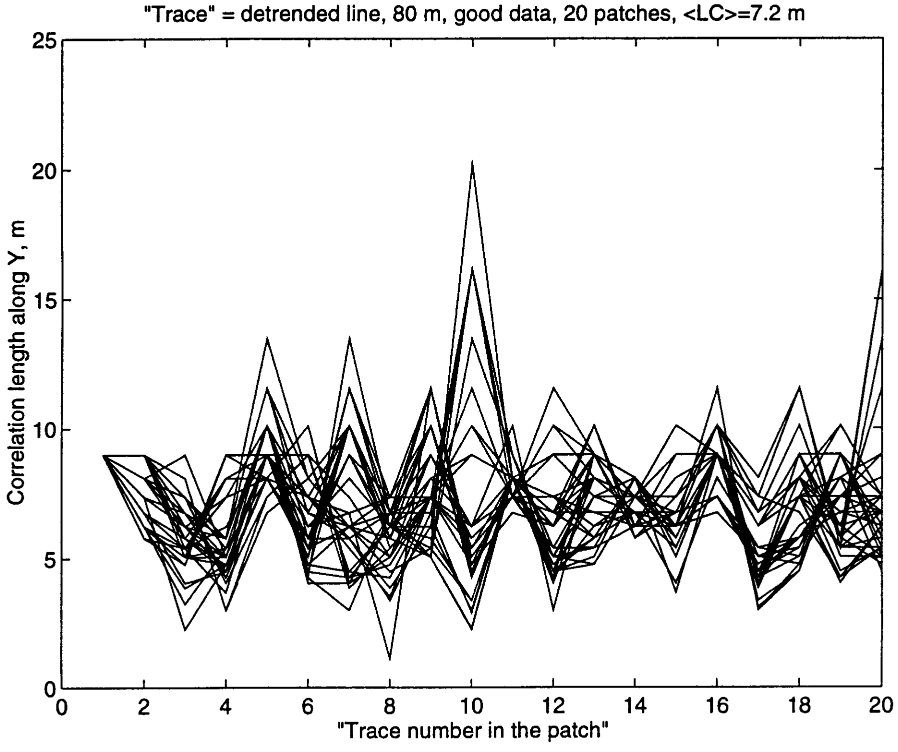

Figure 7.5: Correlation length measured in individual cuts of 80 meters length along the Y axis. Average correlation length was found to be $7.2\,m$.

scale property, not seen on small enough scales in deep ocean.

Finally, I estimate individual power spectra in the X and Y directions, and compare them with the Goff-Jordan spectrum using the appropriate rms roughness and correlation length (Figures 7.6 and 7.7, respectively). Good match of the measured spectra and those predicted using the Goff-Jordan model is obvious.

7.3 The experiment

7.3.1 The selected data

I use the same partitioned data that were used for second order statistics. However, now I consider the behavior of the "sliding mean" itself. First, the data must be partitioned by the incidence, scattering and bistatic angle. Again, the grazing angle bin is set to 10^0, and the bistatic angle bin is chosen to be 20^0.

Since strength of scattering is now of interest, propagation effects must be excluded from consideration. First, source level and transmission losses (calculated by the raytracing method) must be subtracted from the received pressure level. Next, I assume that the square of the scattering amplitude is

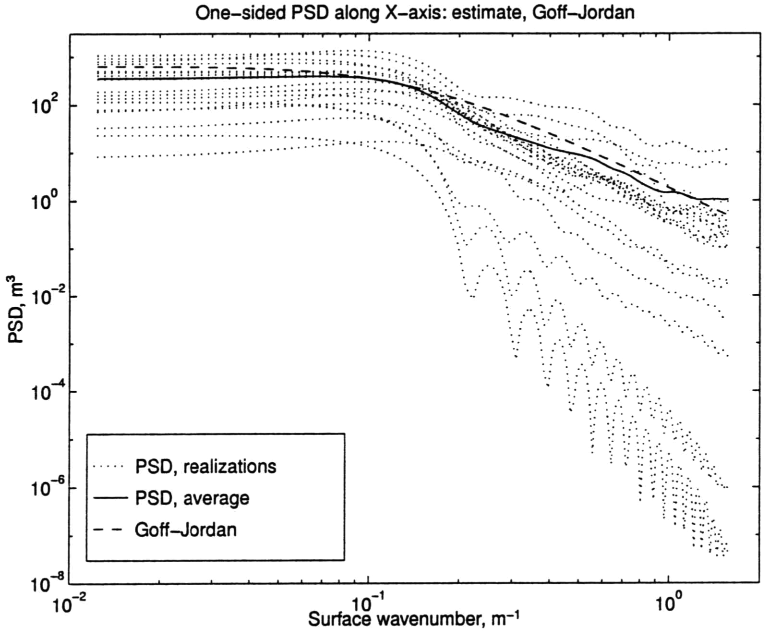

Figure 7.6: Estimate of power spectral density (PSD) in 80 m cuts along the X axis. PSDs for individual patches are plotted with a dotted line. The PSD average over all patches is plotted with a solid line. The Goff-Jordan PSD is plotted as a dashed line. All PSDs are one-sided.

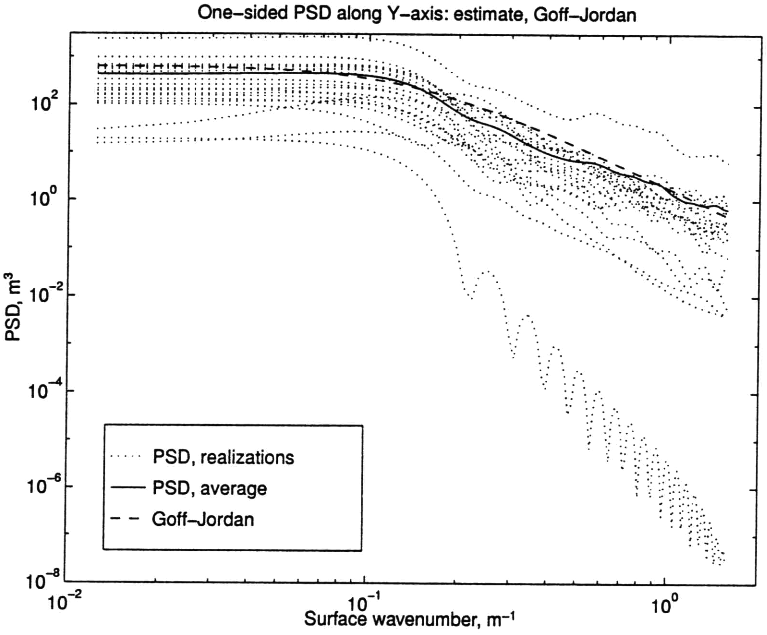

Figure 7.7: Estimate of power spectral density (PSD) in 80 m cuts along Y axis. PSDs for individual patches are plotted with a dotted line. The PSD average over all patches is plotted with a solid line. The Goff-Jordan PSD is plotted as a dashed line. All PSDs are one-sided.

proportional to the ensonified area, which is true when several rough facets are found within the sonar footprint, and subtract 10 log(area) from the measured received pressure level. If my assumptions and the propagation model are correct, the resultant pressure level is the bistatic scattering strength.

7.3.2 The scattering strength

To analyze the behavior of the scattering strength, I plot it for given incidence angle as a function of the scattering and bistatic angles. The coordinate system is shown in Figure 7.8.

For the time being, I consider low grazing angles. In Figure 7.9, the scattering strength as a function of bistatic and scattering angle, for incidence grazing angles ranging from 1^0 to 15^0, is plotted. The discussion follows.

7.4 Modeling of the scattering strength

Understanding the scattering process means being able to model it correctly. I will consider several models, starting with the simplest (which is not nesesserely correct).

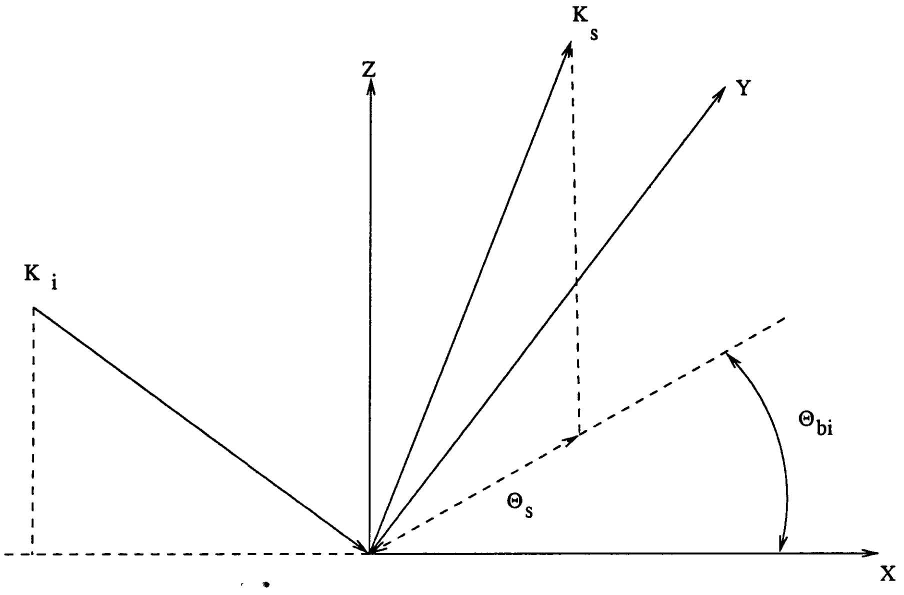

Figure 7.8: Coordinate system for the scattering strength measurements and modeling. The incident wave vector is in the XZ plane. The XY plane is the scattering interface. In the XY plane, the polar angle is the bistatic angle θ_{bi}, and radius is the scattering angle measured from normal (from the Z-axis).

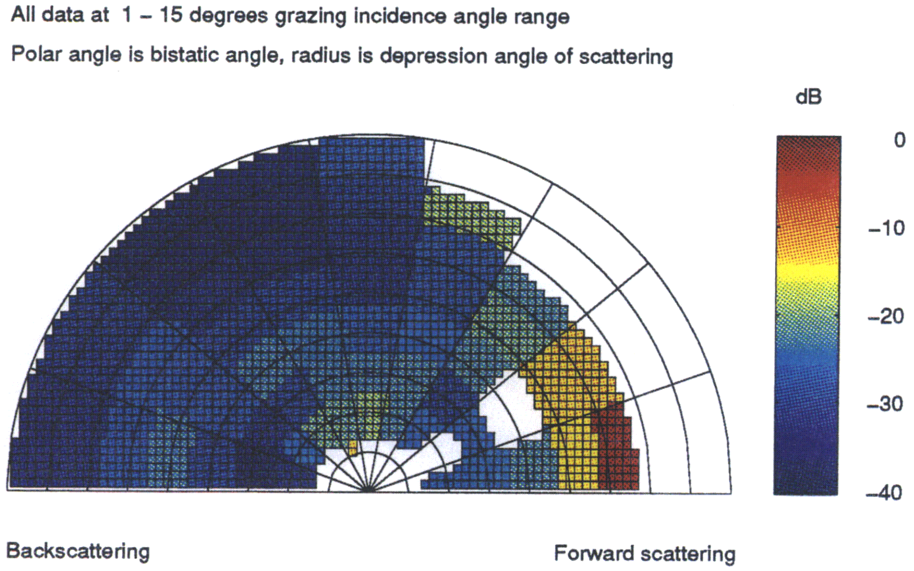

Figure 7.9: The bistatic scattering strength as a function of scattering and bistatic angle, for data in the 1^0 to 15^0 incidence grazing angle range. The polar angle is the bistatic angle, and radius is the scattering angle measured from normal (depression/elevation angle), in degrees, from 0^0 (at the origin) to $\pm 90^0$.

7.4.1 Lambert's Law

Lambert's Law in the form (4.13) has long been used in rough surface scattering. Because of its simplicity, it is conventionally applied even when its applicability conditions are violated. To improve the fit to data, the Mackenzie coefficient μ is normally adjusted, where $\mu = 1/\pi$ $(10\log\mu \approx -5\,dB)$ is the strict Lambert's Law result. One disadvantage of the procedure was already noted: the value of Mackenzie coefficient is empirical, hence can not be predicted by theory. However, this is not the only drawback. Lambert's Law with any constant value of the Mackenzie coefficient fails to predict bistatic scattering adequately. A plot of the Lambert's Law prediction for an incidence angle 8^0, with Mackenzie coefficient $10\log\mu = -15\,dB$ is shown in Figure 7.10. Differences between data and the Lambert's Law prediction are obvious. First, Lambert's Law is overall "flatter" than data. Second, highest values are seen in the data near the specular direction. On the contrary, Lambert's Law is isotropic in bistatic angle, hence no bistatic "highs" are predicted. Clearly, this model is inapplicable to the data collected.

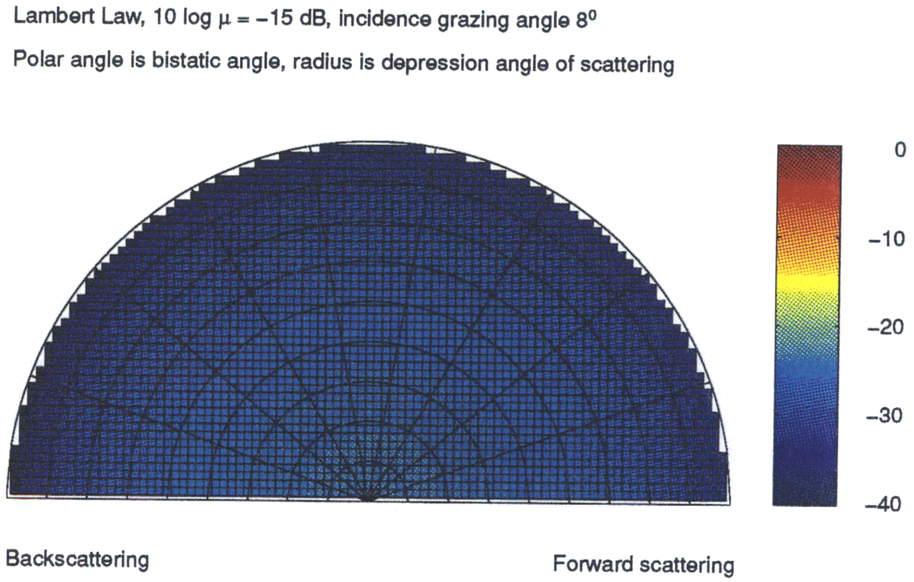

Figure 7.10: The Lambert's Law prediction of the scattering strength. Mackenzie coefficient is chosen $10\log\mu = -15\ dB$. The polar angle is the bistatic angle, and radius is the scattering angle measured from normal (depression/elevation angle), in degrees, from 0^0 (at the origin) to $\pm 90^0$.

7.4.2 The small perturbation solution

Beyond Lambert's Law, one has has two classical analytical solutions: the Kirchhoff approximation, and a small perturbation (SP) solution. The first is favored if steep enough grazing angles are considered. Clearly, since low grazing angles are involved in the data, the small perturbation approach (or the more general 2-scale solution) is chosen.

The characteristic footprint size is about 100 by $1000\,m$. This means that it consists of a few rough facets each about 100 by $100\,m$ in size, elongated in one direction. The natural approach consists of computing scattering from one rough facet and averaging over local slopes. However, since the few facets are seen simultaneously, the local incidence angle varies only slightly from facet to facet. Therefore, the SP solution, which I consider next, is expected to perform reasonably.

The analytical SP solution for a fluid-fluid interface is known for a long while. It can be found, for instance, in [5] (the analytical result is summarized in the Appendix C). The plot of the scattering strength for incidence angle 8^0 is shown in Figure 7.11. It is seen that the scattering is not modeled exactly by this small perturbation approximation. Overall lower levels and steeper decay rates at smaller grazing angles are seen (see also Figures 7.15, 7.17).

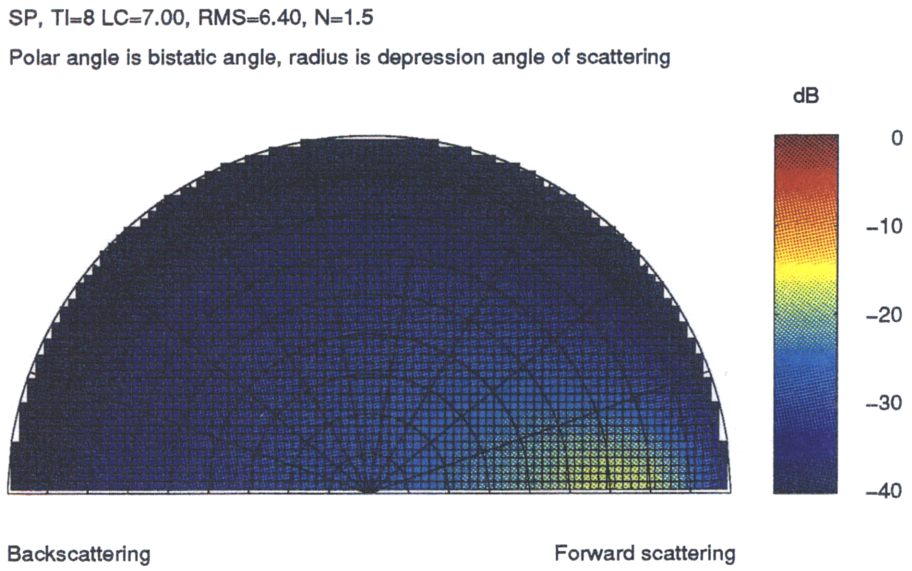

Figure 7.11: Small perturbation solution for the scattering strength. Incidence grazing angle is 8^0. The polar angle is the bistatic angle, and radius is the scattering angle measured from normal (depression/elevation angle), in degrees, from 0^0 (at the origin) to $\pm 90^0$.

First, I try to explain the mismatch between the theory and the data using a 2-scale theory. Data intrinsically involve averaging over several rough facets, i.e., over different local slopes. If the facet is inclined towards the source, the local incidence angle is steeper, hence higher scattering is seen from this facet. To account for this, averaging over local slopes must be considered. Hence, I consider next a 2-scale model (see Figures 7.12, 7.15 and 7.17), where averaging over slopes is performed. To provide a better match with the data in the backscattering direction, the rough facet was rotated around the K_x axis with 0^0 mean and 5^0 rms angle of rotation. A better match between model and data in the back direction is seen. However I do not match the high values observed in the forward direction, and an rms slope of 5^0 chosen to fit data in the back sector is too high for the ARSRP scenario. Therefore, model improvement is still desirable.

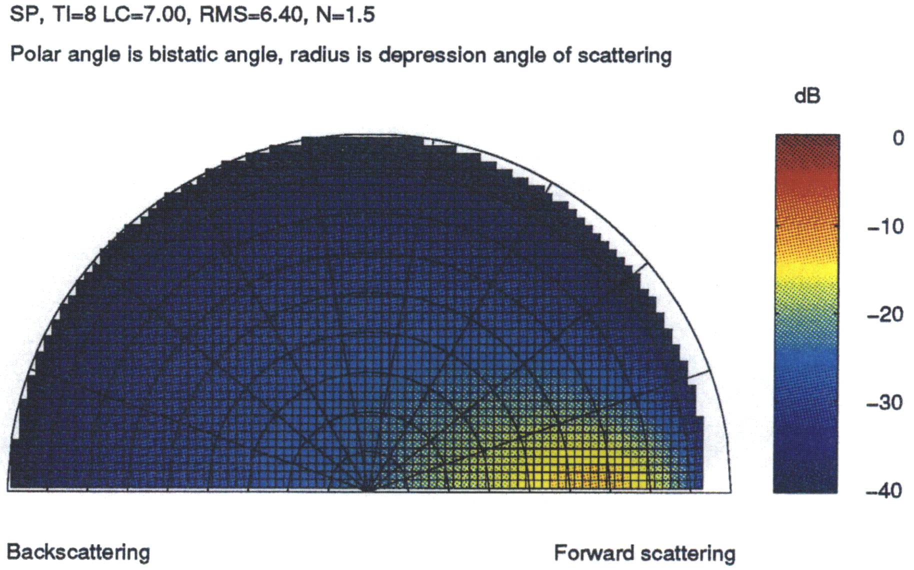

Figure 7.12: 2-scale solution for the scattering cross section. The small perturbation solution is used for the individual rough facet, followed by averaging over local slopes. It is assumed that the mean local slope is zero, and the standard deviation of the local slopes is 5^0. The polar angle is the bistatic angle, and radius is the scattering angle measured from normal (depression/elevation angle), in degrees, from 0^0 (at the origin) to $\pm 90^0$.

7.4.3 Contribution from the small scales (boss-SP solution)

Theoretical considerations

Features too small compared to the wavelength λ do not contribute to the solution. The only effect of features larger then the sonar footprint is introduction of larger values of the mean height and mean slope, which can be easily removed. The scales of interest $L_{interest}$ are confined between a certain large scale L_{large} depending on the interrogated patch size and some small scale L_{small} depending on λ: $L_{large} > L_{interest} > L_{small}$. As a practical limit, $\lambda/4$, $\lambda/8$ or $\lambda/16$ is often used as the smallest scale of interest, when an integral equation solution or another "exact" solution is sought.

However, within these scales, the ocean bottom is irregular with power spectral density $\tilde{W}_h(K)$ decaying between K^{-2} to K^{-3} as $K \to \infty$. Therefore, the surface slopes observed within the rough facet at a small resolution scale are discontinuous, i.e., the smaller L_{small} is chosen, the larger the rms slope is within the rough facet.

The first order perturbation solution considers scales up to $>\approx \lambda/2$ only. On the one hand, this makes the solution robust, since discontinuities of slope are excluded by effectively truncating the power law spectrum of surface irregularities. On the other hand, smaller scales normally considered via the integral equation solution are ignored. Since the probability of finding a feature with the characteristic size a increases as a decreases, the number of features with $a < \lambda/2$ within the sonar footprint may be enormously large, hence the contribution of these features to the scattering strength may not be small. Additionally, these features, acting as point scatterers with scattered power depending on their size, will have a uniform scattering cross section, therefore, they will generate equal energy flux into the forward and back direction. Then it may happen that the contribution to the surface scattering cross section in the forward direction is dominated by the high values generated by the first order perturbation solution. However, those point scatterers may dominate the back sector.

I propose the following semi-analytic treatment of small scales. Since by definition features of interest are small, scattering from an individual feature is independent of its shape. Then I approximate the distribution of irregular features by the distribution of hemispherical bosses with radius a.

The power spectral density of the surface irregularities determines the distribution of feature sizes found on the surface. Therefore I assume that the distribution of features in size is given by the power law:

$$\begin{cases} N(a) = B/a^n, \ \ 0 < a < a_{max}, \\ N(a) = 0, \ \ a > a_{max}, \end{cases} \tag{7.3}$$

where n is a positive power exponent, and the maximum allowed feature size a_{max} will be discussed later.

Then, the corresponding rms roughness h_{boss} generated by all small features modeled as hemispherical bosses can be computed as a function of a_{max}, B and n:

$$h^2_{boss} = \int_0^{a_{max}} N(a) h^2(a) da \tag{7.4}$$

where $N(a)da$ is the number of hemispherical bosses with radius $(a - da/2) < a < (a + da/2)$ found in a unit area of the surface. For hemispherical bosses

$$h^2(a) = \int_0^a 2\pi z(a^2 - z^2) dz = \pi a^4/2. \tag{7.5}$$

Integrating, I end up with

$$h^2_{boss} = \frac{\pi B}{2(5-n)} a^{5-n}_{max}, \tag{7.6}$$

where a bounded value of h^2_{boss} for nontrivial B can be achieved only if $n < 5$.

On the other hand, the rms roughness generated by small scales not accounted for by the first order small perturbation theory can be computed as

$$h_{small} = \int_{K_{min}}^{\infty} \tilde{W}(K)dK \tag{7.7}$$

The isotropic Goff-Jordan power spectrum with correlation length l, rms roughness h_{rms} and spectral exponent $n = 3$ is given by

$$\tilde{W}(K) = \frac{l^2 h_{rms}^2}{2\pi(K^2 l^2 + 1)^{1.5}}. \tag{7.8}$$

Here as usual, K stands for the surface wavenumber, and k is reserved for the acoustic wave number. Substitution of 7.8 into 7.7 yields

$$h_{small}^2 = \frac{h_{rms}^2}{\sqrt{K_{min}^2 l^2 + 1}}, \tag{7.9}$$

which for the case $K_{min} l >> 1$ can be further reduced to

$$h_{small}^2 = \frac{h_{rms}^2}{K_{min} l} \tag{7.10}$$

Since the smallest scale contributing to the first order small perturbation solution (the shortest Bragg resonant grating) for incidence grazing angle θ_i is given by $k + k_{inc,x} = k(1 + \cos\theta_i)$, it seems reasonable to choose

$$K_{min} = k(1 + \cos\theta_i). \tag{7.11}$$

Now, a connection can be found between a_{max} and K_{min}. Corresponding to K_{min}, the surface wavelength is given by $\lambda_{max} = 2\pi/K_{min}$. Then the corresponding feature size equals the wavelength, and its characteristic radius is half of its size:

$$a_{max} = \frac{1}{2}\frac{2\pi}{K_{min}} = \frac{\pi}{K_{min}}. \tag{7.12}$$

Equating h_{boss} and $h_{small,sp}$ one can find B:

$$B = \frac{2h_{rms}^2(5-n)K_{min}^{4-n}}{l\pi^{6-n}}. \tag{7.13}$$

Then using (7.13) and the scattering solution for a distribution of bosses, I can add the contribution of small scales to the SP solution, which results in the composite "boss-SP" scattering theory.

Several analytical solutions exist for the distribution of bosses on the base plane. For instance, I can use the cross section solution given by Twersky [113]

$$\sigma_{boss} = \int N(a) \cdot \frac{k^4 a^6 (6 \sin\theta_i \sin\theta_s \cos\phi)^2}{9} da, \tag{7.14}$$

where θ_i and θ_s are incidence and scattering grazing angle, the scattering interface is in the (XY) plane, the incidence wave vector is in the (XZ) plane, and ϕ is the angle between the scattering wave vector and the Z axis. Then from (7.3) and (7.13) the scattering cross section for the distribution of bosses per unit scattering area is given by:

$$\sigma_{boss} = \frac{2h_{rms}^2 \pi k^4 (5-n)}{lK_{min}^3(7-n)} \cdot (\sin\theta_i \sin\theta_s \cos\phi)^2. \tag{7.15}$$

Robustness of the solution

A few more words must be written on the choice of the power spectral exponent n in the distribution of bosses. The value $n = 0$ corresponds to a boss size equally distributed between $a = 0$ and $a = a_{max}$. Larger values of n result in lesser number of larger bosses, and larger number of smaller ones. Since the power spectral density of the surface irregularities is related to the distribution of feature sizes found on the bottom, it seems natural to assume $n = 3$. However, since this choice can not be rigorously justified, sensitivity of the solution to the choice of n becomes an issue.

To check the sensitivity of the solution to the value of n, the boss scattering cross section was computed for values of n from $n = 0$ to $n = 5$. In Figure 7.13, the difference between solutions for $0 < n < 5$ and for $n = 0$ is shown. It is seen that for a broad range of n (from $n = 0$ to $n = 4$) the solution only slightly depends on the exact value of n, i.e., is robust with respect to the choice of n.

Properties of the solution

First, for a broad range of power exponent $0 < n < 4$ the boss contribution shows only a gentle dependence on the exact value of n. As $n \to 5$, contri-

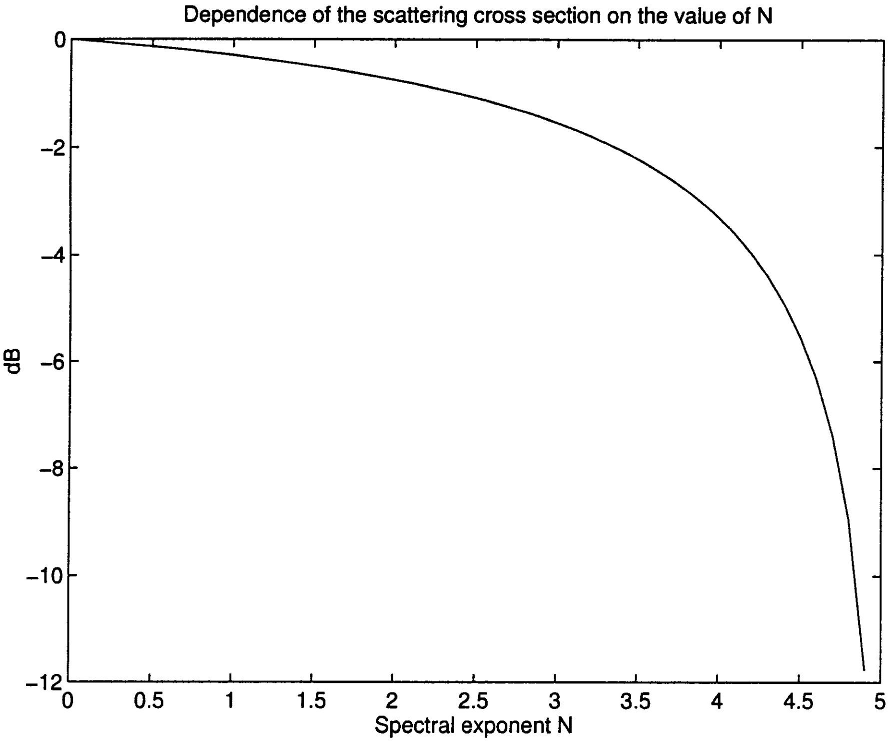

Figure 7.13: Sensitivity of the boss solution to the value of the spectral exponent n. Solution for $n = 0$ is chosen as the reference.

bution of small scales diminishes, so that there is no contribution at all for $n = 5$. For $n > 5$ the value of B in (7.6) becomes infinite, which means that the contribution of the boss solution becomes zero. An interesting property of the boss solution is emphasized here. Larger values of n correspond to steeper decaying power spectrum densities (PSD) of the surface irregularities. On the other hand, since the boss solution contribution diminishes as n increases, a lesser correction to the SP solution results from the surface with steeper decaying PSD of the surface irregularities. For instance, for surfaces characterized by a steep PSD ($n \geq 5$) there is no correction at all. Therefore, I conclude that a correction to the SP solution is needed only when the PSD of surface irregularities decay slowly as a function of the surface wave number.

Application to the modeling of ARSRP scattering data

The resultant combined scattering strength for an individual rough facet is plotted in Figure 7.14, for incidence angle 8^0. For the small scales, a value of the spectral exponent $n = 0$ was used, i.e., a uniform distribution of boss sizes was considered.

From the comparison of Figures 7.9, 7.12 and 7.14 it is seen that reason-

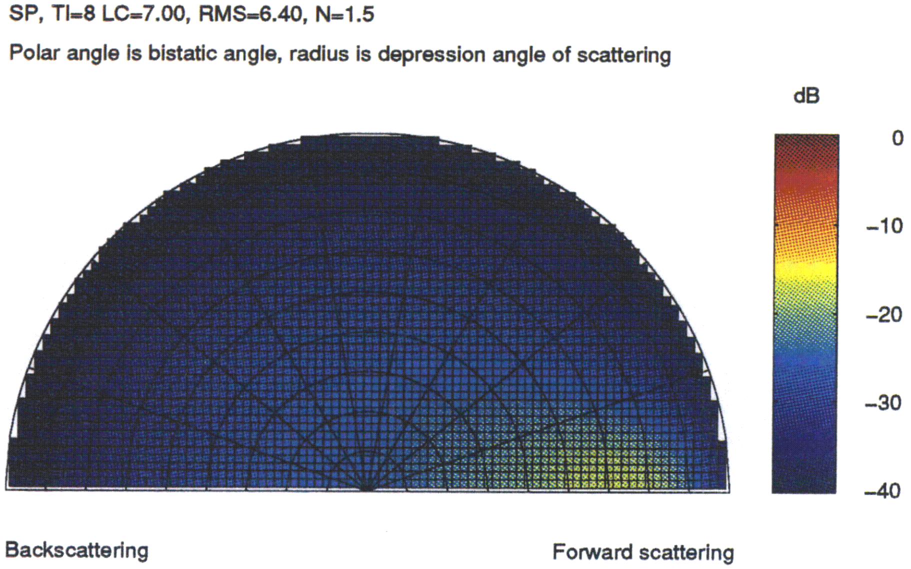

Figure 7.14: Boss-SP solution for the scattering strength of an individual rough facet. Scales smaller then those accounted for by the SP theory were considered using a boss solution by Twersky. The polar angle is the bistatic angle, and radius is the scattering angle measured from normal (depression/elevation angle), in degrees, from 0^0 (at the origin) to $\pm 90^0$.

able match with data at low scattering angles can be achieved using Lambert's Law (via an adjustable Mackenzie coefficient), a 2-scale solution (via adjustable local slopes) and boss-SP solution. However, a mismatch between data and model solutions at scattering angles above 40^0 is still clearly visible.

To understand the reason for the discrepancy and to choose the right model, more in-depth investigations of scattering in the plane of incidence was performed.

7.4.4 Scattering in the plane of incidence

Line plots of the scattering strength are shown in Figure 7.15. The incidence grazing angle for all "model plots" is chosen as 8^0, and data are collected in the incidence angle range from 1^0 to 15^0. In the figure scattering only in the plane of incidence is considered. The abscissa shows the scattering angle counted clockwise from back to forward, so that for the chosen incidence grazing angle a scattering angle of 8^0 corresponds to backscattering, and 172^0 is the specular direction.

Again, a mismatch between models and the experimental data is seen. However, data for all incidence angles ranging from 1^0 to 15^0 are plotted in figure 7.9. It is therefore possible that the data are not uniform. The

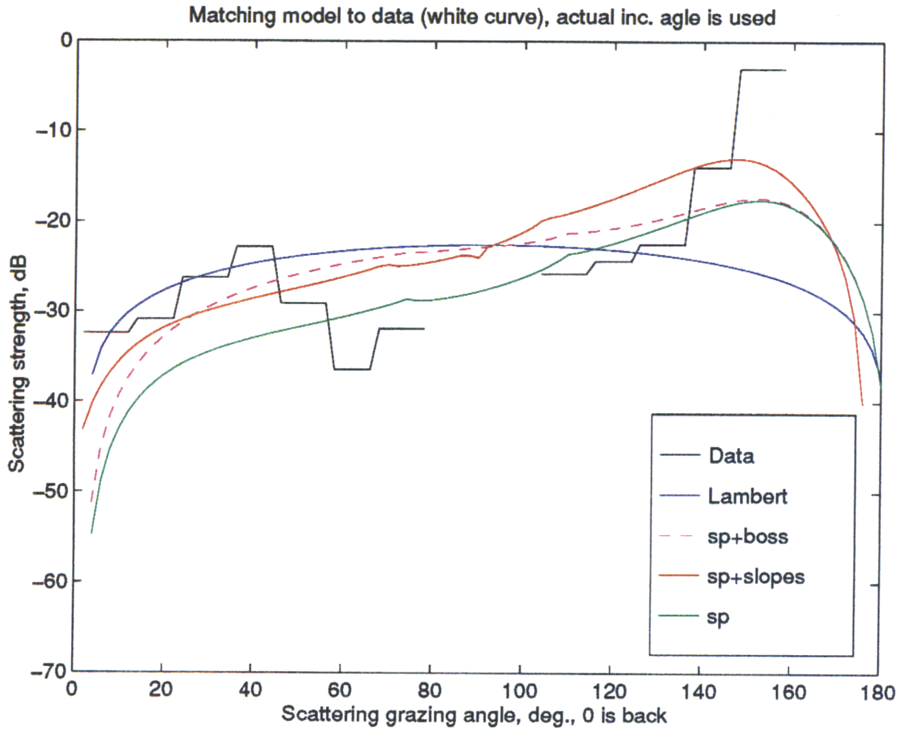

Figure 7.15: Scattering strength for scattering in the plane of incidence. The black line is the measured scattering strength. An incidence angle 8^0 was used for modeling. The blue line is Lambert's Law with $10\log\mu = -15\,dB$. The green line is the first order small perturbation solution for a fluid-fluid interface (zero shear modulus in the bottom). The red line is the 2-scale solution, where averaging over local slopes (rms angle 5^0) was performed. The dashed magenta line is the boss-SP solution for an individual rough facet.

scattering strength for different scattering angles could have been measured at different times within one ping, or during different pings, hence the angle between the incident wave and the bottom may take different values (of course, in the $1^0 - 15^0$ range) for different scattering angle bins. To account for this, I calculate the average incidence angle in the selected data as a function of scattering angle bin (Figure 7.16). It is seen in the figure that

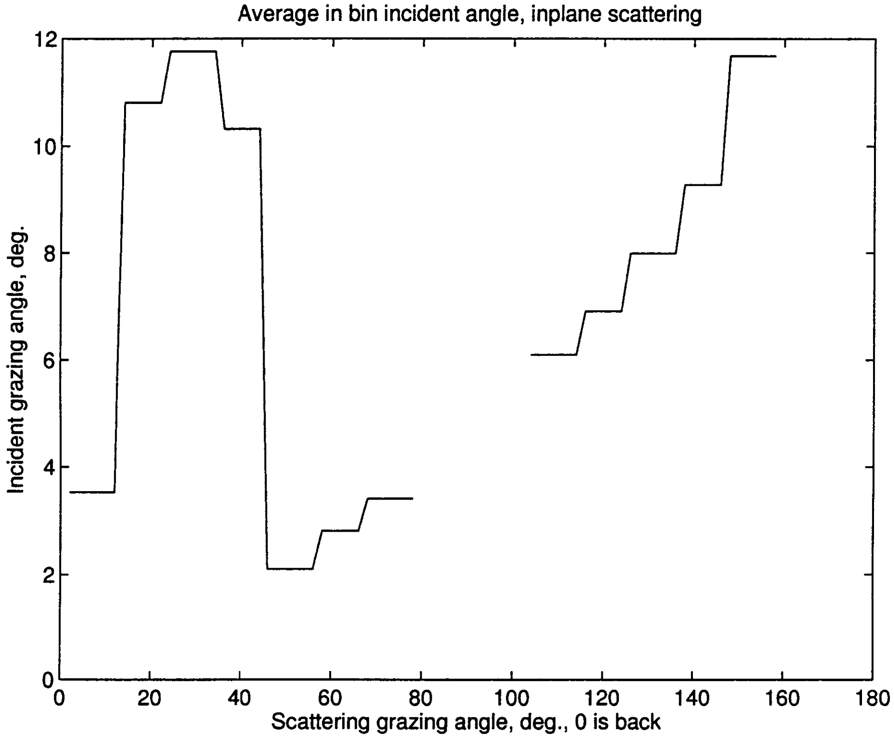

Figure 7.16: Average incidence grazing angle in the data as a function of scattering grazing angle bin for the case of scattering in the plane of incidence.

indeed, very different incidence angles contribute to the scattering at different scattering angles. To account for this, model results were recomputed using actual values of the incidence grazing angle. The results are plotted in Figure 7.17. The discussion of the individual curves follows.

Lambert's Law

To provide for a good fit between Lambert's Law (blue line) and data (black line) for low grazing scattering angles, the Mackenzie coefficient was set to $-15\ dB$. It is seen that Lambert's Law matches reasonably the scattering data up to a scattering angle of 50^0. However, it is also seen that Lambert's curve is "flatter" then the data curve. Made to match at a scattering angle of 50^0, it slightly overpredicts at lower values of the scattering angle. Hence, when the incidence angle suddenly jumps from 10^0 down to about 2^0 at about a 40^0 scattering angle, Lambert's Law fails to "catch up" and starts to overpredict. With use of lower value of the Mackenzie coefficient one can "force" agreement between Lambert's Law and data in the $50^0 - 80^0$ scattering angle range, but then its performance at low grazing angles will be compromised. This means that it is impossible to use one value of the Mackenzie coefficient to explain scattering for a broad range of incidence and

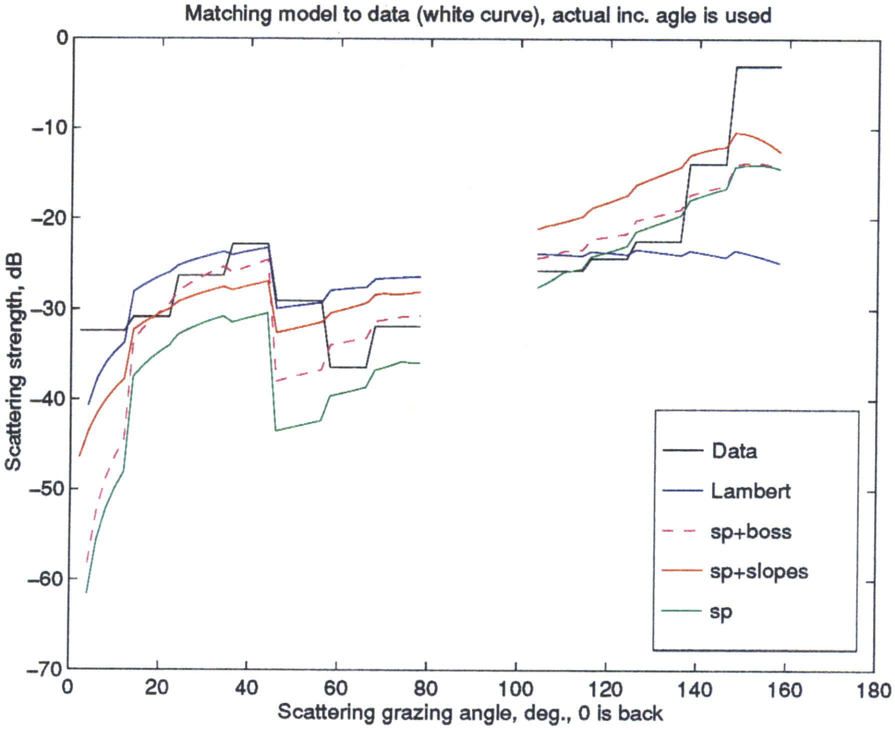

Figure 7.17: Scattering strength for scattering in the plane of incidence. The black line is measured scattering strength. The actual incidence angle was used for modeling. The blue line is Lambert's Law with $10 \log \mu = -15\, dB$. The green line is the first order small perturbation solution for the fluid-fluid interface (zero shear). The red line is the 2-scale solution, where averaging over local slopes (rms angle 5^0) was performed. The dashed magenta line is the boss-SP solution for the individual rough facet.

scattering angles.

Small perturbation theory

"Simple" SP theory (green line) agrees with the data for large values of the scattering angle, however it underpredicts at low scattering angles. With addition of contributions from small scales (bosses) it agrees well in the entire scattering angle range (see dashed magenta line in the figure). When 2-scale theory (SP plus averaging over local slopes) is used, a 5^0 rms slope of the rough facet is needed to ensure a match between theory and data at low grazing scattering angles. However, the value of 5^0 rms slope is too high. Also, it is seen that using such a value for the rms angle I ended up having too much predicted scattering at high scattering angles $\theta_s > 50^0$ (see red line in the figure).

Conclusion

- Lambert's Law can be made to fit the data via an adjustable Mackenzie coefficient, however, one value of the Mackenzie coefficient can be used only locally, for a small enough range of angles.

- For the ARSRP scenario a 2-scale model does not explain the scattering physics. Forced to match data for 10^0 incidence and 10^0-40^0 scattering grazing angle, it gives a wrong prediction when the incidence angle decreases to 2^0.

- Addition of point scatterers results in an improved match between theory and data. Using the combination of bosses and small perturbation theory, I was able to model the data using only the knowledge of the surface statistics, without introduction of adjustable coefficients.
- Precise knowledge of the average incidence angle is important for modeling the low grazing angle scattering. Errors of $\pm 2^0$ can not be tolerated.

Chapter 8

Conclusions and Suggestions for Future Work

8.1 Conclusions

The important scientific questions which motivated the ARSRP experiment can be found in Chapter 1 and in Ref. [1]. Answering some of these questions was my objective.

The major scientific question of the ARSRP program was to decide what is the physics of rough ocean bottom scattering, and what are the physical parameters controlling the properties of the scattered signal.

From the analysis of the statistical properties of data, I conclude that scattering from rough bottoms has a discrete nature in its high amplitude returns. At lower levels a mixture of several scattering events with comparable amplitudes is mostly observed in the data, hence the statistics of the received signal, with the exception of the nonstationary mean value, becomes Gaussian.

This in turn answers the major ARSRP question. Except for the mean value, received signal statistics depend on the bistatic angle only. Properties of the event-like features observed in the signal ("clutter") are dominated by the wavelength scale scattering. On the other hand, for the mean value of the reverberation signal, large scale bathymetry and propagation effects are the controlling parameters.

Analyzing the received signal I found that it is a complicated nonstationary function of time, hence it is not well suited for reduction, processing and modeling. I found that the AGC processing widely used in radar technology effectively separates the received signal into its slow and fast components. The slow component (short-term mean value, related to the local scattering strength) is non-stationary function of time. However, it depends on the large-scale geomorphology, and should be approached deterministically.

The fast component carries all higher order statistical information about the scattering. It is a stationary function of time, which simplifies its analysis. However, it depends on wavelength scale roughness on the bottom, hence ought to be approached as a stochastic process. In turn, this suggests a deterministic approach to the modeling of the local mean value (i.e., expectation to measure the specific pressure level), but clearly precludes any further application of the deterministic approach. Only stochastic modeling of individual peaks is feasible. This means that a proper mixture of stochastic and deterministic approaches is needed for proper modeling of the scattering process.

This naturally leads to answering the last ARSRP scientific question (what is a good characterization of seafloor scattering and what is an adequate model for it). I found that the often used Lambert Law is inapplicable for modeling bistatic scattering. The small perturbation (SP) solution results in a reasonable estimate of the scattering within the forward sector (bistatic angle from 90^0 to 180^0), but generally underestimates scattering in the back sector (bistatic angle from 0^0 to 90^0). I showed that the reason for this mismatch may be found using the separation of scales hypothesis. First, the SP does not account for averaging over local rough facet slopes, which is important when larger sonar footprints are involved. The traditional 2-scale theory ought to be used to account for this effect. Second, and more important for the ARSRP scenario, scales smaller then $\lambda/2$ are not accounted for by the SP theory. I showed that inclusion of the contribution from these scales via the boss-SP theory results in an adequate model for the scattering observed during the ARSRP experiment, which matches experimental data in the back direction to within 3 *dB*.

An additional remark can be made on the notion of scattering strength. Use of the SP solution suggests that it suffices only away from the specular scattering direction. Scattering into the forward lobe (coherent reflection) is dominated by the zero order perturbation solution. It exhibits strong dependence on the patch size (generally, it is proportional to the area squared). The use of the scattering strength implies that scattering is proportional to the area, and therefore, it is inappropriate within the forward lobe.

8.2 Suggestions for future work

All real ocean bottoms possess elastic properties. I suggest expansion of the boss-SP theory into the elastic domain. Keeping the solution analytically tractable requires an analytical form of the perturbation solution for the fluid-elastic interface.

On the experimental side, I believe that controlled experiments in the laboratory environment can be helpful. I see two reasons for it. First, scattering can be effectively isolated from propagation and other effects. Secondly, having control of the surface, one is in a position to vary some of its parameters leaving others unchanged. This is unlikely to happen in an ocean environment, where one has no control over the rough surface and often insufficient knowledge about it.

Another possibility is a numerical experiment. In this case, an "exact" solution of the scattering problem (like for instance integral equation formulation) can be used for certain simplified scattering scenarios. Even though they are more restrictive then a real scattering experiment, numerical experiments can be significantly cheaper to perform.

Appendix A

Partitioning of the bistatic reverberation data

A.1 The sound propagation problem

Several ways to solve the propagation problem are known. Out of all I choose raytracing technique as the easiest and the least computationally demanding (implemented as a computer code "Artist" by V. H. Lupien, [114]). In general, ones ability to solve the propagation problem is limited by the insufficient knowledge about the environment (exact bathymetry, sound speed profile and experiment geometry). For the analysis of the ARSRP experiment uncertainty in the receiver array heading and precise bathymetry proved to be the major obstacles.

Analyzing the experiment, several methods to determine the array heading can be used. First, there are heading sensors within the receiver array, and readings of these sensors (which can be found in the experiment "log-files") can be used as an array heading. Second, since the ship heading is known (and logged), one can assume that towed array is moving in the same direction. Third, there are GPS sensors monitoring source and receiver position. Then one can assume that array heading coincide with the imaginary line drawn from source to receiver GPS positions. Finally, via raytracing modeling one can predict received signal using a simple scattering model. For instance, it is well known that strong large scale features in the received signal (so called "lineations") are related to transmission losses and large scale bathymetry. So if there is a large hill on the bottom, one can predict its appearance in the data. Then correlating the model prediction with the received data a one can make a judgment on the array heading (and also on the time delay if there were any, see Chapter 5, section on timing). Clearly, the last method gives the best results for array heading estimation. It also incorporates corrections of timing. Therefore, cross correlation of the model prediction with received data makes an important step in data partitioning. Availability of this correction technique is subject to presence of the strong deterministic feature in the ensonified region, hence it is not always available. In this thesis pings 430, 436, 469, 480, 486, 490 and 492 were chosen for processing. A strong deterministic feature known as a B' was visible during these pings, thus making the heading correction via correlation with model prediction possible. It was found that average correction to heading (compared to the heading value written in the log-file) is -4^0, and its standard deviation is 5^0, which is much larger than the receiver angular resolution (1.5^0 in the broadside beam). These emphasize the importance of an improved procedure for monitoring the receiver heading.

Additional uncertainty is related to the lack of knowledge about the actual bottom shape and position. Errors in the actual depth estimate inevitably arise due to uncertainty in the bathymetry map, and because exact array heading, ship position etc. are not known (i.e., at each moment of time scattering can be attributed to the wrong point on the bathymetry map). Using long range scattering data and large enough ship separations, one can somewhat reduce the impact of these uncertainties on the data quality (see next section).

Since neither exact location nor shape of the bottom was known during the ARSRP experiment, I decided to perform ray tracing to an artificial flat horizontal bottom located at $4500\,m$ depth, which is about right for the ARSRP conditions. Then, for long ranges (later times in the received signal) I assume that I have a good estimate of the bistatic angle and grazing angle relative to the flat reference plane. Real precise values of local grazing angles between sound wave and true bottom at each moment in the time series are unknown.

It makes sense to write a few more words on the choice of the reference plane. It absolutely does not have to be horizontal. For instance, consider large scale features of $\geq\ km$ scale. There is enough knowledge to consider these features deterministically. Clearly it is possible to distinguish between scattering from a steep slope of a large hill and scattering from a flat sediment pool. Then one can estimate the mean large scale slope by fitting a plane into the deterministic bathymetry.

There are two instances in which zero mean slope can be encountered. First, given enough knowledge of the deterministic bathymetry features, one can choose areas with low large scale mean slopes (this is what was done during data selection for this thesis). Second, when there is insufficient knowledge about the large scale bathymetry, zero mean slope again is a reasonable assumption. It is known that the rms roughness measured along the line of length L on the bottom is roughly proportional to $\sqrt{L}$. Then the angle made by the best fit line to the bathymetry is inversely proportional to $\sqrt{L}$. Therefore if large enough scales are considered, the mean slope tends to be small, hence the flat reference plane assumption becomes the most reasonable to make.

A.2 Relation between uncertainty in the depth estimate and uncertainty in the grazing and bistatic angles

To estimate the uncertainty, I consider a simple model. I first assume that sound wave propagates in the channel with the uniform sound speed and depth z (Figure A.1). At time t_0 scattering signal is generated by sound traveled along a path $l = ct_0$ (c is the sound speed), which correspond to the horizontal traveled distance R and grazing incident angle on the flat horizontal bottom α. Next I consider a depth variation dz in the channel. Then

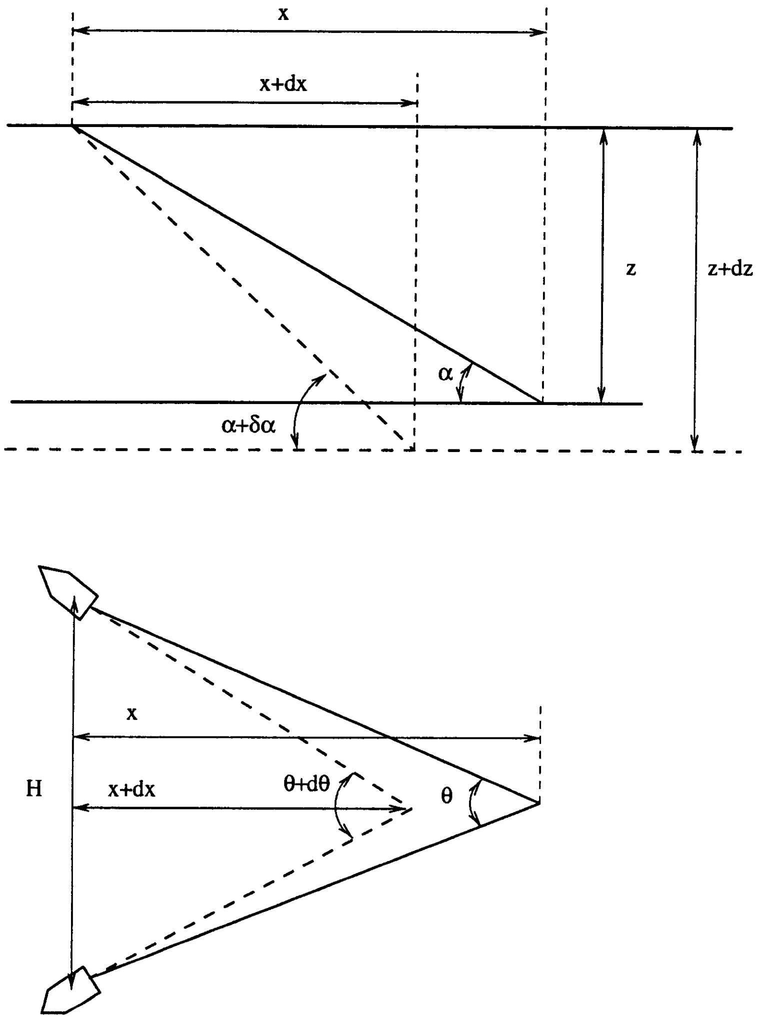

Figure A.1: Geometrical considerations for evaluating errors in estimation of the local incident grazing angle α and bistatic angle θ attributed to the point in the time series.

scattering is generated by another point on the bottom, and true incident and bistatic angles are $\alpha + d\alpha$ and $\theta + d\theta$, respectively. From easy geometrical considerations I can estimate the resultant change in angles $d\alpha$ and $d\theta$:

$$d\alpha = (z/l^2)dz, \tag{A.1}$$

$$d\theta = \frac{H \cdot z}{(l^2 + z^2)^{1.2} \cdot (1 + 0.25H^2/z^2)}, \tag{A.2}$$

where H is the horizontal distance between two ships. Clearly, if $R >> z$ and $H >> z$, errors in estimation of angles are by z/R or z/H smaller then the variation of depth.

Appendix B

Analytical form for the small perturbation solution

Consider a plane wave incident from the upper halfspace upon a rough fluid-fluid interface. In the following, subscripts "1" and "2" refer to the upper and lower medium, respectively. Solution for the scattering strength S_s observed in the halfspace of incidence due to the acoustic wave $k = 2\pi/\lambda$ is given by [31, 5]

$$S_s = 10 \log \left(k^4 \cdot |F|^2 \cdot \tilde{W}_h(\vec{\kappa_2} - \vec{\kappa_1}) \right), \quad dB \tag{B.1}$$

where

$$
\begin{aligned}
2k^2 F(\hat{\vec{k}}_1, \hat{\vec{k}}_2) = {} & \frac{(\rho_2 - \rho_1) \cdot \sqrt{k_1^2 - \kappa_1^2}}{\rho_1 \sqrt{k_2^2 - \kappa_1^2} + \rho_2 \sqrt{k_1^2 - \kappa_1^2}} \\
& \times \left\{ \left[-\vec{k}_1 \cdot \vec{\kappa}_1 + \frac{k_1^2 \rho_2 - k_2^2 \rho_1}{\rho_2 - \rho_1} \right] (1 + V) - \sqrt{k_2^2 - \kappa_2^2} \vec{k}_{1z} (1 - V) \right\}
\end{aligned}
\tag{B.2}
$$

In formulas (B.1 - B.2) ρ is the density, k is the acoustic wave number, and V is the plane wave reflection coefficient for the flat interface (i.e., coefficient of the incident wave reflection from the reference plane); $\vec{k}_1 = k \cdot \hat{\vec{k}}_1$ and $\vec{k}_2 = k \cdot \hat{\vec{k}}_2$ are the incident and scattered wave vectors; $\vec{\kappa}_1$ and $\vec{\kappa}_2$ are projections of $\vec{k}_1$ and $\vec{k}_2$ on the reference plane, respectively.

Bibliography

[1] Office of Naval Research. *Acoustic Reverberation Special Research Program Initial Report.* R/V Cory Chouest, July 5-26 1993.

[2] I. Dyer, A. Baggeroer, H. Schmidt, R. Fricke, N. Ozluer, and D. Giannoni. *Ocean reverberation*, pages 51–57. Kluwer Academic Publishers, 1993. Section 1. Discrete backscatter can be dominant in rough bottom scattering. Edited by D. D. Ellis, J. R. Preston and H. J. Urban.

[3] I. Dyer. Heuristic facet backscatter theory: a plausible model for dominant backscatter events? Woods Hole Oceonographic Institution, 1991. Office of Naval Research Acoustic Reverberation Special Research Project symposium.

[4] R. J. Urick. *Principles of underwater sound for engineers.* McGraw-Hill, New York, 1967.

[5] F. G. Bass and I. M. Fuks. *Wave scattering from statistically rough surfaces.* Pergamon Press, New York, 1979.

[6] E. I. Thorsos and D. R. Jackson. The validity of the perturbation approximation for rough surface scattering using a gaussian roughness spectrum. *J. Acoust. Soc. Am.*, 86:261–277, 1989.

[7] B. F. Kuryanov. The scattering of sound at a rough surface with two types of irregularity. *Sov. Phys. Acoust.*, 8:252–257, 1963.

[8] R. J. Urick. *Principles of underwater sound.* McGraw-Hill, New York, 1983.

[9] I. Tolstoy and C. S. Clay. *Ocean acoustics: theory and experiment in underwater sound.* McGraw-Hill, New York, 1966.

[10] I. Dyer. *Fundamentals and applications of underwater sound.* Cambridge University Press, 1996. Class notes, book in preparation.

[11] I. Tolstoy. *Wave propagation.* McGraw-Hill, New York, 1973.

[12] M. Crocker, editor. *Handbook of acoustics.* J. Wiley and Sons, 1997.

[13] F. B. Jensen, W. A. Kuperman, M. B. Porter, and H. Schmidt. *Computational Ocean Acoustics.* Am. Inst. of Phys., New York, 1994.

[14] L. M. Brekhovskikh. *Waves in layered media.* Academic Press, 1980.

[15] P. M. Morse and U. Ingard. *Theoretical acoustics.* McGraw-Hill, New York, 1968.

[16] D. J. Crighton, editor. *Modern methods in analytical acoustics.* Springer, 1992. Lecture notes.

[17] H. Schmidt. *SAFARI: Seismo-acoustic fast field algorithm for range independent environment.* SR 113, SACLANT ASW Research Center, La Spezia, Italy, 1987. User's guide.

[18] O. A. Godin. Parabolic approximation in the acoustics of moving media. *Acusticheskii Zhurnal*, 37:646–653, 1991.

[19] M. D. Collins. Low-frequency, bottom-interacting pulse propagation in range-dependent oceans. *IEEE J. Oceanic Eng.*, 13:222–228, 1988.

[20] F. B. Jensen. Wave theory modeling: a convenient approach to cw and pulse propagation modeling in low-frequency acoustics. *IEEE J. Oceanic Eng.*, 13:186–197, 1988.

[21] A. D. Pierce. *Acoustics: an introduction to its physical principles and applications.* Acoustical Society of America, New York, 1991.

[22] M. M. Boone and E. A. Vermaas. A new ray-tracing algorithm for arbitrary inhomogeneous and moving media, including caustics. *J. Acoust. Soc. Am*, 90:2109–2117, 1991.

[23] T. Farrell and K. D. LePage. Travel time variability and localization accuracy for global scale monitoring of underwater acoustic events. *J. Acoust. Soc. Am.*, 99:2572, 1996. Abstract, 132 meeting of the ASA.

[24] K. D. LePage. Relaxation techniques for finding horizontal eigenrays for global scale propagation. *J. Acoust. Soc. Am.*, 100:2833, 1996. Abstract, 3-rd joint meeting of the ASA and ASJ.

[25] C. M. Bender and S. A. Orzag. *Advanced mathematical methods for scientist and engineers.* McGraw-Hill, New York, 1978.

[26] A. Ishimaru. *Wave propagation and scattering in random media.* Academic Press, New York, 1978.

[27] P. Beckmann. *The scattering of electromagnetic waves from rough surfaces.* Artech House, Inc., Norwood, MA, 1987.

[28] T. Willmore. *An introduction to differential geometry.* Clarendon Press, 1959.

[29] J. A. Goff and T. H. Jordan. Stochastic modeling of sea floor morphology: inversion of sea beam data for second order statistics. *J. Geophys. Res.*, 93:13589–13608, 1988.

[30] J. A. Goff. The relationship between local- and global-scale scattering functions for fractal surfaces under a separation of scales hypothesis. *J. Acoust. Soc. Am.*, 97:1586–1595, 1995.

[31] S. M. Rytov, Yu. A. Kravtsov, and V. I. Tatarskii. *Principles of statistical radiophysics.* Springer-Verlag, New York, 1989.

[32] T. H. Bell Jr. Mesoscale sea floor roughness. *Deep-Sea Res.*, 26a:65–76, 1979.

[33] T. H. Bell Jr. Statistical features of sea floor topography. *Deep-Sea Res.*, 22:883–892, 1975.

[34] B. B. Mandelbrot. *Fractals : form, chance, and dimension.* W.H. Freeman, San Francisco, 1977.

[35] B. B. Mandelbrot. *The fractal geometry of nature.* W.H. Freeman, San Francisco, 1982.

[36] C. C. Barton and P. R. LaPointe. *Fractals in the Earth sciences.* Plenum Press, New York, 1995.

[37] G. Korvin. *Fractal models in the Earth sciences.* Elsevier, New York, 1992.

[38] V. I. Tatarskii. *Wave propagation in the turbulent medium.* McGraw-Hill, New York, 1968.

[39] V. I. Tatarskii. *The effects of the turbulent atmosphere on wave propagation.* Israel Program for Scientific Translations, Jerusalem, 1971.

[40] J. A. Goff and T. H. Jordan. Stochastic modeling of sea floor morphology: resolution of topographic parameters by sea beam data. *IEEE J. of Oceanic Eng.*, 14:326–337, 1989.

[41] H. Fan. *Wave theory modeling of three-dimensional seismo-acoustic reverberation in ocean waveguides.* PhD thesis, Massachusetts Institute of Technology, September 1995.

[42] K. D. LePage and H. Schmidt. Modeling of low-frequency transmission loss in the central arctic. *J. Acoust. Soc. Am.*, 96:1783–1795, 1994.

[43] K. D. LePage and H. Schmidt. Analysis of spatial reverberation statistics in the central arctic. *J. Acoust. Soc. Am*, 99:2033–2047, 1996.

[44] G. C. Bishop and J. Smith. A scattering model for nondifferentiable periodic surface roughness. *J. Acoust. Soc. Am.*, 91:744–770, 1992.

[45] J. Kevorkian. *Partial differential equations analytical solution techniques.* Chapman and Hall, New York, 1993.

[46] I. Tolstoy. Smoothed boundary conditions, coherent low-frequency scatter, and boundary modes. *J. Acoust. Soc. Am.*, 75:1–22, 1984.

[47] I. Tolstoy. Acoustic scatter from a slightly rough boundary between a fluid and an elastic solid. *J. Acoust. Soc. Am.*, 78:1727–1734, 1985.

[48] M. A. Biot. Generalized boundary conditions for multiple scatter in acoustics reflections. *J. Acoust. Soc. Am.*, 44:1616–1622, 1968.

[49] M. A. Biot. Lagrangian analysis of multiple scatter in acoustic and electromagnetic reflection. *Acad. R. Belgique, Bull. Cl. Sci*, 59:153–199, 1973.

[50] A. R. Wenzel. Smoothed boundary conditions for randomly rough surfaces. *J. Math. Phys.*, 15:317–323, 1974.

[51] L. M. Brechovskikh and Y. P. Lysanov. *Fundamentals of ocean acoustics.* Springer-Verlag, 1991.

[52] D. P. Winebrenner and A. Ishimaru. Application of the phase-perturbation technique to randomly rough surfaces. *J. Opt. Soc. Am.*, 2:2285–2294, 1985.

[53] M. S. Howe. Contributions to the theory of scattering by randomly irregular surfaces. *Proc. R. Soc. London A*, 337:413–433, 1974.

[54] M. S. Howe and L. A. Mysak. Scattering of poincare waves by an irregular coastline. *J. Fluid Mech.*, 57:111–128, 1973.

[55] Howe M. S. Wave propagation in random media. *J. Fliid Mech.*, 45:769–783, 1971.

[56] E. I. Thorsos. Acoustic scattering from a "pierson-moskowitz" sea surface. *J. Acoust. Soc. Am.*, 88:335–349, 1990.

[57] W. A. Kuperman and H. Schmidt. Self-consistent perturbation approach to rough surface scattering in stratified elastic media. *J. Acoust. Soc. Am.*, 86:1511–1522, 1989.

[58] B. Tracey. *An integrated modal approach to surface and volume scattering in ocean acoustic waveguides.* PhD thesis, Massachusetts Institute of Technology, January 1996.

[59] B. Tracey and H. Schmidt. Seismo-acoustic field statistics in shallow water. *IEEE J. Ocean. Eng.*, pages 317–331, 1997.

[60] J. T. Goh. *Spectral super-element approach for wave propagation in range dependent elastic medium.* PhD thesis, Massachusetts Institute of Technology, 1996.

[61] H. Schmidt, W. Seong, and J. T. Goh. Spectral super-element approach to range-dependent acoustic modeling. *J. Acoust. Soc. Am.*, 98:465–472, 1995.

[62] A. Ishimaru, L. Arles-Sengers, P. Phu, and D. Winebrenner. *Ultra-wideband, short-pulse electromagnetics 2*, chapter 5: Pulse scattering by rough surfaces, pages 431–438. Plenum Press, New York, 1995. Edited by L. Carin and L. B. Felsen.

[63] D. M. F. Chapman. An improved kirchhoff formula for reflection loss at a rough ocean surface at low grazing angles. *J. Acoust. Soc. Am.*, 73:520–527, 1983.

[64] S. T. McDaniel. High-frequency forward scatter from arctic ice: temporal response. *IEEE J. Oceanic Eng.*, 17:216–221, 1992.

[65] E. I. Thorsos. The validity of the kirchhoff approximation for rough surface scattering using a gaussian roughness spectrum. *J. Acoust. Soc. Am.*, 83:78–92, 1988.

[66] A. Ishimaru and J. S. Chen. Scattering from very rough surfaces based on the modified second-order kirchhoff approximation with angular and propagation shadowing. *J. Acoust. Soc. Am.*, 88:1877–1883, 1990.

[67] A. Ishimaru and J. S. Chen. Scattering from very rough metallic and dielectric surfaces - a theory based on the modified kirchhoff approximation. *Waves in random media*, 1:21–34, 1991.

[68] J. S. Chen and A. Ishimaru. Numerical simulation of the second-order kirchhoff approximation from very rough surfaces and a study of backscattering enhancement. *J. Acoust. Soc. Am.*, 88:1846–1850, 1990.

[69] I. Tolstoy. The scattering of spherical pulses by slightly rough surfaces. *J. Acoust. Soc. Am.*, 66:1135–1144, 1979.

[70] J. E. Burke and V. Twersky. Scattering and reflection by elliptically striated surfaces. *J. Acoust. Soc. Am.*, 38:883–895, 1966.

[71] J. E. Burke and V. Twersky. On scattering of waves by the infinite grating of elliptic cylinders. *IEEE Trans. Ant. and Prop.*, 14:465–480, 1966.

[72] V. Twersky. Coherent response to a point source irradiating a rough plane. *J. Acoust. Soc. Am.*, 73:1847–1863, 1984.

[73] O. I. Diachok. Effects of sea-ice ridges on sound propagation in the arctic ocean. *J. Acoust. Soc. Am.*, 59:1110–1120, 1976.

[74] V. Twersky. Multiple scattering of waves and optical phenomena. *J. Opt. Soc. Am.*, 52:145–171, 1962.

[75] R. S. Houston. *A treatise on light.* Longmans, Green and Co., New York, 1938.

[76] J. T. Koenderink and A. J. van Doorn. Geometrical models as a general method to treat diffuse interreflections in radiometry. *J. Opt. Soc. Am.*, 73:843–850, 1983.

[77] J. A. Smith, T. L. Lin, and K. J. Ranson. The lambertian assumption and landsat data. *Photogrammetric Eng. Rem. Sens.*, pages 1183–1189, 1980.

[78] S. K. Nayar and M. Oren. Visual appearance of matte surfaces. *Science*, 267, 1995.

[79] M. Oren and S. K. Nayar. Generalization of lambert's reflectance model. *Computer Graphics Proceedings, Annual Conference Series*, pages 239–245, 1994.

[80] M. Oren and S. K. Nayar. Generalization of lambertian reflectance model and implications for machine vision. *Int. J. of Comp. Vision*, 1995.

[81] S. K. Nayar, K. Ikeuchi, and T. Kanade. Shape from interreflectiions. *Int. J. Comp. Vis.*, 6:173–195, 1991.

[82] S. Stanic, K. B. Briggs, P. Fleisher, W. B. Sawyer, and R. I. Ray. High-frequency acoustic backscattering from a coarse shell ocean bottom. *J. Acoust. Soc. Am.*, 85:125–136, 1989.

[83] D. R. Jackson, D. P. Winebrenner, and A. Ishimaru. Application of the composite roughness model to high-frequency bottom backscattering. *J. Acoust. Soc. Am.*, 79:1410–1422, 1986.

[84] J. W. Caruthers and J. C. Novarini J. C. The partition wavenumber in acoustic backscattering from a two-scale rough surface described by a power-law spectrum. *IEEE J. Oceanic Eng.*, 19:100–107, 1994.

[85] J. C. Novarini and J. W. Caruthers. Modeling backscattering from a rough seafloor with sediment inhomogeneities. Technical report, Naval Research Laboratory, Stennis Space Center, MS 39529, February 27 1995.

[86] E. Bahar and M. A. Fitzwater. Like- and cross-polarized scattering cross sections for random rough surfaces: theory and experiment. *J. Opt. Soc. Am.*, 2:2295–2303, 1985.

[87] A. K. Fung and M. F. Chen. Numerical simulation of scattering from simple and composite random surfaces. *J. Opt. Soc. Am.*, 2:2274–2284, 1985.

[88] I. M. Fuks. Spectral width of signals scattered by a disturbed sea surface. *Sov. Phys. Acoust.*, 20:276–281, 1974.

[89] J. W. Caruthers and J. C. Novarini. Modeling bistatic bottom scattering strength including a forward scatter lobe. *IEEE J. Oceanic Eng.*, 18:100–107, 1993.

[90] P. Phu, A. Ishimaru, and Y. Kuga. Controlled millimeter-wave experiments and numerical simulation on the enhanced backscattering from one-dimensional very rough surfaces. *Radio Sci.*, 28:533–548, 1993.

[91] J. R. Fricke. *Acoustic scattering from elastic ice: a finite difference solution.* PhD thesis, WHOI-MIT Joint Program, June 1991.

[92] J. R. Fricke. Acoustic scattering from elemental ice features: numerical modeling results. *J. Acoust. Soc. Am.*, 93:1784–1796, 1993.

[93] R. A. Stephen and S. A. Swift. Modeling seafloor geoacoustic interaction with the numerical scattering chamber. *J. Acoust. Soc. Am.*, 96:973–990, 1994.

[94] R. A. Stephen and M. E. Dougherty. *Computational acoustics*, volume 1, pages 227–246. Elsevier, 1993. Edited by R. L. Lau, D. Lee and A. R. Robinson.

[95] R. L. Holford. Scattering of sound waves at a periodic, pressure-release surface: an exact solution. *J. Acoust. Soc. Am.*, 70:1116–1128, 1981.

[96] J. L. Uretsky. The scattering of plane waves from periodic surfaces. *Ann. Phys.*, 33:400–427, 1965.

[97] T. J. Cox. Predicting the scattering from reflectors and diffusers using two-dimensional boundary element methods. *J. Acoust. Soc. Am.*, 96:874–878, 1994.

[98] Office of Naval Research. *Acoustic Reverberation Special Research Program Initial Report.* R/V Cory Chouest, August 19 1991.

[99] J. R. Preston, E. Michelozzi, L. Troiano, and R. Hollett R. *Acoustic Reverberation Special Research Program Initial Report.* R/V Alliance. SACLANTEN and ONR ARSRP group joint experiment, August 30 1993.

[100] A. B. Baggeroer. *Applications of digital Signal Processing*, chapter Sonar signal processing. Prentice-Hall, 1978. Edited by A. V. Oppenheim.

[101] B. G. Ferguson. Remedying the effects of array shape distortion on the spatial fitering of acoustic data from a line array of hydrophones. *IEEE J. Oceanic Eng.*, 18:565–571, 1993.

[102] D. A. Gray, B. D. O. Anderson, and R. R. Bitmead. Towed array shape estimation using kalman filters - theoretical models. *IEEE J. Oceanic Eng.*, 18:543–556, 1993.

[103] S. Stanic and E. G. Kennedy. Reverberation fluctuations from a smooth sea floor. *IEEE J. Oceanic Eng.*, 18:95–99, 1993.

[104] H. Boehme and N. P. Choritos. Acoustic backscattering at low grazing angles from the ocean bottom. *J. Acoust. Soc. Am.*, 84:1018–1029, 1988.

[105] G. R. Wilson and D. R. Powell. Probability estimates of surface and bottom reverberation. *J. Acoust. Soc. Am.*, 73:195–200, 1983.

[106] P. Faure. Theoretical model of reverberation noise. *J. Acoust. Soc. Am.*, 36:256–259, 1964.

[107] Middleton. A statistical theory of reverberation and similar first-order scatter yelds. part i: waveforms and general process. *IEEE Trans. Inform. Theory*, IT-13:372–392, 1967.

[108] V. V. Olshevsky. Statistical methods of sonar. Technical report, Consultants Bureau, New York, 1978.

[109] V. V. Olshevsky. Characteristics of sea reverberation. Technical report, Consultants Bureau, New York, 1967.

[110] N. P. Choritos, H. Boehme, T. G. Goldsberry, S. P. Pitt, R. A. Lamb, A. L. Garsia, and R. A. Altenburg. Acoustic backscattering at low grazing angles from the ocean bottom. part ii. statistical characteristics of bottom backscatter at a shallow water site. *J. Acoust. Soc. Am.*, 77:975–982, 1985.

[111] M. Gensane. A statistical study of acoustic signals backscattered from the sea bottom. *IEEE J. Oceanic Eng.*, 14:84–93, 1989.

[112] J. A. Goff. Multi-scale spectral analysis of hydrosweep, ams-120, and mesotech profiles from site b. Woods Hole Oceanographic Institution, July 19 1995. Bottom-subbottom acoustic reverberation special research program symposium.

[113] V. Twersky. On scattering and reflection of sound by rough surfaces. *J. Acoust. Soc. Am.*, 29:209–225, 1957.

[114] V. H. Lupien. Coregistration of received signals with bathymetry using artist. *J. Acoust. Soc. Am.*, page 3345, 1994. Abstract, 128 ASA meeting.